الجمهورية الجزائرية الديمقراطية الشعبية

République Algérienne Démocratique et Populaire

Ministère de L'Enseignement Supérieur et de la Recherche Scientifique

Université Ferhat ABBAS Sétif 1

UNIVERSITÉ SETIF1 - FERHAT ABBAS

FACULTÉ DE TECHNOLOGIE

THÈSE

Présentée au Département de Génie des procèdes

Pour l'obtention du diplôme de

DOCTORAT

Domaine : Sciences et Technologie

Filière: Génie des procédés **Option: Génie Chimique**

Par

FENNI Manel

THÈME

MODELISATION NUMERIQUE DES TRANSFERTS THERMIQUES DANS UN MILIEU POREUX SOUMIS A DE FORTES VARIATIONS DE TEMPERATURE

Soutenue le 11 / 12 / 2025 devant le Jury:

BOUTAHALA Mokhtar	**Professeur**	**Univ. Sétif 1- Ferhat Abbas**	**Président**
GUELLAL Messaoud	**Professeur**	**Univ. Sétif 1- Ferhat Abbas**	**Directeur de thèse**
HAMIMID Saber	**M.C.A.**	**Univ. B.B.A - M.B. El Ibrahimi**	**Co-Directeur**
CHIBANE Lemnouer	**Professeur**	**Univ. Sétif 1- Ferhat Abbas**	**Examinateur**
MAHFOUD Brahim	**Professeur**	**Univ. Bouira-Akli M. Oulhadj**	**Examinateur**
GOUIDMI Hamza	**M.C.A.**	**Univ. B.B.A - M.B. El Ibrahimi**	**Examinateur**

الجمهورية الجزائرية الديمقراطية الشعبية

People's Democratic Republic of Algeria

Ministry of Higher Education and Scientific Research

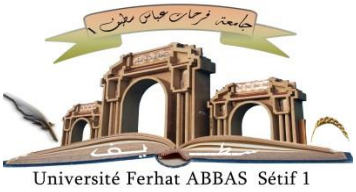

UNIVERSITY OF SETIF1 - FERHAT ABBAS

FACULTY OF TECHNOLOGY

THESIS

Presented to the Department of Process Engineering

For the degree of

DOCTORATE

Field : Science and Technology

Major : Process Engineering **Specialization: Chemical Engineering**

By

FENNI Manel

TOPIC

NUMERICAL MODELING OF HEAT TRANSFERS IN A POROUS MEDIUM SUBJECTED TO LARGE TEMPERATURE VARIATIONS

Defended on 11 / 12 / 2025 before the Jury:

BOUTAHALA Mokhtar	**Professor**	**Univ. Sétif 1-Ferhat Abbas**	**President**
GUELLAL Messaoud	**Professor**	**Univ. Sétif 1-Ferhat Abbas**	**Thesis Director**
HAMIMID Saber	**M.C.A.**	**Univ. B.B.A- M. B. El Ibrahimi**	**Co-Director**
CHIBANE Lemnouer	**Professor**	**Univ. Sétif 1-Ferhat Abbas**	**Examiner**
MAHFOUD Brahim	**Professor**	**Univ. Bouira-Akli M. Oulhadj**	**Examiner**
GOUIDMI Hamza	**M.C.A.**	**Univ. B.B.A- M. B. El Ibrahimi**	**Examiner**

Acknowledgements

I am sincerely grateful to all those who contributed to the completion of this thesis. This journey would not have been possible without their invaluable support and encouragement.

First and foremost, I extend my heartfelt gratitude to Professor Messaoud GUELLAL, who supervised this research at the Laboratory of Chemical Process Engineering, Sétif 1 University-Ferhat Abbas. His guidance, expertise, and unwavering support throughout this study were instrumental in its completion.

I also extend my sincere thanks to my co-director of my thesis, Dr. Saber HAMIMID, an assistant professor at the University of Bordj Bou Arréridj-Mohamed El Bachir El Ibrahimi, for his support and guidance throughout my thesis.

I am honored that Professor Mokhtar BOUTAHALA from Sétif 1 University-Ferhat Abbas of chaired the jury of my thesis. His support and guidance are deeply appreciated.

I am equally grateful to Professor Lemnouer CHIBANE from Sétif 1 University-Ferhat Abbas, Professor Brahim MAHFOUD from the University of Bouira-Akli Mohand Oulhadj and Hamza GOUIDMI an assistant professor at the University of Bordj Bou Arréridj-Mohamed El Bachir El Ibrahimi, for agreeing to serve as examiners.

I extend my heartfelt thanks to everyone mentioned above and to all those who have supported me in various ways, big and small. This thesis is the culmination of collective efforts and shared dedication.

Dedications

*I owe an immense debt of gratitude to **God** first and foremost, for his guidance and for every blessing bestowed upon me.*

To my family, whose unwavering love, understanding, and encouragement have been my pillars of strength. Their patience and unwavering belief in me have carried me through.

*To my parents, **Nadhir** and **Leila**,*

*To my son, **Djoud**,*

*To my brother, **Seif**, and his family,*

*To my sisters, **Imane**, **Bouchra**, and **Yasmine**,*

*To my dearest friend, **Dounia**, and her family,*

To all my colleagues and friends,

Your support and unwavering faith in me have meant more than words can express. Thank you for standing by me throughout this journey.

CHAPTER III : Numerical resolution

CHAPTER IV: Coupled Natural Convection and Internal Heat Generation in a Square Cavity with a Fluid-Saturated Porous Layer

CHAPTER V: Natural Convection Heat Transfer in Porous Square Cavity Under Low Mach Number Approximation

CHAPTER VI: Investigating the Influence of Surface Radiation on Heat Transfer and Fluid Flow in a Square Cavity with a Porous Layer at the Bottom

LIST OF FIGURES

CHAPTER I: Advances in Low Mach Number Natural Convection in Porous Media: A Comprehensive Review

CHAPTER III: Numerical resolution

CHAPTER IV: Coupled Natural Convection and Internal Heat Generation in a Square Cavity with a Fluid-Saturated Porous Layer

CHAPTER V: *Natural Convection Heat Transfer in Porous Square Cavity Under Low Mach Number Approximation*

CHAPTER VI: Investigating the Influence of Surface Radiation on Heat Transfer and Fluid Flow in a Square Cavity with a Porous Layer at the Bottom

LIST OF TABLES

CHAPTER III: Numerical resolution

CHAPTER IV: Coupled Natural Convection and Internal Heat Generation in a Square Cavity with a Fluid-Saturated Porous Layer

CHAPTER V: Natural Convection Heat Transfer in Porous Square Cavity Under Low Mach Number Approximation

CHAPTER VI: Influence of Surface Radiation on Heat Transfer and Fluid Flow in a Square Cavity with a Porous Layer at the Bottom

Nomenclature

Cp	Specific heat at constant pressure, $J.kg^{-1}.K^{-1}$
Cv	Specific heat at constant volume, $J.kg^{-1}.K^{-1}$
Da	Darcy number, $Da = K.H^{-2}$
D_x, D_y	Matrix drags per unit volume of the porous medium
F_{ij}	Geometry view factor
g	Gravitational acceleration, $m.s^{-2}$
H	Height of the enclosure, m
k	Thermal conductivity, $W.m^{-1}.K^{-1}$
K	Permeability, m^2
Nu	Nusselt number
Nu_{avg}	Average Nusselt number
$Nr = \sigma T_0^4 H / k\Delta T$	Dimensionless parameter of conduction-radiation
p	Dynamic pressure, Pa
p'	Dynamic perturbed pressure, $p' = p - \bar{p} + \rho_0 gy,\ Pa$
$\bar{p}$	Mean thermodynamic pressure, Pa
$\bar{P}$	Dimensionless mean thermodynamic pressure
Pr	Prandtl number, $Pr = \nu/\alpha$
q	Internal heat generation [W m^{-3}]
Qr	Dimensionless net radiative heat flux
Ra_E	External Rayleigh number ($= \frac{g\beta\Delta TH^3}{\nu\alpha}$)
Ra_I	Internal Rayleigh number ($= \frac{g\beta\Delta TqH^5}{\nu\alpha k}$)
R	Mass-specific gas constant, $J.kg^{-1}.K^{-1}$
Ra	Rayleigh number, Ra$= \frac{g\beta\Delta TH^3}{(\nu\alpha)}$
R_i	Dimensionless Radiosity
r	Internal source term
t	Time, s
T	Dimensional temperature, K
$T_C(T_H)$	Temperature on left (right) vertical wall of cavity, $T_H > T_C,\ K$
T_0	Reference temperature, $T_0 = \frac{T_H+T_C}{2}$, K

u	Velocity in x-direction, $m.s^{-1}$
v	Velocity in y-direction, $m.s^{-1}$
$\vec{V}$	Field velocity, $\left(u\vec{e}_x + v\vec{e}_y\right)$, $m.s^{-1}$
U, V	Dimensionless velocity-components
$x\ , y$	Cartesian coordinates, m
X, Y	Dimensionless coordinates
X_p	Dimensionless width of the porous layer
Y_p	Dimensionless thickness of the porous layer

Greek symbols

α	Thermal diffusivity, $m^2.s^{-1}$
β	Thermal expansion coefficient, $-1/\rho_0(\partial\rho/\partial T)$, K^{-1}
γ	Ratio of specific heats Cp and Cv
ΔT	Temperature difference, $\Delta T = T_H - T_C\ , K$
ε	Porosity of the porous layer
ε_r	Emissivity
ε_b	Boussinesq parameter: $\varepsilon_b = \Delta T/2T_0$
η	Dimensionless size of the porous layer
θ	Dimensionless temperature, $\theta = (T - T_0)/\Delta T$
$\Theta = T/T_0$	Dimensionless radiative temperature
μ	Dynamic viscosity of the fluid, $kg.m^{-1}.s^{-1}$
ν	Kinematic viscosity, $m^2.s^{-1}$
π	Dimensionless pressure
ρ	Fluid density, $kg.m^{-3}$
τ	Dimensionless time
σ	Ratio of heat capacities $\sigma = \left(\varepsilon(\rho Cp)_f + (1-\varepsilon)(\rho Cp)_s\right)/(\rho Cp)_f$

Subscripts

avg	Average value
C	Cold
H	Hot
eff	Effective property of the porous layer
f	Refers to the fluid domain
s	Refers to the porous medium

CP	Constant properties
VP	Variable properties
0	Reference state
$*$	Dimensionless parameters

GENERAL INTRODUCTION

Industries are increasingly turning to modeling to solve multi-physics problems related to the design of systems with complex geometries. The advancing performance of modern computers allows for calculations involving coupled physical phenomena, such as thermo-mechanical deformations of structures, coupled heat transfers involving conduction, convection, and radiation, fluid-structure interaction, and electromagnetic-thermal coupling. Numerous studies have been conducted using numerical and practical experimentation. While laboratory experimentation is crucial for validating the initial approach, it is hindered by the high cost of equipment and implementation difficulties. Numerical simulation remains the most cost-effective and widely used method. The rapid evolution of computer capabilities over the past two decades has significantly advanced our understanding of natural convection, thermal radiation, and the coupling between these phenomena.

Coupled thermal phenomena in confined environments are of considerable interest in the field of engineering. This interest is reflected in numerous applications, such as solar energy collectors, electronic component cooling, thermal comfort in buildings, and furnaces, among others. The study of natural convection in confined spaces is still the subject of extensive research, both numerically and experimentally. In such problems, various modes of heat transfer (convection, conduction, radiation) can occur in a coupled manner, particularly through the walls.

The majority of these studies involve a relatively small temperature difference, for which the Boussinesq approximation is used, assuming that fluid properties remain constant except for a linear dependence of density on temperature in the gravity term. However, in many physical and industrial applications, such as thermal insulation systems, chemical reactors, atmospheric flows, and combustion processes, temperature differences can reach tens of degrees. In such situations, the assumptions used to apply the Boussinesq approximation cannot be justified, and a different modeling approach is required, one that takes into account realistic variations in fluid properties.

Our work aims to study natural convection and the coupling between natural convection and surface radiation in a differentially heated cavity in the non-Boussinesq case, in the presence of a porous medium and internal heat generation. The objective here is to consider large temperature differences by using low Mach number models that allow us to dispense with the Boussinesq hypothesis while maintaining the decoupling between pressure and density fluctuations characteristic of incompressible flows. The numerical resolution of this problem primarily involves the finite volume approximation of the generalized Navier-Stokes equations.

Particular attention is given to examining the effect of the Boussinesq parameter, the Rayleigh number, wall emissivity, the variation of thermophysical properties of the fluid with temperature, the Darcy number, porosity, and the internal Rayleigh number on the temperature distribution, the flow structure within the cavity, and the contribution of different phenomena to overall heat transfer.

This manuscript is structured into six chapters.

Chapter 1 provides an extensive literature review on natural convection in closed cavities. It presents the generalities and definitions related to the studied phenomena, namely natural convection, internal heat generation and thermal radiation, as well as their coupling. The chapter also reviews different works that have addressed this type of problem, including studies conducted under the Boussinesq approximation, using low Mach number models, and in porous media.

In Chapter 2, we describe in detail the modeling steps used in a two-dimensional system. Starting from a general formalism, we present the balance equations describing the unsteady motion of a Newtonian, viscous, and compressible fluid. Then, simplifying assumptions are applied to different degrees to achieve different types of flow (low Mach flow, incompressible flow, and dilatable flow), highlighting the application limits relative to each system of equations.

Chapter 3 describes the numerical solution methodology for the partial differential equations presented in Chapter 2. Throughout this chapter, we briefly present the finite volume method applied to fluid flows and, in general terms, the steps of discretization of mathematical equations.

Chapter 4 focuses on the investigation of the coupling between porous medium and natural convection with an internal heat source. The motivation for this study stems from the limited number of research studies that have explored this specific coupling. Therefore, the objective of the study is to examine how the presence of a porous medium and internal heat generation influence fluid flow and heat transfer within a square cavity.

Chapter 5 is dedicated to presenting the numerical results of pure natural convection at a low Mach number of a fluid (air) confined in a differentially heated square cavity. The objective is to first validate the developed numerical code by comparing the obtained results with those in the literature. Then, we study the validity range of the Boussinesq approximation and examine the effect of various dominant parameters on the thermal and dynamic behavior of the fluid, including the presence of a porous medium and its properties such as permeability and porosity.

Chapter 6 focuses on the study of the coupling between natural convection and surface radiation in a differentially heated square cavity in the non-Boussinesq case. Numerical experiments are conducted to validate the method and highlight the effect of radiation on the thermal and dynamic fields, taking into account the presence of a porous medium and its properties.

The culmination of these six chapters leads to a comprehensive understanding of the complex interplay between natural convection and other influential factors in diverse systems. The findings contribute to the optimization and design of systems with complex geometries, enabling advancements in fields such as energy systems, environmental engineering, and geothermal technologies. By considering realistic variations in fluid properties, non-Boussinesq conditions, and the coupling with porous media, this research pushes the boundaries of our knowledge, paving the way for innovative solutions and improved system performance.

I.1 INTRODUCTION

With the prodigious development of modern techniques, it has become essential for any engineer, regardless of the field in which they will be called upon, to possess a good knowledge of the fundamental laws of heat transfer. This phenomenon is particularly significant in technical sciences, engineering designs, and industry; it manifests in all aspects of life and has a wide range of applications. Heat transfer is a complex process that occurs based on the different fundamental modes, namely: conduction, convection, and radiation. Among these modes, convection stands out as the most significant mode of energy transfer. Considering the factors that induce fluid motion, convection can be classified into three categories: forced convection, natural convection, and mixed convection

Natural convection of fluids in enclosures has garnered extensive research attention due to its importance in mechanical, industrial, thermal, and engineering applications. It finds practical applications in electronic component refrigeration, buried pipe protection, nuclear reactor cooling systems, solar energy collection, and room ventilation, among others [1]. Researchers have explored numerous cavity forms, including rectangular configurations [2,3], triangular shapes [4], trapezoidal structures [5], and other variations [6,7]. Sadeghi et al. [8] have provided a comprehensive review of studies that employed cavities and enclosures with different geometric designs.

The natural convection process within a square cavity has garnered significant interest from researchers over the years due to its importance and wide range of applications across various disciplines and sectors [9,10]. The first studies in this field date back to 1942 and include notable works such as those by **Elenbaas** [11], and the syntheses conducted by **Ostrach** [12,13], **Batchelor** [14], **Shih** [15], and **Gebhart et al.** [16]. In the latter reference, the validity limits of the widely used Boussinesq hypothesis in the analysis of natural convection are thoroughly discussed. In 1983, **De Vahl Davis and Jones** [9] confirmed the accuracy of the benchmark solution, establishing a foundation for verifying different methods and computer programs employed to generate contributed solutions.

Reddy et al. [17] conducted a numerical investigation on the flow of nanofluid inside a square cavity under isothermal conditions on both side walls and adiabatic conditions on the top and bottom walls. The finite difference method was utilized to solve the governing differential equations expressed in terms of the stream function. The results indicate an increase in the rate of heat transfer with higher values of the Rayleigh number (Ra).

The investigation conducted by **Hassanzadeh et al.** [18] focuses on the impact of a revolving rough cylinder within a square cavity on the mechanism of natural convective heat transfer. Six different cases are examined, and the differences between the cases become more pronounced at lower Rayleigh numbers and higher rotating speeds.

In a study by **Rui et al.** [19], the process of natural convection melting in a square cavity is explored. The authors developed an enthalpy-based lattice Boltzmann model (TLBM) in combination with the pseudo-potential LB model to accurately track the solid-liquid interface.

The results demonstrate that TLBM effectively simulates the solid-liquid phase transition process with great precision.

In a study by **Leporini et al.** [20], the natural convection process of air within a square cavity with active side and bottom walls was investigated. The authors examined the effects of the position relative to the gravity vector and the temperature difference between the hot and cold walls. Numerical simulations were performed using both a pure convection model and a combined radiative-convective model. The results show good agreement with experimental measurements, and the inclusion of radiance contribution does not affect the outcomes.

A numerical analysis of laminar natural convection in a square cavity filled with air (Pr = 0.71) was provided by **Alsabery et al.** [21]. The cavity contained two cylinders of different geometric shapes (square, circular, and elliptical), each with the same surface area. While the other walls of the cavity were assumed to be fully insulated, the right wall was uniformly cooled to a constant temperature, Tc. The results highlighted the significant influence of Rayleigh numbers on the flow and heat transfer within the cavity

Karki et al. [22] employed the lattice Boltzmann approach to study the impact of adiabatic obstructions on two-dimensional natural convection within a square enclosure. It was observed that the average heat transfer along the hot wall increases with the size of the obstacles until it reaches an optimum value. Further increases in size lead to a decrease in heat transfer.

The Boussinesq approximation, widely used for numerically simulating natural convection problems, is based on the Oberbeck-Boussinesq principle. However, the accuracy of this approximation was limited to small temperature variations. To address this limitation, researchers and engineers were motivated to develop approaches that extend beyond the range of validity of the Boussinesq approximation, particularly for buoyancy-driven flows with large temperature differences. **Mayeli et al.** [23] collected and classified various methodologies for the numerical modeling of laminar natural convection, including both Boussinesq and non-Boussinesq approximations for Newtonian fluids. These classifications fell into two broad categories: compressible and incompressible techniques. Figure 1 provides a summary of the different approximations used for the numerical simulation of natural convection problems.

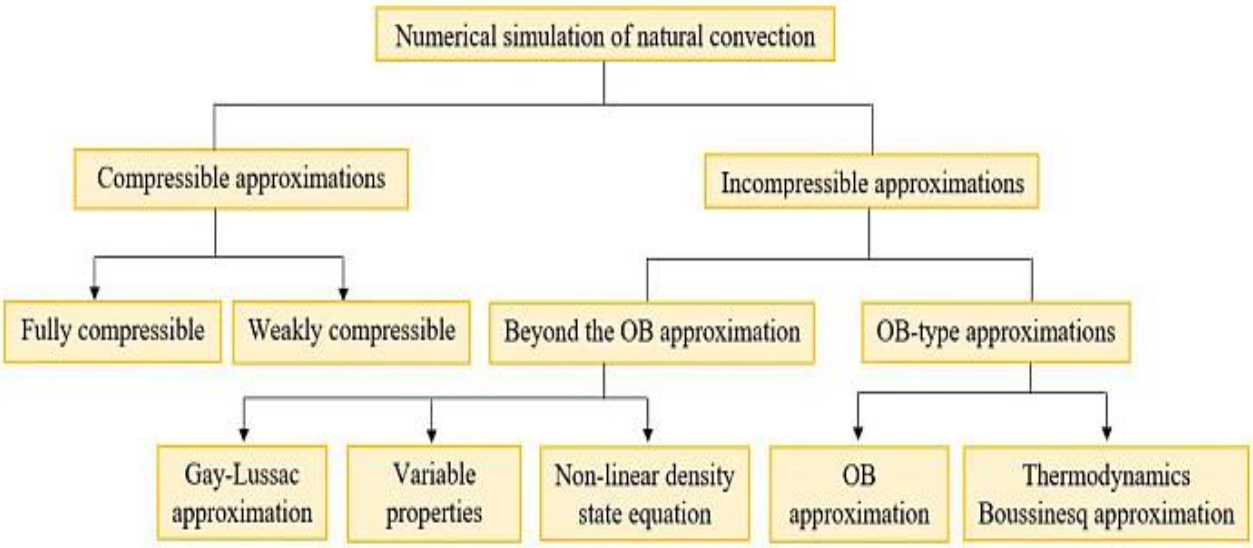

Figure I.1: Classification of various approximations used in the numerical modeling of natural convection issues.

I.2 BOUSSINESQ APPROXIMATION

In 1903, **Boussinesq** observed that density variations can be neglected, except when multiplied by gravitational acceleration in the equation of motion for the vertical component of the velocity vector [24]. This simple approximation has had a profound impact on various areas of fluid dynamics. It allows us to treat flows with small density variations as incompressible while still accounting for the primary effects of density variations. Moreover, it holds significant analytical and numerical importance by eliminating acoustic modes, which can be challenging to handle

Many problems in fluid dynamics have been successfully solved using Boussinesq-type approximations, yielding results that align well with experimental data [25]. Notably, the work of **Gray and Giorgini** [26] deserves mention, as they developed a new method for deriving approximation equations for natural convection flows. By systematically applying this approach, they defined specific conditions for eliminating different terms. This technique effectively determines the conditions under which a particular Newtonian liquid or gas satisfies the conventional Boussinesq approximation. The study used air and water at room temperature as examples to illustrate the application of this technique.

Turkel [27] provided a general description of preconditioning the steady-state compressible inviscid fluid dynamic equations. Extensions of the Navier-Stokes equations were also taken into account. Various variations of the preconditioning matrix were presented, along with implementation details.

Cherkasov et al. [28] discussed laminar natural convection in a gas confined between two vertical isothermal plates, each heated to different temperatures. They obtained an analytical solution using the Boussinesq approximation and compared it to a similar problem involving a liquid.

Hamimid et al. [29] investigated the combined effects of laminar natural convection and surface radiation in a differentially heated square cavity. The computations were performed using the finite volume method, a staggered grid, and the SIMPLER algorithm. A power-law scheme was applied to approximate the advection-diffusion terms, while analytical formulas were used to calculate view factors. The study examined the influence of emissivity on temperature and velocity profiles within the enclosure. Additionally, results for local and average convective and radiative Nusselt numbers under various parametric conditions were provided and analyzed.

Meyali et al. [30] presented a formulation based on the Boussinesq approximation for the numerical simulation of natural convection. By incorporating density variations into the advection terms, the study accounted for centrifugal effects arising from both bulk enclosure rotation and individual vortices, leading to more accurate results.

Many numerical and theoretical studies on natural convection in a cavity use the Boussinesq approximation [28,31–35]. Recently, the ideal gas law and asymptotic expansion methods have been employed to reevaluate this approximation. Generally, the Boussinesq approximation is considered valid when the maximum temperature differences do not exceed 10% of the reference temperature of the gas [36]. However, this approximation has not been questioned in the context of solute convection, highlighting the need to develop alternative non-Boussinesq models, such as the low Mach number approximation, to address these situations

I.3 LAW MACH NUMBER APPROXIMATION

Boussinesq's approximation has sparked extensive discussion, as previously mentioned. Over the past fifty years, numerous publications have addressed the validity of the Boussinesq approximation, particularly in the context of closed systems [37–39].

Gray and Giorgini [26] provided detailed information on the Boussinesq approximation, noting that its validity limit for air is around 28.6 K. This work has likely influenced the ideas developed by Paolucci [40], which are currently being examined in several studies. In particular, **Rey** [41] built on these ideas by specifying the limits of applicability of this approximation and further explored its practical constraints.

In practical terms, Mach numbers are always extremely low for internal flows, rendering the Mach number limit insignificant. Additionally, **Pons and Le Quéré** [42–44] raised concerns about the impact of pressure forces and even viscosity [45].

In general, density fluctuations in physical flows can arise from compressibility (pressure variation), dilatability (temperature variation), or a combination of two species (fluids with different densities). When the Mach number in a flow exceeds unity, the flow becomes supersonic and may exhibit shock waves that significantly influence the flow behavior. Even at low fluid velocities (such as in natural or mixed convection), numerically processing the conservation equations in their compressible form presents challenges.

The concept of a low Mach number arises when studying compressible flows at low speeds. This condition is characterized by a flow's characteristic velocity, U, being significantly

lower than the speed of sound, c (which represents the propagation speed of pressure waves). Consequently, the Mach number, Ma, defined as the ratio of U to c, is much less than unity. Such flows are encountered in various physical phenomena, including oceanic circulation, respiratory and vocal processes, natural convection, aeroacoustics, and industrial processes such as gas cooling or heating in enclosed domains and combustion. In these cases, significant density variations occur due to heat generated by chemical reactions. Furthermore, even in hypersonic flows, regions near stagnation points and adhesive surfaces can exhibit zero velocity.

Paillere et al. [46] investigated two numerical methods for solving low Mach number compressible flows and their application to single-phase natural convection problems. One method is based on an asymptotic model of the Navier-Stokes equations, which is valid for small Mach numbers. The other method is more general than the Boussinesq incompressible flow model.

Jagannathan et al. [47] presented results from direct numerical simulations of stationary compressible isotropic turbulence conducted at very high resolutions. They analyzed compressibility effects by decomposing the velocity and pressure fields into solenoidal and dilatational components. They proposed a critical turbulent Mach number of approximately 0.3, which delineated two distinct flow regimes.

Arima [48] investigated a mathematical model for environmental fluids that described fluid flow motions with significant density variations. The model was formulated as an unsteady low-Mach number flow based on the compressible Navier-Stokes equations. By making this assumption, the detailed acoustic effects were eliminated from the governing equations.

Boscarino [49] presented a finite volume shock-capturing method that asymptotically preserved all Mach numbers for numerical solutions of the compressible Euler equations of gas dynamics. Numerical tests were conducted in one and two dimensions to demonstrate the performance of the proposed scheme in both compressible and incompressible regimes.

Yu Zhang et al. [50] numerically investigated the non-Boussinesq effect in thermal convection within an air-filled horizontal concentric annulus using the variable property-based lattice Boltzmann flux solver (VPLBFS). The study analyzed various solutions, including the real solution considering total fluid properties, constant property solution, dynamic viscosity, partial Boussinesq approximation, thermal conductivity, and fluid density. The study revealed complex flow instability behavior under non-Boussinesq conditions and its correlation with heat transfer characteristics. It emphasized the significance of considering the integral effect of total fluid properties and fluid density variation.

The low Mach number approximation has become a valuable tool in fluid dynamics and thermodynamics. It simplifies the mathematical representation of fluid flow phenomena when the flow velocity is much smaller than the speed of sound. This technique is based on the understanding that density variations due to compressibility are negligible at low Mach numbers. As a result, it has been widely applied across various scientific and engineering fields. From astrophysics to combustion science, and from environmental modeling to biomedical

engineering, the low Mach number Approximation has provided valuable insights and predictions for complex fluid behaviors.

I.4 NATURAL CONVECTION IN POROUS MEDIA

Natural convection in porous media is a fascinating field where the low Mach number approximation plays a crucial role. Natural convection refers to the flow of a fluid driven by temperature gradients and the resulting density differences, while porous media involve materials with interconnected voids filled by a fluid. Understanding the interaction between natural convection and porous media is of great importance in various domains, including geothermal energy extraction, subsurface environmental remediation, and the study of heat transfer in porous materials such as soils. Researchers typically use a combination of the Darcy-Brinkman equation, which describes fluid flow through porous media, and the heat conduction equation to analyze natural convection in porous media. These equations are often solved together to model the coupled phenomena.

Modeling natural convection in porous media presents challenges due to the complex geometry of porous materials and the interplay between fluid flow and heat transfer. Accurate simulation and prediction of these phenomena often require high-performance computing and advanced numerical techniques.

In the past decade, significant progress has been made in this field, particularly with regard to the low Mach number approximation. This approximation has paved the way for new insights into understanding and leveraging the complexities of convection in porous media.

Gray and Giorgini [26] introduced a novel method for deriving approximate equations governing natural convection flows. This approach allows for the explicit identification of terms that can be neglected and establishes conditions under which the conventional Boussinesq approximation is applicable to both liquids and gases.

In a review by **Stauffer et al.** [51] on thermally driven convection in porous media, it was revealed that air exhibits a critical Rayleigh number of $4\pi^2$. However, the thermal gradient decreases due to adiabatic effects. Finite amplitude analysis predicted the onset of convection in air-filled porous media, and the resulting Ra vs. Nu curves aligned with experimental data for water.

Peirotti et al. [52] investigated the validity of the Boussinesq approximation in natural convection within a fluid-saturated porous cavity with insulated walls. Numerical calculations were performed for water and air, considering various Rayleigh numbers and aspect ratios. The findings demonstrated significant differences between the Nusselt numbers obtained using the Boussinesq approximation and those predicted by the model

In recent years, there has been a growing body of literature dedicated to advancing our understanding of low Mach number natural convection in porous media. Researchers have focused on exploring the complexities of fluid-solid interactions, the influence of heterogeneity in porous structures, and the effects of porosity and permeability on convective heat and mass transport. The integration of numerical simulations and experimental investigations has played

a crucial role in validating and refining theoretical models, leading to more accurate predictions and the design of more efficient systems.

Lebeau et al. [53] proposed a numerical model for convective heat and mass transport in both compressible and incompressible gas flows with soil-water phase change. The model considered adiabatic processes of compression heating and expansion cooling, allowing the inherently compressible gaseous phase to be treated as incompressible. The method employed a Galerkin finite element formulation with adaptive mesh refinement and dynamic time step control. The significance of this model became evident as the thermal gradient approached the adiabatic gradient, indicating that pore-air compressibility could not be ignored in medium to large-sized enclosures with small temperature differentials.

Johnson et al. [54] investigated numerical models of flow in unsaturated porous media, focusing specifically on the use of retention functions to account for capillary effects. However, many porous systems undergo changes in porosity, which in turn affect the retention function during the simulation. To address this issue, they introduced a new retention function that updates the maximum capillary pressure, residual saturation, and maximum saturation before applying the saturation fit. This correction helped rectify unphysical model behaviors and led to significant changes in simulation outcomes, particularly in systems dominated by capillary effects. The porosity-dependent retention function proved essential for obtaining meaningful simulation results in systems with varying porosity

Shankar et al. [55] investigated the linear stability of thermal buoyant flow in a fluid-saturated vertical porous slab, considering both weak and strong horizontal permeability heterogeneities. The study examined linear, quadratic, and exponential heterogeneity models and found Gill's proof to be ineffective. It presented neutral stability curves and calculated the critical Darcy-Rayleigh number for convective instability. The research highlighted both the similarities and differences between the various heterogeneity models concerning fluid flow stability

In their research, **Yan et al.** [56] explored the impact of low- or high-permeability inclusions on density-driven free convection in porous media. The study conducted sensitivity analyses using the modified Elder problem, focusing on permeability contrast, effective area, and distance. The results indicated that high-permeability inclusions had stronger effects due to unbalanced solute distributions, that larger effective areas influenced free convection, and that free convection was more sensitive to inclusions that were vertically closer. The findings also revealed that high-permeability inclusions had a more significant impact at the early stage, while those located far from the source zone exhibited a later impact. These insights contributed to the understanding of unstable density-driven flow and solute transport in porous media with structured heterogeneity

Barletta et al. [57] analyzed buoyancy-induced parallel flow in a cylindrical porous layer with an annular cross-section, assuming a radial thermal gradient originating from a uniformly distributed heat source. The study investigated the onset of convective instability by utilizing the heat-source Rayleigh number and the ratio between the internal and external radii.

Neutral stability curves and critical values were computed numerically, revealing that axisymmetric modes were the most critical type of instability.

I.5 NATURAL CONVECTION IN POROUS MEDIA WITH AN INTERNAL HEAT SOURCE

In the realm of natural convection within porous media, the introduction of internal heat generation adds a layer of complexity. The interaction between fluid dynamics and thermal processes becomes intricately intertwined as the porous matrix itself acts as a heat source, leading to significant implications across various fields. The presence of an internal heat source further complicates porous media convection, opening up diverse applications such as geothermal reservoir management, nuclear reactor safety protocols, and optimization of subsurface heat transport. Extensive research efforts have been devoted to understanding this phenomenon, as demonstrated by the study by Hardee et al. on heat transfer characteristics in fluid-saturated porous media. Their investigation combines analytical models with experimental data, and derives an approximate criterion for dry out in two-phase boiling heat transfer within stationary beds [58].

Furthermore, **Hdhiri et al.** [59] employed a numerical methodology to explore natural convection within a square cavity filled with a porous medium. Using the Darcy-Brinkman model, they predicted heat transfer within the porous material and obtained numerical solutions for varying Grashof, Prandtl, and Darcy numbers. Their research emphasized the significant impact of increasing Prandtl numbers on average Nusselt number values, noting that homogeneous media tended to overestimate heat transfer rates compared to porous media. Additionally, their work established valuable correlations for heat transfer rates in scenarios involving porous media.

Turkyilmazoglu published two papers. The first paper investigated free convection flow on a heated, vertically stretching permeable surface within a porous medium. The governing equations were transformed into self-similar nonlinear ordinary differential equations, which were solved analytically using exponential series. Closed-form solutions were obtained under specific conditions, providing insights into heat transfer mechanisms [60]. In the second paper, the author analyzed free convection flow of fluids in saturated porous media with a nonconstant heat flux at the wall and internal heat generation/absorption. The focus was on obtaining analytical solutions for the temperature field of the porous medium.

Closed-form solutions were found, revealing either unique or multiple solutions depending on whether the medium was cooling or heating. Thresholds for multiple solutions were determined, with algebraically decaying solutions dominating. The paper also validated the exact solutions through simplified real models. The results contributed to further research on free convecting flows in porous environments, emphasizing the need for justification of numerical methods [61].

Another study conducted by **El Ahmed et al.** [62] involved the numerical simulation of magnetohydrodynamic free convection and heat transfer in wavy enclosures filled with a heat-generating porous medium. The study employed complex models, including Buongiorno's

model with Brownian motion and thermophoresis for nanofluids, as well as the Darcy model for porous media. The wavy enclosure was subjected to an inclined magnetic field and a constant heat generation source. The system was numerically solved using an implicit finite difference method and compared with published data.

Shankar et al. [63] conducted a study on the stability of natural convection in a vertical layer of heat-generating Darcy porous medium with Oldroyd-B fluid, using a local thermal non-equilibrium (LTNE) model. This model incorporated two heat transport equations for the fluid and solid phases, accounting for uniform volumetric heating in both phases. The introduction of internal heating induced flow asymmetry, resulting in competing modes.

Khan et al. [64] investigated triple-diffusive free convection in porous chambers, with a specific focus on internal volumetric heat generation and temperature. The study examined square, trapezoidal, and triangular porous chambers, using different concentrations of NaCl and Sucrose as solutal components. The research explored the effects of internal heat generation rate, Rayleigh and Lewis numbers, buoyancy ratios, salt concentration, and Nusselt, Lewis, and Sherwood numbers. The triangular cavity exhibited the highest heat and mass transfer rates among the investigated configurations.

Rao et al. [65] studied natural convection in a wavy cavity involved in cooling a heat source with a constant heat flux. The non-dimensional governing equations were solved using a finite difference method. Parameters considered in the analysis included heater length, effective Rayleigh-Darcy number, and the waviness of the right vertical wall. The results indicated that convection in the wavy cavity depended primarily on ε only at high Ra, and a significant enhancement of convection was observed as the surface roughness increased.

Al-Amir et al. [66] conducted a study on the significance of natural convection and entropy generation in enclosures, particularly when using nanofluids and porous media. These processes enhanced heat transfer, fluid flow, and overall system performance. Optimizing them led to improvements in thermal management systems such as heat exchangers, electronic cooling systems, and renewable energy devices. The study focused on investigating entropy generation and natural convection in a Z-staggered cavity filled with a porous medium containing TiO_2-water nanofluid. The results demonstrated that increasing the Rayleigh number and nanoparticle volume fraction enhanced heat transmission, while decreasing the Darcy number and heat generation factor reduced the Nusselt number. The most effective streamline configuration was achieved at an inclination angle of 60 degrees.

Fereidooni's research focused on the free convection of Cu-H_2O nanofluid flow and heat transfer in a wavy circular porous domain using the finite element method (FEM). The study examined the influence of the shape factor of nanomaterials on flow and heat transfer characteristics. The results revealed that the average Nusselt number increased with the concentration of the nanofluid and the shape factor of the nanoparticles, while it could decrease by reducing the values of the wavy wall's contraction ratio A and the number of undulations D [67].

Collectively, these studies represent a significant body of research that not only enhances our understanding of natural convection in porous media but also provides practical insights for various applications, including geothermal energy extraction, nuclear reactor safety, and the optimization of subsurface heat transport. This research serves as a foundation for further exploration and underscores the importance of ongoing efforts to unravel the complexities of this captivating field.

Moreover, several studies have explored specific aspects of this phenomenon, including the effects of nanofluids and magnetohydrodynamics. Additionally, research has focused on the stability of natural convection in heat-generating porous media and the influence of surface or volumetric radiation on this phenomenon. These investigations have significantly advanced our understanding of the complexities associated with heat transfer and fluid flow within porous materials.

I.6 NATURAL CONVECTION IN POROUS MEDIA WITH SURFACE RADIATION

Surface radiation plays a crucial role in heat transfer within porous materials. These materials can induce fluid motion through natural convection driven by temperature differences. However, the presence of radiation emission and absorption on the surfaces of these materials adds complexity to the heat transfer process. The interaction between radiation and natural convection is significant in various fields, including geothermal energy, heat insulation, and environmental science. Depending on factors such as temperature variations and the radiative properties of the porous materials, radiation can either enhance or hinder natural convection.

Researchers use mathematical models, computer simulations, and experimental studies to examine how radiation affects heat transfer rates and fluid flow in porous materials. These studies aim to develop more energy-efficient systems and improve materials for various applications, ranging from underground energy storage to nuclear reactors

In a study by Yih [68], numerical solutions were presented for the influence of radiation on natural convection in an isothermal vertical cylinder embedded in a saturated porous medium. The Keller box method was employed to transform the partial differential equations into non-similar boundary layer equations. The results showed that the local Nusselt number increased with the transverse curvature parameter ξ, and the local heat transfer rate rose with the conduction-radiation parameter Rd and the surface excess temperature rate H.

Hossain et al. [69] examined the effect of radiation on the flow of optically dense, viscous, incompressible fluid induced by Darcy's buoyancy on a heated inclined flat surface. They employed the Keller box elimination method, the implicit finite difference method, and the Rosseland diffusion approximation. The results showed that the local Nusselt number increased with the buoyancy parameter. The study also demonstrated the impacts of the surface temperature excess ratio and the conduction-radiation parameter.

Scarella et al. [70] expanded the investigation of the interaction between natural convection and radiation heat transfer in a differentially heated cavity to the low Mach number approximation in 3D for both transparent and participating media. They solved the Navier-

Stokes and energy equations using the finite volume method and the discrete ordinates method. The work was validated using the Boussinesq approximation and simulations.

Gorla and Bakier [71] examined radiation and convection heat transfer in porous media using Darcy's model. They considered a rectangular profile fin with three types of fins: a long fin, a finite-length fin with an insulated tip, and a finite-length fin with an exposed tip. The study discussed the effects of the porosity parameter S_h, the radiation parameter G, and the temperature ratio C_T on temperature distribution and heat transfer rate. The results showed that radiation transferred more heat compared to a similar model without radiation.

Darvishi [72] investigated convection heat transfer in porous media using the homotopy analysis method (HAM). The study considered a rectangular profile fin with three types: long, finite, and exposed. The heat transfer equation was formulated using Darcy's model, and the effects of porosity, radiation, and temperature parameters were analyzed. The results showed that radiation transferred more heat compared to a similar model without radiation. The auxiliary parameter in the HAM was derived using the averaged residual error concept, which reduced computational time. The study found that the base heat flow increased with medium permeability and buoyancy effects and was enhanced by surface radiation or the tip Biot number.

The work of El-Kabeir et al. [73] investigates the effect of thermal radiation and nonlinear Forchheimer terms on boundary-layer flow and heat transfer from a vertical cylinder in a porous medium with nanofluids. A model was created, and the governing equations were numerically solved. Parametric research was conducted after comparisons with earlier work indicated a high level of agreement.

Xu [74] investigated the utilization of nanofluids and metal foam in thermal engineering to enhance heat transfer rates. Metal foam offered advantages such as low weight, high specific surface area, and thermal conductivity. Nanofluids, with their increased thermal conductivity, served as effective heat transfer mediums. The study examined the flow and heat transfer modes of nanofluids, metal foam, and their combination, aiming to urge researchers to focus on fundamental transport concepts for improving heat transfer in porous media. This understanding could contribute to enhancing the performance of miniaturized heat exchangers and heat sinks used for electronics cooling.

In their article, Badruddin et al. [75] presented a comprehensive review of recent research on heat transfer in porous media, focusing on various geometrical shapes such as vertical plates, cavities, and cylindrical shapes. The review encompassed phenomena such as natural convection, mixed convection, thermal equilibrium, and thermal non-equilibrium. Despite more than a century of research, new discoveries continue to deepen our understanding of porous media, highlighting its significance in various applications.

I.7 CONCLUSION

Natural convection, particularly within square cavities, is of significant importance in engineering applications such as electronic component cooling, solar energy capture, and room ventilation. Extensive research has been conducted on cavity geometries, as well as on factors

like rotation, fluid properties, and the development of numerical models to simulate these processes. Although the Boussinesq approximation is a fundamental approach, its limitations have led to the exploration of alternative methods, such as the low Mach number Approximation. These advancements have greatly enhanced our understanding of heat transfer and fluid dynamics, with practical applications in both engineering and environmental science.

The study of natural convection in porous media is a complex, multidisciplinary field that has made substantial progress over the years. It involves intricate interactions between fluids and solids, as well as various mechanisms of heat transfer. Darcy's law is commonly used to represent porous media, describing the relationship between fluid velocity and the pressure gradient within the medium. The low Mach number approximation can be seamlessly integrated into Darcy's law to account for low-speed, incompressible flows.

Heat transfer in porous media involves conduction through the solid matrix and convection through fluid-filled pores. The low Mach number approximation simplifies the fluid flow aspect of this heat transfer, allowing for a more accurate depiction of natural convection patterns within the porous material.

Mathematical modeling and numerical simulation are tools used to study the impact of factors such as surface radiation, internal heat generation, and nanofluids on heat transfer rates and fluid flow within porous media. They allow for the examination of interactions between parameters such as temperature, porosity, radiation intensity, and fluid properties in these media. These interactions are crucial in advancing our understanding of natural convection in radiation-influenced environments. The integration of the low Mach number Approximation will further expand the field of study, providing valuable practical insights.

Internal heat generation within porous media is a phenomenon that can significantly influence natural convection patterns. Understanding how heat sources affect fluid motion and temperature distribution is essential for optimizing systems and processes. Consequently, we have relied on mathematical modeling and numerical simulations to explore the intricacies of natural convection in these contexts, providing valuable insights into heat transfer rates and fluid flow patterns.

This comprehensive review aims to synthesize the latest developments and trends in the study of low Mach number natural convection in porous media, providing an up-to-date resource. We delve into the theoretical foundations of this approximation and explore key findings in the field. By doing so, we hope to offer researchers, engineers, and scientists a valuable reference for understanding the complexities of convection in porous materials and designing innovative solutions that leverage the low Mach number approximation

References

[1] N.A. Khan, O.I. Khalaf, C.A.T. Romero, M. Sulaiman, M.A. Bakar, Application of Euler Neural Networks with Soft Computing Paradigm to Solve Nonlinear Problems Arising in Heat Transfer, Entropy. 23 (2021) 1053. https://doi.org/10.3390/e23081053.

[2] Z.Z. Rashed, S.E. Ahmed, Z. a. S. Raizah, Thermal dispersion and buongiorno's nanofluid model enclosure partially filled with heat generating porous medium, J. Porous Media. 23 (2020). https://doi.org/10.1615/JPorMedia.2020026476.

[3] M.A. Mansour, S.E. Ahmed, A.M. Aly, Z.A.S. Raizah, Z. Morsy, Triple convective flow of micropolar nanofluids in double lid-driven enclosures partially filled with LTNE porous layer under effects of an inclined magnetic field, Chin. J. Phys. 68 (2020) 387–405. https://doi.org/10.1016/j.cjph.2020.10.001.

[4] H. Kavoosi Balotaki, H. Havaasi, H. Khakrah, P. Hooshmand, D. Ross, WITHDRAWN: Modelling of free convection heat transfer in a triangular cavity equipped using double distribution functions (DDF) lattice Boltzmann method (LBM), Therm. Sci. Eng. Prog. (2020) 100495. https://doi.org/10.1016/j.tsep.2020.100495.

[5] S.E. Ahmed, A.K. Hussein, M.A. Mansour, Z.A.S. Raizah, X. Zhang, MHD mixed convection in trapezoidal enclosures filled with micropolar nanofluids, Nanosci. Technol. Int. J. 9 (2018). https://doi.org/10.1615/NanoSciTechnolIntJ.2018026118.

[6] M.S. Sadeghi, T. Tayebi, A.S. Dogonchi, T. Armaghani, P. Talebizadehsardari, Analysis of hydrothermal characteristics of magnetic Al2O3-H2O nanofluid within a novel wavy enclosure during natural convection process considering internal heat generation, Math. Methods Appl. Sci. n/a (n.d.). https://doi.org/10.1002/mma.6520.

[7] M.S. Sadeghi, T. Tayebi, A.S. Dogonchi, M.K. Nayak, M. Waqas, Analysis of thermal behavior of magnetic buoyancy-driven flow in ferrofluid–filled wavy enclosure furnished with two circular cylinders, Int. Commun. Heat Mass Transf. 120 (2021) 104951. https://doi.org/10.1016/j.icheatmasstransfer.2020.104951.

[8] M.S. Sadeghi, N. Anadalibkhah, R. Ghasemiasl, T. Armaghani, A.S. Dogonchi, A.J. Chamkha, H. Ali, A. Asadi, On the natural convection of nanofluids in diverse shapes of enclosures: an exhaustive review, J. Therm. Anal. Calorim. 147 (2022) 1–22. https://doi.org/10.1007/s10973-020-10222-y.

[9] G. De Vahl Davis, I.P. Jones, Natural convection in a square cavity: A comparison exercise, Int. J. Numer. Methods Fluids. 3 (1983) 227–248. https://doi.org/10.1002/fld.1650030304.

[10] A. Mazgar, F. Hajji, K. Jarray, F. Nejma, Conjugate non-Gray Gas Radiation Combined with Natural Convection inside a Square Cavity with Internal Heat Source: Entropy Generation, 2019.

[11] W. Elenbaas, Heat dissipation of parallel plates by free convection, Physica. 9 (1942) 1–28. https://doi.org/10.1016/S0031-8914(42)90053-3.

[12] S. Ostrach, Natural Convection in Enclosures, in: J.P. Hartnett, T.F. Irvine (Eds.), Adv. Heat Transf., Elsevier, 1972: pp. 161–227. https://doi.org/10.1016/S0065-2717(08)70039-X.

[13] S. Ostrach, Natural Convection in Enclosures, J. Heat Transf. 110 (1988) 1175–1190. https://doi.org/10.1115/1.3250619.

[14] G.K. Batchelor, Heat transfer by free convection across a closed cavity between vertical boundaries at different temperatures, Q. Appl. Math. 12 (1954) 209–233. https://doi.org/10.1090/qam/64563.

[15] T.M. Shih, A Literature Survey on Numerical Heat Transfer, Numer. Heat Transf. 5 (1982) 369–420. https://doi.org/10.1080/10407788208913456.

[16] B. Gebhart, Y. Jaluria, R. Mahajan, B. Sammakia, M. Yovanovich, Buoyancy-Induced Flows and Transport, in: 1988. https://doi.org/10.1115/1.3226555.

[17] P.S. Reddy, P. Sreedevi, Buongiorno's model nanofluid natural convection inside a square cavity with thermal radiation, Chin. J. Phys. 72 (2021) 327–344. https://doi.org/10.1016/j.cjph.2020.08.016.

[18] R. Hassanzadeh, R. Rahimi, A. Khosravipour, S. Mostafavi, H. Pekel, Analysis of natural convection in a square cavity in the presence of a rotating cylinder with a specific number of roughness components, Int. Commun. Heat Mass Transf. 116 (2020) 104708. https://doi.org/10.1016/j.icheatmasstransfer.2020.104708.

[19] Z. Rui, J. Li, J. Ma, H. Cai, B. Nie, H. Peng, Comparative study on natural convection melting in square cavity using lattice Boltzmann method, Results Phys. 18 (2020) 103274. https://doi.org/10.1016/j.rinp.2020.103274.

[20] M. Leporini, F. Corvaro, B. Marchetti, F. Polonara, M. Benucci, Experimental and numerical investigation of natural convection in tilted square cavity filled with air, Exp. Therm. Fluid Sci. 99 (2018) 572–583. https://doi.org/10.1016/j.expthermflusci.2018.08.023.

[21] R. Hidki, L. El Moutaouakil, Z. Charqui, M. Boukendil, Z. Zrikem, Natural convection in a square cavity containing two heat-generating cylinders with different geometries, Mater. Today Proc. 45 (2021) 7415–7423. https://doi.org/10.1016/j.matpr.2021.01.626.

[22] P. Karki, A.K. Yadav, D. Arumuga Perumal, Study of Adiabatic Obstacles on Natural Convection in a Square Cavity Using Lattice Boltzmann Method, J. Therm. Sci. Eng. Appl. 11 (2019). https://doi.org/10.1115/1.4041875.

[23] P. Mayeli, G.J. Sheard, Buoyancy-driven flows beyond the Boussinesq approximation: A brief review, Int. Commun. Heat Mass Transf. 125 (2021) 105316. https://doi.org/10.1016/j.icheatmasstransfer.2021.105316.

[24] Livre : Boussinesq - Théorie analytique de la chaleur, Tome 2, 1903.djvu - Wikisource, (n.d.).https://fr.wikisource.org/wiki/Livre:Boussinesq

[25] J.M. Lopez, F. Marques, M. Avila, The Boussinesq approximation in rapidly rotating flows, J. Fluid Mech. 737 (2013) 56–77. https://doi.org/10.1017/jfm.2013.558.

[26] D.D. Gray, A. Giorgini, The validity of the boussinesq approximation for liquids and gases, Int. J. Heat Mass Transf. 19 (1976) 545–551. https://doi.org/10.1016/0017-9310(76)90168-X.

[27] E. Turkel, Preconditioning Techniques in Computational Fluid Dynamics, Annu. Rev. Fluid Mech. 31 (1999) 385–416. https://doi.org/10.1146/annurev.fluid.31.1.385.

[28] S. Cherkasov, A. Anan'ev, L. Moiseeva, Limitations of the Boussinesq Model on the Example of Laminary Natural Convection of Gas between Vertical Isothermal Walls, High Temp. 56 (2018) 878–883. https://doi.org/10.1134/S0018151X18060081.

[29] (17) (PDF) Numerical study of combined natural convection-surface radiation in a square cavity,(n.d.).https://www.researchgate.net/publication/281909148_Numerical_study_of_combined_natural_convection-surface_radiation_in_a_square_cavity

[30] P. Mayeli, G.J. Sheard, A centrifugal buoyancy formulation for Boussinesq-type natural convection flows applied to the annulus cavity problem, Int. J. Numer. Methods Fluids. 93 (2021) 683–702. https://doi.org/10.1002/fld.4904.

[31] N. Laaroussi, G. Lauriat, G. Desrayaud, Effects of variable density for film evaporation on laminar mixed convection in a vertical channel, Int. J. Heat Mass Transf. 52 (2009) 151–164. https://doi.org/10.1016/j.ijheatmasstransfer.2008.05.022.

[32] S. Rath, Complex interplay of power-law rheology and non-Oberbeck-Boussinesq effects on natural convection heat transfer in a confined domain, Int. J. Heat Mass Transf. 176 (2021) 121462. https://doi.org/10.1016/j.ijheatmasstransfer.2021.121462.

[33] S.R. Sondur, A.M. Mescher, Natural convection of Boussinesq and non-Boussinesq airflows simulated in a tall annular cavity, Numer. Heat Transf. Part Appl. 0 (2022) 1–27. https://doi.org/10.1080/10407782.2022.2105121.

[34] Y. Zhou, M. Wang, Y. Wang, Predictive accuracy of Boussinesq approximation in opposed mixed convection with a high-temperature heat source inside a building, Build. Environ. 144 (2018) 349–356. https://doi.org/10.1016/j.buildenv.2018.08.043.

[35] Using the Boussinesq Approximation for Natural Convection, COMSOL. (n.d.). https://www.comsol.com/blogs.

[36] S. Hamimid, Simulation numérique de la convection naturelle couplée au rayonnement ou à un champ magnétique dans l'approximation faible nombre de Mach, Thesis, 2018. http://dspace.univ-setif.dz:8888/jspui/handle/123456789/1159 (accessed October 3, 2022).

[37] E.A. Spiegel, G. Veronis, On the Boussinesq Approximation for a Compressible Fluid., Astrophys. J. 131 (1960) 442. https://doi.org/10.1086/146849.

[38] J.M. Mihaljan, A Rigorous Exposition of the Boussinesq Approximations Applicable to a Thin Layer of Fluid., Astrophys. J. 136 (1962) 1126. https://doi.org/10.1086/147463.

[39] Natural convection in an enclosed vertical air layer with large horizontal temperature differences | Journal of Fluid Mechanics | Cambridge Core, (n.d.). https://www.cambridge.org/core/journals/journal-of-fluid-mechanics

[40] S. Paolucci, On the Filtering of Sound from the Navier–Stokes Equations, NASA STIRecon Tech. Rep. N. 83 (1982) 26036.

[41] C. Rey, Analyse des effets de variation de volume des gaz dans les équations générales de bilan, Int. J. Heat Mass Transf. 43 (2000) 4311–4326. https://doi.org/10.1016/S0017-9310(00)00048-X.

[42] M. Pons, P. Le Quéré, An example of entropy balance in natural convection, Part 1: the usual Boussinesq equations, Comptes Rendus Mécanique. 333 (2005) 127–132. https://doi.org/10.1016/j.crme.2004.11.011.

[43] M. Pons, P. Le Quéré, An example of entropy balance in natural convection, Part 2: the thermodynamic Boussinesq equations, Comptes Rendus Mécanique. 333 (2005) 133–138. https://doi.org/10.1016/j.crme.2004.11.003.

[44] M. Pons, P. Le Quéré, Modeling natural convection with the work of pressure-forces: a thermodynamic necessity, Int. J. Numer. Methods Heat Fluid Flow. 17 (2007) 322–332. https://doi.org/10.1108/09615530710730184.

[45] M. Pons, Les routes vers l'équilibre en convection naturelle - le travail des forces de pression., 1 (2009) 6.

[46] H. Paillere, C. Viozat, A. Kumbaro, I. Toumi, Comparison of low Mach number models for natural convection problems, Heat Mass Transf. 36 (2000) 567–573. https://doi.org/10.1007/s002310000116.

[47] S. Jagannathan, D.A. Donzis, Reynolds and Mach number scaling in solenoidally-forced compressible turbulence using high-resolution direct numerical simulations, J. Fluid Mech. 789 (2016) 669–707. https://doi.org/10.1017/jfm.2015.754.

[48] T. Arima, Numerical Methods for Chemically Reacting Fluid Flow Computation under Low-Mach Number Approximation, Tokyo J. Math. 29 (2006) 167–198. https://doi.org/10.3836/tjm/1166661873.

[49] S. Boscarino, G. Russo, L. Scandurra, All Mach Number Second Order Semi-implicit Scheme for the Euler Equations of Gas Dynamics, J. Sci. Comput. 77 (2018) 850–884. https://doi.org/10.1007/s10915-018-0731-9.

[50] Y. Zhang, Y. Cao, A numerical study on the non-Boussinesq effect in the natural convection in horizontal annulus, Phys. Fluids. 30 (2018) 040902. https://doi.org/10.1063/1.5010864.

[51] P.H. Stauffer, L.H. Auer, N.D. Rosenberg, Compressible gas in porous media: a finite amplitude analysis of natural convection, Int. J. Heat Mass Transf. 40 (1997) 1585–1589. https://doi.org/10.1016/S0017-9310(96)00222-0.

[52] M.B. Peirotti, M.D. Giavedoni, J.A. Deiber, Natural convective heat transfer in a rectangular porous cavity with variable fluid properties—validity of the Boussinesq approximation, Int. J. Heat Mass Transf. 30 (1987) 2571–2581. https://doi.org/10.1016/0017-9310(87)90138-4.

[53] M. Lebeau, J.-M. Konrad, Natural convection of compressible and incompressible gases in undeformable porous media under cold climate conditions, Comput. Geotech. 36 (2009) 435–445. https://doi.org/10.1016/j.compgeo.2008.04.005.

[54] P.J. Johnson, G.A. Zyvoloski, P.H. Stauffer, Impact of a Porosity-Dependent Retention Function on Simulations of Porous Flow, Transp. Porous Media. 127 (2019) 211–232. https://doi.org/10.1007/s11242-018-1188-x.

[55] B.M. Shankar, I.S. Shivakumara, Gill's stability problem may be unstable with horizontal heterogeneity in permeability, J. Fluid Mech. 943 (2022) A20. https://doi.org/10.1017/jfm.2022.411.

[56] M. Yan, C. Lu, J. Yang, Y. Xie, J. Luo, Impact of Low- or High-Permeability Inclusion on Free Convection in a Porous Medium, Geofluids. 2019 (2019) e8609682. https://doi.org/10.1155/2019/8609682.

[57] A. Barletta, D.A.S. Rees, B. Pulvirenti, Buoyant flow instability induced by a uniform internal heat source in a vertical annular porous layer, Int. J. Heat Mass Transf. 194 (2022) 122935. https://doi.org/10.1016/j.ijheatmasstransfer.2022.122935.

[58] H.C. Hardee, R.H. Nilson, Natural Convection in Porous Media with Heat Generation, Nucl. Sci. Eng. 63 (1977) 119–132. https://doi.org/10.13182/NSE77-A27015.

[59] N. Hdhiri, B. Souayeh, H. Alfannakh, B.B. Beya, Natural Convection Study with Internal Heat Generation on Heat Transfer and Fluid Flow Within a Differentially Heated Square Cavity Filled with Different Working Fluids and Porous Media, BioNanoScience. 9 (2019) 702–722. https://doi.org/10.1007/s12668-019-00626-y.

[60] EBSCOhost | 134980808 | MHD natural convection in saturated porous media with heat generation/absorption and thermal radiation: closed-form solutions., (n.d.). https://web.s.ebscohost.com

[61] M. Turkyilmazoglu, Multiple exact solutions of free convection flows in saturated porous media with variable heat flux, J. Porous Media. 25 (2022). https://doi.org/10.1615/JPorMedia.2022041870.

[62] S.E. Ahmed, Z.Z. Rashed, MHD natural convection in a heat generating porous medium-filled wavy enclosures using Buongiorno's nanofluid model, Case Stud. Therm. Eng. 14 (2019) 100430. https://doi.org/10.1016/j.csite.2019.100430.

[63] B.M. Shankar, I.S. Shivakumara, S.B. Naveen, Impact of Thermal Non-equilibrium on the Stability of Natural Convection in an Oldroyd-B Fluid-Saturated Vertical Porous Layer with Internal Heat Sources, Transp. Porous Media. 133 (2020) 437–458. https://doi.org/10.1007/s11242-020-01431-y.

[64] Z.H. Khan, W.A. Khan, M.A. Sheremet, Enhancement of heat and mass transfer rates through various porous cavities for triple convective-diffusive free convection, Energy. 201 (2020) 117702. https://doi.org/10.1016/j.energy.2020.117702.

[65] P.S. Rao, P. Barman, Natural convection in a wavy porous cavity subjected to a partial heat source, Int. Commun. Heat Mass Transf. 120 (2021) 105007. https://doi.org/10.1016/j.icheatmasstransfer.2020.105007.

[66] Q.R. Al-Amir, H.K. Hamzah, F.H. Ali, M. Hatami, W. Al-Kouz, A. Al-Manea, R. Al-Rbaihat, A. Alahmer, Investigation of Natural Convection and Entropy Generation in a Porous Titled Z-Staggered Cavity Saturated by TiO2-Water Nanofluid, Int. J. Thermofluids. 19 (2023) 100395. https://doi.org/10.1016/j.ijft.2023.100395.

[67] J. Fereidooni, Free convection analysis for a nanofluid in a wavy porous domain subject to shape of nanoparticle and internal heat generation, Int. J. Mod. Phys. B. (2023) 2450194. https://doi.org/10.1142/S0217979224501947.

[68] K.A. Yih, Radiation effect on natural convection over a vertical cylinder embedded in porous media, Int. Commun. Heat Mass Transf. 26 (1999) 259–267. https://doi.org/10.1016/S0735-1933(99)00012-3.

[69] M.A. Hossain, I. Pop, Radiation effect on Darcy free convection flow along an inclined surface placed in porous media, Heat Mass Transf. 32 (1997) 223–227. https://doi.org/10.1007/s002310050115.

[70] G. Scarella, G. Accary, S. Meradji, D. Morvan, O.A. Bessonov, Three-dimensional numerical simulation of the differentially heated cavity in the Low Mach Number approximation, in: Begel House Inc., 2008. https://doi.org/10.1615/ICHMT.2008.CHT.740.

[71] R.S.R. Gorla, A.Y. Bakier, Thermal analysis of natural convection and radiation in porous fins, Int. Commun. Heat Mass Transf. 38 (2011) 638–645. https://doi.org/10.1016/j.icheatmasstransfer.2010.12.024.

[72] M.T. Darvishi, R.S.R. Gorla, F. Khani, Natural convection and radiation in porous fins, Int. J. Numer. Methods Heat Fluid Flow. 23 (2013) 1406–1420. https://doi.org/10.1108/HFF-12-2011-0264.

[73] S.M.M. EL-Kabeir, A.J. Chamkha, A.M. Rashad, Effect of thermal radiation on non-Darcy natural convection from a vertical cylinder embedded in a nanofluid porous media, J. Porous Media. 17 (2014). https://doi.org/10.1615/JPorMedia.v17.i3.70.

[74] H.J. Xu, Z.B. Xing, F.Q. Wang, Z.M. Cheng, Review on heat conduction, heat convection, thermal radiation and phase change heat transfer of nanofluids in porous media: Fundamentals and applications, Chem. Eng. Sci. 195 (2019) 462–483. https://doi.org/10.1016/j.ces.2018.09.045.

[75] I.A. Badruddin, Azeem, T.M. Yunus Khan, M.A. Ali Baig, Heat Transfer in Porous Media: A Mini Review, Mater. Today Proc. 24 (2020) 1318–1321. https://doi.org/10.1016/j.matpr.2020.04.447.

II.1 INTRODUCTION

In this chapter, we explore the fascinating world of fluid mechanics, where we study the behavior of different types of fluids like water and air. We start by developing a set of equations that help us understand how these fluids move and change over time. As we go through the chapter, we break down these equations into simpler forms to make them easier to work with. We also discuss the assumptions we make about the flows, like assuming the density stays constant or that the flow is one-dimensional. By understanding these basic principles, we can gain a better understanding of how fluids behave and open the door to more advanced studies in fluid dynamics.

II.2 CONSERVATION EQUATIONS

The state of flow of a fluid is characterized by its velocity vector $\vec{V}$, density ρ , pressure p , and temperature T . The velocity vector $\vec{V}$ components are denoted as u ,v in the x , y and z directions, respectively. Assuming that the internal properties μ, λ, c_v , c_p , namely density and temperature, are known, equations exist to determine the values of the six dependent variables u ,v ,w , ρ, p ,T as functions of time and space x , y , z and t . The balance equations governing the fluid motion in a spatial domain consist of three conservation laws, along with the fluid's equation of state:

- Conservation of mass, which ensures the conservation of mass for fluid particles.
- Conservation of momentum, which applies Newton's law to fluid particles.
- Conservation of energy, which states that energy cannot be created or destroyed and preserves the energy of fluid particles.
- The thermodynamic equation of state (or constitutive equation), which establishes a relationship between the state variables $f(p, \rho, T)$.

II.2.1 Compressible Flow

This model, which does not involve approximations, is the most comprehensive and can be used to accurately describe flows with high compression ratios.

II.2.1.1 Conservation Equations

By disregarding heat loss through radiation, we can derive a system of six equations [1,2] for a two-dimensional compressible flow of a viscous Newtonian fluid that satisfies Stokes' hypothesis and the perfect gas law. Assuming that the only volume force present is gravity $\vec{F} = \vec{g}$, the equations are detailed in Appendix I:

- Continuity equation:

$$\frac{\partial \rho}{\partial t} + \nabla.(\rho \vec{V}) = 0 \qquad \text{(II.1)}$$

- Momentum equation:

$$\rho\left(\left(\vec{V}\nabla\right)\vec{V}+\frac{\partial\vec{V}}{\partial t}\right)=\rho\vec{g}-\nabla p+\nabla.\mu\nabla\vec{V}+\frac{1}{3}\nabla\mu\nabla\vec{V} \quad \text{(II.2)}$$

- Energy equation:

$$\rho c_p\left(\frac{\partial T}{\partial t}+\left(\vec{V}\nabla\right)T\right)=r+\nabla.k\nabla T+\frac{dp}{dt}+\nabla\vec{V}:\bar{\bar{\tau}} \quad \text{(II.3)}$$

- State equation:

$$p=\rho RT \quad \text{(II.4)}$$

Equations (II.1-II.4) are universally applicable and hold true regardless of variations in physical properties related to pressure and temperature. Furthermore, it is feasible to establish a set of simpler equations, although their scope is more limited, that correspond to various specific cases.

II.2.2.2 Summary of the Equations

In the low Mach number approximation, we have $Ma \ll 1$. Therefore, terms of order higher than or equal to Ma^2 can be neglected in the continuity, energy, and state equations. The momentum equation is solved at the order $o\left(Ma^2\right)$, resulting in the simplified equations that govern low Mach number flows.

$$\frac{\partial\rho^{(0)}}{\partial t^*}+\nabla.\rho^{(0)}v^{(0)}=0 \quad \text{(II.5)}$$

$$\nabla p^{(0)}=0 \quad \text{(II.6)}$$

$$\rho^{(0)}\frac{\partial v^{(0)}}{\partial t^*}+\rho^{(0)}\left(v^{(0)}\nabla\right)v^{(0)}=\frac{1}{Fr}\rho^{(0)}\overrightarrow{g^*}-\frac{1}{\gamma}\nabla p^{(1)}+\mathrm{Re}^{-1}\nabla.\mu^{(0)}\nabla v^{(0)}+\frac{1}{3}\mathrm{Re}^{-1}\nabla\mu^{(0)}\nabla v^{(0)} \quad \text{(II.8)}$$

$$\rho^{(0)}c_p{}^{(0)}\left(\frac{\partial T^{(0)}}{\partial t^*}+v^{(0)}\nabla T^{(0)}\right)=Pe^{-1}\left(\nabla.k^{(0)}\nabla T^{(0)}\right)+\frac{\gamma-1}{\gamma}\frac{dp^{(0)}}{dt^*} \quad \text{(II.9)}$$

$$p^{(0)}=\rho^{(0)}T^{(0)} \quad \text{(II.10)}$$

II.2.2.3 Redimensioning the conservation equations

To reestablish the conservation equations in dimensional form, we utilize the velocity scale and the pressure scale. The dimensionless variables can be expressed as follows:

$$x^*=x/l_0;t^*=t/\left(l_0/U_f\right);V^{(0)}=V/U_f;p^{(1)}=\gamma p_{dyn}/\rho_0U_f^2;\rho^*=\rho/\rho_0;$$
$$\mu^*=\mu/\mu_0;k^*=k/k_0;T^*=T/T_0;c_p^*=c_p/c_{p0};g^*=g/g_0,p^{(0)}=\overline{p}/p_0$$

Finally, we obtain the conservation equations in the low Mach number approximation in dimensional form (omitting the superscripts "0" for simplicity):

$$\frac{\partial \rho}{\partial t} + \nabla . \rho V = 0 \tag{II.11}$$

$$\nabla \overline{p} = 0 \tag{II.12}$$

$$\rho\left(\frac{\partial V}{\partial t} + V\,\nabla V\right) = \rho\vec{g} - \nabla p_{dyn} + \nabla . \mu \nabla V + \frac{1}{3}\nabla \mu \nabla V \tag{II.13}$$

$$\rho c_p\left(\frac{\partial T}{\partial t} + V\,\nabla T\right) = \left(\nabla . k \nabla T\right) + \frac{d\,\overline{p}}{dt} \tag{II.14}$$

$$\overline{p} = \rho R T \tag{II.15}$$

In the particular case of constant density ρ, convection does not occur. Assuming that this state is represented by:

$\vec{V} = 0$, $\rho = \rho_0$, $p = p_0$ et $T = T_0$, equation (2.13) gives:

$$0 = \rho_0 \vec{g} - \nabla p_0 \tag{II.16}$$

With : $P_0 = \rho_0 g y$

Where a temperature difference exists, density changes with temperature. Pressure p_{dyn} can therefore be expressed as the sum of perturbed pressure p' and static pressure $P_0 = \rho_0 g y$:

$$p_{dyn} = p' + p_0 \tag{II.17}$$

The total pressure can therefore be written as: $p(\vec{x}, t) = p' + p_0 - \overline{p}(t)$

By subtracting equations (II.13) and (II.16), we can write:

$$\rho\left(\left(\vec{V}\nabla\right)\vec{V} + \frac{\partial \vec{V}}{\partial t}\right) = (\rho - \rho_0)\vec{g} - \nabla p' + \nabla . \mu \nabla \vec{V} + \frac{1}{3}\nabla \mu \nabla . \vec{V} \tag{II.18}$$

It is also assumed that the dynamic viscosity is either constant $\mu(T) = \mu(T_0) = \mu_0$ or given by Sutherland's law [7]:

$$\frac{\mu(T)}{\mu_0} = \left(\frac{T}{T_0}\right)^{3/2} \frac{T_0 + S_\mu}{T + S_\mu} \tag{II.19}$$

With $T_0 = 273k$, $S_\mu = 110.5K$, $\mu_0 = 1.68\times10^{-5} kg.m^{-1}.s^{-1}$ [8–10]. Thermal conductivity is given by:

$$k(T) = \mu(T)\frac{C_{p0}k_0}{\nu_0} \tag{II.20}$$

II.2.3 Dimensionalization of the Low Mach Number Equations

To ensure the generality of the solutions for numerical validation of the calculation code and comparison with literature results, the conservation equations of the low Mach number model are introduced with the following scaled variables:

$$\tau = \frac{\alpha t}{H^2},\ X = \frac{x}{H},\ Y = \frac{y}{H},\ U = \frac{uH}{\alpha}, V = \frac{vH}{\alpha}, \Pi = \frac{p'H^2}{\rho\alpha^2}, \overline{P} = \frac{\overline{p}}{\overline{p}_0},\ \theta = \frac{T - T_0}{\Delta T}$$ where:

$$\Delta T = T_H - T_C\ ,\ T_0 = \frac{T_H + T_C}{2}$$

Where: $\varepsilon_b = \Delta T / 2T_0$ represents a parameter that measures the temperature difference between the active walls.

The dimensionless thermophysical quantities are defined based on their values under reference conditions:

$\rho^* = \rho/\rho_0, \mu^* = \mu/\mu_0; k^* = k/k_0$ et $C_p^* = C_p/C_{p0} = 1$,[3].

Based on these considerations, we obtain the following system of dimensionless equations:

$$\frac{\partial\rho^*}{\partial\tau} + \frac{\partial\rho^* U}{\partial X} + \frac{\partial\rho^* V}{\partial Y} = 0 \tag{II.21}$$

$$\rho^*\left(\frac{\partial U}{\partial\tau} + U\frac{\partial U}{\partial X} + V\frac{\partial U}{\partial Y}\right) = -\frac{\partial\Pi}{\partial X} + \Pr\left\{\frac{\partial}{\partial X}\left(\mu^*\frac{\partial U}{\partial X}\right) + \frac{\partial}{\partial Y}\left(\mu^*\frac{\partial U}{\partial Y}\right) + \frac{1}{3}\nabla\mu^*\nabla\vec{V}\right\} \tag{II.22}$$

$$\rho^*\left(\frac{\partial V}{\partial\tau} + U\frac{\partial V}{\partial X} + V\frac{\partial V}{\partial Y}\right) = -\frac{\partial\Pi}{\partial Y} - Ra\Pr\frac{\rho^* - 1}{2\varepsilon_b} + \Pr\left\{\frac{\partial}{\partial X}\left(\mu^*\frac{\partial V}{\partial X}\right) + \frac{\partial}{\partial Y}\left(\mu^*\frac{\partial V}{\partial Y}\right) + \frac{1}{3}\nabla\mu^*\nabla\vec{V}\right\} \tag{II.23}$$

$$\rho^* c_p^*\left(\frac{\partial\theta}{\partial\tau} + U\frac{\partial\theta}{\partial X} + V\frac{\partial\theta}{\partial Y}\right) = \frac{\partial}{\partial X}\left(k^*\frac{\partial\theta}{\partial X}\right) + \frac{\partial}{\partial Y}\left(k^*\frac{\partial\theta}{\partial Y}\right) + \frac{\gamma-1}{2\varepsilon_b\gamma}\frac{d\overline{P}}{dt} \tag{II.24}$$

$$\rho^* = \frac{\overline{P}}{(2\varepsilon_b\theta + 1)} \tag{II.25}$$

The dynamic viscosity and thermal conductivity become:

$$\mu^* = (2\varepsilon_b\theta + 1)^{3/2}\frac{(1 + S_\mu/T_0)}{2\varepsilon_b\theta + 1 + S_\mu/T_0} \tag{II.26}$$

$$k^*(\theta) = \frac{\mu^*(\theta)}{\mathrm{Pr}} \tag{II.27}$$

In addition to these equations, we have the dimensionless form of the equation of state, which is given by:

$$\rho^* = \frac{\overline{P}}{(2\varepsilon_b \theta + 1)} \tag{II.28}$$

When solving these equations numerically, the problem is that there are more unknowns than equations (at 2D, there are six unknowns). This is due to the pressure decomposition, which introduces thermodynamic pressure $\overline{p}$ (or $p^{(0)}$) as an additional unknown. In order to close the problem, we need an additional equation translating the initial state, which is the conservation of mass equation.

II.2.3.1 Calculation of $\overline{p}$

The thermodynamic pressure is the ambient pressure:

$$\overline{p}(t) = 1, \forall t \tag{II.29}$$

in an open cavity and is determined by the conservation of total mass:

$$\int_\Omega \rho d\Omega = M_0 = \int_\Omega \rho_0 d\Omega \ , \ \forall\ t \tag{II.30}$$

in a closed cavity. The volume of the system is denoted by Ω , and M_0 is defined as the initial mass of the system:

$$M_0 = \int_\Omega \rho_0 d\Omega = \frac{1}{R}\int_\Omega \frac{p_0}{T_0} d\Omega \tag{II.31}$$

From the equation of state, we obtain:

$$\rho = \frac{\overline{p}}{RT} \text{ and } \rho_0 = \frac{\overline{p}_0}{RT_0} \tag{II.32}$$

Integrating over a control volume, we have:

$$\int_\Omega \frac{\overline{p}}{RT} d\Omega = \int_\Omega \frac{p_0}{RT_0} d\Omega \quad \Rightarrow \quad \overline{p}\int_\Omega \frac{1}{T} d\Omega = p_0 \int_\Omega \frac{1}{T_0} d\Omega \tag{II.33}$$

Finally, we obtain the expression:

$$\bar{p} = p_0 \frac{\int_\Omega \frac{1}{T_0} d\Omega}{\int_\Omega \frac{1}{T} d\Omega} \tag{II.34}$$

II.2.3.2 Calculation of $\frac{d\bar{p}}{dt}$

The second additional equation is given by the calculation of the term $\frac{d\bar{p}}{dt}$. The conservation of mass equation, combined with the energy equation and the equation of state, allows us to write the divergence of velocity in the form given by equation (2.38). We have:

For the equation of state:

$$\frac{d\rho}{dt} = \frac{1}{RT}\frac{d\bar{p}}{dt} - \frac{\bar{p}}{RT^2}\frac{dT}{dt} \tag{II.35}$$

For the continuity equation:

$$\nabla.\vec{V} = -\frac{1}{\bar{p}}\frac{d\bar{p}}{dt} + \frac{1}{T}\frac{dT}{dt} \tag{II.36}$$

For the energy equation:

$$\frac{dT}{dt} = \rho c_p \frac{dT}{dt} = \frac{1}{\rho c_p}\nabla.k\nabla T + \frac{1}{\rho c_p}\frac{dp}{dt} \tag{II.37}$$

Combining equations (II.10) and (II.11), we have:

$$\nabla.\vec{V} = -\frac{1}{\bar{p}}\frac{d\bar{p}}{dt} + \frac{\gamma-1}{\rho\gamma RT}\nabla.k\nabla T + \frac{\gamma-1}{\rho\gamma RT}\frac{dp}{dt} \tag{II.38}$$

With:

$$c_p = \frac{\gamma R}{\gamma - 1}$$

Integrating over the control volume of equation (II.38), we get:

$$\int_\Omega \nabla.\vec{V}\, d\Omega = \int_{\Omega^*} \left\{ -\frac{1}{\bar{p}}\frac{d\bar{p}}{dt} + \frac{\gamma-1}{\bar{p}\gamma}\nabla.k\nabla T + \frac{\gamma-1}{\bar{p}\gamma}\frac{d\bar{p}}{dt} \right\} d\Omega \tag{II.39}$$

Applying the divergence theorem for impermeable wall conditions:

$$\int_{\Omega^*} \nabla.\vec{V}\, d\Omega = \int_S \vec{V}.\vec{n}.dS = 0 \tag{II.40}$$

We obtain:

$$\int_\Omega \frac{1}{\overline{p}} \frac{1}{\gamma} \frac{d\overline{p}}{dt} d\Omega = \int_\Omega \frac{\gamma - 1}{\overline{p}\gamma} \nabla.k \nabla T\, d\Omega \tag{II.41}$$

$\overline{p}$ only depends on time, thus:

$$\frac{1}{\gamma} \frac{d\overline{p}}{dt} \int_\Omega d\Omega = \frac{\gamma - 1}{\gamma} \int_\Omega \nabla.k \nabla T\, d\Omega \tag{II.42}$$

Using the divergence theorem:

$$\int_\Omega \nabla.k \nabla T d\Omega = \int_S k \nabla T dS = \int_S k \frac{\partial T}{\partial n} dS \tag{II.43}$$

Therefore:

$$\frac{1}{\gamma} \frac{d\overline{p}}{dt} \int_\Omega d\Omega = \frac{\gamma - 1}{\gamma} \int_S k \nabla T dS \tag{II.44}$$

Finally, we have:

$$\frac{d\overline{P}}{dt} = \frac{(\gamma - 1) \int_S k \nabla T dS}{\int_\Omega d\Omega} \tag{II.45}$$

By dimensioning the expressions of $\overline{p}$ and $\frac{d\overline{p}}{dt}$, we have:

$$\overline{P} = \frac{\int_\Omega d\Omega}{\int_\Omega \frac{1}{2\varepsilon_b \theta + 1} d\Omega} \tag{II.46}$$

$$\frac{d\overline{P}}{d\tau} = 2\varepsilon_b \gamma . \frac{1}{\int_\Omega d\Omega} . \int_S k \frac{\partial \theta}{\partial n} dS \tag{II.47}$$

In the case of the Boussinesq approximation, the dimensionless equations are as follows:

$$\frac{\partial U}{\partial X}+\frac{\partial V}{\partial Y}=0 \tag{II.48}$$

$$\frac{\partial U}{\partial \tau}+U\,\frac{\partial U}{\partial X}+v\,\frac{\partial U}{\partial Y}=-\frac{\partial \pi}{\partial X}+\Pr\left\{\frac{\partial^2 U}{\partial X^{2}}+\frac{\partial^2 U}{\partial Y^{2}}\right\} \tag{II.49}$$

$$\frac{\partial V}{\partial \tau}+U\,\frac{\partial V}{\partial X}+V\,\frac{\partial V}{\partial Y}=-\frac{\partial \pi}{\partial Y}+\Pr\left\{\frac{\partial^2 V}{\partial X^{2}}+\frac{\partial^2 V}{\partial Y^{2}}\right\}+Ra\,\Pr\,\theta \tag{II.50}$$

$$\frac{\partial \theta}{\partial \tau}+U\,\frac{\partial \theta}{\partial X}+V\,\frac{\partial \theta}{\partial Y}=\frac{\partial^2 \theta}{\partial X^{2}}+\frac{\partial^2 \theta}{\partial Y^{2}} \tag{II.51}$$

II.2.4 Incompressible Flow

In an incompressible flow, the density remains constant and uniform. This characteristic is reflected in the continuity equation, where the flow is considered isovolumetric: $\nabla.\vec{V}=0$.

This property also implies that pressure does not need to be interpreted as a thermodynamic quantity. In this approximation, we impose $\rho=\rho_0$ everywhere, effectively neutralizing the equation of state $p=p(\rho,T)$, which becomes meaningless. This approximation is equivalent to assuming that the speed of sound is infinitely greater than the flow velocity. Pressure, which was a thermodynamic quantity in compressible flows, becomes solely a dynamic quantity that satisfies the constraint.

In this case, we assume that the fluid properties (ρ,μ,k) are constant and equal to their values in the reference state. Additionally, we neglect the thermodynamic pressure gradient. These assumptions are valid for low Mach numbers, where the variations in p' and T are very small.

$$p_{dyn}=p'+p_0 \Rightarrow p'=p_{dyn}-\rho_0 g y \tag{II.52}$$

$$\Rightarrow(\rho-\rho_0)\vec{g}-\nabla p'=(\rho-\rho_0)\vec{g}-\nabla(p_{dyn}-\rho_0 g y)=\rho\vec{g}-\nabla p_{dyn} \tag{II.53}$$

The following incompressible equations result from simplification of the low Mach number equations:

$$\nabla.\vec{V}=0 \tag{II.54}$$

$$\left(\frac{\partial V}{\partial t}+V\,\nabla V\right)=\vec{g}-\frac{1}{\rho_0}\nabla p_{dyn}+v\Delta\vec{V} \tag{II.55}$$

$$\frac{\partial T}{\partial t}+V\,\nabla T=aT\,\Delta \tag{II.56}$$

The thermal problem and the dynamic problem are decoupled, allowing for separate solution. In the case where gravity can be neglected, the dilatable equations (Boussinesq equations) are identical to the incompressible equations, resulting in the decoupling of velocity and temperature.

II.2.5 Dilatable Flow (Boussinesq Approximation)

The assumption of an incompressible fluid is often too simplistic for certain flows, as it fails to account for changes in density caused by temperature variations. In the presence of gravity, these density changes give rise to an Archimedean force field that can induce fluid motion. However, it's important to note that this type of movement differs in nature from the sound waves that we typically want to filter out or ignore.

To incorporate these density variations while still considering the dominance of sound waves, we employ the Boussinesq approximation. This approximation assumes that the speed of sound waves is infinitely greater than the velocity of the flow. By doing so, we can capture the effects of density variations on fluid motion without explicitly accounting for the compressibility of the fluid.

In cases of natural convection where density variations within the fluid are small and flow velocities are relatively slow (low Mach number), the fluid can be treated as nearly incompressible. The Boussinesq approximation allows us to neglect density variations (ρ) except in the gravitational force, known as Archimedes' term, which drives thermo-convection. This hypothesis simplifies the analysis while still considering the essential influence of density variations on the fluid flow [11].

Therefore, we have:

$$\nabla . V = 0 \text{ And } \frac{d\bar{p}}{dt} = 0 \tag{II.57}$$

The equation system then becomes:

$$\nabla . V = 0 \tag{II.58}$$

$$\left(\vec{V}\nabla\right)\vec{V} + \frac{\partial \vec{V}}{\partial t} = \frac{(\rho - \rho_0)}{\rho_0}\vec{g} - \frac{1}{\rho_0}\nabla p' + \nu \nabla . \nabla \vec{V} \tag{II.59}$$

$$\frac{\partial T}{\partial t} + V\,\nabla T = aT\,\Delta \tag{II.60}$$

So, to use this approximation, the ratio between density variation and density must be small:
$\frac{\Delta\rho}{\rho} = \frac{(\rho - \rho_0)}{\rho_0} \ll 1$

In actual fact, this assumption involves simplifying the equation of fluid state by linearizing the expression of ρ as a function of temperature variations T , as follows:

$$\rho = \rho_0 + \left[\frac{\partial \rho}{\partial T}\right]_0 (T - T_0) \tag{II.61}$$

For a perfect gas:

$$\rho = \frac{p}{RT} \Rightarrow \frac{\partial \rho}{\partial T} = -\frac{\rho}{T} \tag{II.62}$$

This gives us:

$$\rho = \rho_0 + \left[-\frac{\rho}{T}\right]_0 (T - T_0) \tag{II.63}$$

$$\Rightarrow \quad \rho = \rho_0 - \frac{\rho_0}{T_0}(T - T_0) \tag{II.64}$$

And since: $\beta = -\frac{1}{\rho}\left(\frac{\partial \rho}{\partial T}\right)_{p=p_0} = \frac{1}{T_0}$ (for a perfect gas), we finally obtain:

$$\rho = \rho_0(1 - \beta(T - T_0))$$

Then, noting that the value of β is small and that temperature gradients are rarely very high, we can replace ρ by ρ_0 in all the terms of equations (II.11)-(II.14) (low Mach number equations) except in the gravity term (Archimedes term or buoyancy force), which is linearized as follows:

$$\rho\vec{g} = \rho_0\vec{g} - \rho_0\beta(T - T_0)\vec{g} \tag{II.65}$$

And the system of equations describing the natural convection flow of a Newtonian fluid, assumed to be a perfect gas, under Boussinesq's assumptions is:

$$\nabla . V = 0 \tag{II.66}$$

$$(\vec{V}\nabla)\vec{V} + \frac{\partial \vec{V}}{\partial t} = \beta(T - T_0)\vec{g} - \frac{1}{\rho_0}\nabla p' + \nu\nabla\vec{V} \tag{II.67}$$

$$\frac{\partial T}{\partial t} + V\,\nabla T = a\Delta T \tag{II.68}$$

In the present work, the flows considered are compressible flow with low Mach number and incompressible dilatable flow, or simply Boussinesq flow.

II.3 THE COMPOSITE FLUID/POROUS SYSTEM

The low Mach number approximation in the porous media equation enables efficient and accurate modeling of fluid flows through porous materials in various engineering applications. It facilitates simulations and analyses of phenomena such as groundwater flow, oil reservoir simulations, filtration processes, and heat transfer in porous media. By simplifying the equations while still accounting for essential flow characteristics, this approximation provides a valuable tool for understanding and predicting fluid behavior in porous media systems.

The governing equations for the system are expressed in a dimensional form [12].

Fluid region:

$$\frac{\partial \rho}{\partial t} + \frac{\partial \rho u}{\partial x} + \frac{\partial \rho v}{\partial y} = 0 \tag{II.69}$$

$$\rho\left(\frac{\partial u}{\partial t} + u\frac{\partial u}{\partial x} + v\frac{\partial u}{\partial y}\right) = -\frac{\partial \acute{p}}{\partial x} + \left[\frac{\partial}{\partial x}\left(\mu\frac{\partial u}{\partial x}\right) + \frac{\partial}{\partial y}\left(\mu\frac{\partial u}{\partial y}\right)\right] + \frac{1}{3}\left(\mu\frac{\partial^2 u}{\partial x^2} + \mu\frac{\partial^2 u}{\partial y^2}\right) \tag{II.70}$$

$$\rho\left(\frac{\partial v}{\partial t} + u\frac{\partial v}{\partial x} + v\frac{\partial v}{\partial y}\right) = -\frac{\partial \acute{p}}{\partial y} + \left[\frac{\partial}{\partial x}\left(\mu\frac{\partial v}{\partial x}\right) + \frac{\partial}{\partial y}\left(\mu\frac{\partial v}{\partial y}\right)\right] + \frac{1}{3}\left(\mu\frac{\partial^2 v}{\partial x^2} + \mu\frac{\partial^2 v}{\partial y^2}\right) - g(\rho - \rho_0) \tag{II.71}$$

$$(\rho Cp)_f\left(\frac{\partial T}{\partial t}\right) + (\rho Cp)_f\left[u\frac{\partial T}{\partial x} + v\frac{\partial T}{\partial y}\right] = \frac{\partial}{\partial x}k\frac{\partial T}{\partial x} + \frac{\partial}{\partial y}k\frac{\partial T}{\partial y} + \frac{d\bar{p}}{dt} \tag{II.72}$$

$$\bar{p} = \rho RT \tag{II.73}$$

Porous region:

$$\frac{\partial \rho}{\partial t} + \frac{\partial \rho u}{\partial x} + \frac{\partial \rho v}{\partial y} = 0 \tag{II.74}$$

$$\rho\left(\frac{1}{\varepsilon}\frac{\partial u}{\partial t} + \frac{1}{\varepsilon^2}u\frac{\partial u}{\partial x} + \frac{1}{\varepsilon^2}v\frac{\partial u}{\partial y}\right) = -\frac{\partial \acute{p}}{\partial x} + \frac{1}{\varepsilon}\frac{\partial}{\partial x}\left(\mu\frac{\partial u}{\partial x}\right) + \frac{1}{\varepsilon}\frac{\partial}{\partial y}\left(\mu\frac{\partial u}{\partial y}\right) + \frac{1}{3}\frac{1}{\varepsilon}\left(\mu\frac{\partial^2 u}{\partial x^2} + \mu\frac{\partial^2 u}{\partial y^2}\right) - Dx \tag{II.75}$$

$$\rho\left(\frac{1}{\varepsilon}\frac{\partial v}{\partial t}+\frac{1}{\varepsilon^2}u\frac{\partial v}{\partial x}+\frac{1}{\varepsilon^2}v\frac{\partial v}{\partial y}\right) = -\frac{\partial \acute{p}}{\partial y}+\frac{1}{\varepsilon}\frac{\partial}{\partial x}\left(\mu\frac{\partial v}{\partial x}\right)+\frac{1}{\varepsilon}\frac{\partial}{\partial y}\left(\mu\frac{\partial v}{\partial y}\right)+\frac{1}{3}\frac{1}{\varepsilon}\left(\mu\frac{\partial^2 v}{\partial x^2}+\mu\frac{\partial^2 v}{\partial y^2}\right)-Dy - g(\rho-\rho_0) \quad \text{(II.76)}$$

$$(\rho Cp)_{eff}\left(\frac{\partial T}{\partial t}\right)+(\rho Cp)_f\left[u\frac{\partial T}{\partial x}+v\frac{\partial T}{\partial y}\right]=\frac{\partial}{\partial x}k\frac{\partial T}{\partial x}+\frac{\partial}{\partial y}k\frac{\partial T}{\partial y}+\frac{d\bar{p}}{dt} \quad \text{(II.77)}$$

$$\bar{p}=\rho RT \quad \text{(II.78)}$$

With:

$$Dx=\mu_0\frac{u}{K}+\frac{1.75}{\sqrt{150}}\frac{\rho}{\sqrt{K}}\frac{\vec{u}}{\varepsilon^{3}/_{2}}u \quad \text{(II.79)}$$

$$Dy=\mu_0\frac{v}{K}+\frac{1.75}{\sqrt{150}}\frac{\rho}{\sqrt{K}}\frac{\vec{v}}{\varepsilon^{3}/_{2}}v \quad \text{(II.80)}$$

Based on the above description, and with the following variable changes:

$$\tau=\frac{t}{\frac{H^2}{\alpha_{eff}}} \qquad X=\frac{x}{H} \qquad Y=\frac{y}{H} \qquad U=\frac{uH}{\alpha_{eff}}$$

$$\pi=\frac{\varepsilon^2 pH^2}{\rho\alpha_{eff}^2} \qquad \theta=\frac{T-T_0}{\Delta T} \qquad \Delta T=T_H-T_C,\ T_0=\frac{(T_H+T_C)}{2} \qquad V=\frac{vH}{\alpha_{eff}}$$

$$\varepsilon_b=\frac{\Delta T}{2T_0} \qquad \bar{P}=\frac{\bar{p}}{p_0}$$

Based on the assumption of mass, momentum, and energy conservation, the following equations describe the unsteady two-dimensional flow with natural convection in a porous cavity [13]:

Fluid region:

$$\frac{\partial \rho^*}{\partial \tau}+\frac{\partial \rho^* U}{\partial X}+\frac{\partial \rho^* V}{\partial V}=0 \quad \text{(II.81)}$$

$$\rho^*\left(\frac{\partial U}{\partial \tau}+U\frac{\partial U}{\partial X}+v\frac{\partial U}{\partial Y}\right) = -\frac{\partial \pi}{\partial X}+Pr\left[\frac{\partial}{\partial X}\left(\mu^*\frac{\partial U}{\partial X}\right)+\frac{\partial}{\partial Y}\left(\mu^*\frac{\partial U}{\partial Y}\right)\right]+\frac{1}{3}\left(\mu^*\frac{\partial^2 U}{\partial X^2}+\mu^*\frac{\partial^2 U}{\partial Y^2}\right) \quad \text{(II.82)}$$

$$\rho^*\left(\frac{\partial V}{\partial \tau}+U\frac{\partial V}{\partial X}+v\frac{\partial V}{\partial Y}\right) = -\frac{\partial \pi}{\partial Y}+Pr\left[\frac{\partial}{\partial X}\left(\mu^*\frac{\partial V}{\partial X}\right)+\frac{\partial}{\partial Y}\left(\mu^*\frac{\partial V}{\partial Y}\right)\right]+\frac{1}{3}\left(\mu^*\frac{\partial^2 V}{\partial X^2}+\mu^*\frac{\partial^2 V}{\partial Y^2}\right) - RaPr\frac{\rho^*-1}{2\epsilon_b} \tag{II.83}$$

$$\rho^* Cp\left(\frac{\partial \theta}{\partial \tau}\right)+\left(U\frac{\partial \theta}{\partial X}+V\frac{\partial \theta}{\partial Y}\right) = \frac{\partial}{\partial X}k^*\frac{\partial \theta}{\partial X}+\frac{\partial}{\partial Y}k\frac{\partial \theta}{\partial Y}+\frac{\gamma-1}{2\varepsilon_b\gamma}\frac{d\bar{p}}{d\tau} \tag{II.84}$$

$$\rho^* = \frac{\bar{P}}{(2\varepsilon_b\theta+1)} \tag{II.85}$$

Porous region:

$$\frac{\partial \rho^*}{\partial \tau}+\frac{\partial \rho^* U}{\partial X}+\frac{\partial \rho^* V}{\partial V}=0 \tag{II.86}$$

$$\rho^*\left(\varepsilon\frac{\partial U}{\partial \tau}+U\frac{\partial U}{\partial X}+v\frac{\partial U}{\partial Y}\right) = -\frac{\partial \pi}{\partial X}+\varepsilon Pr\left[\frac{\partial}{\partial X}\left(\mu^*\frac{\partial U}{\partial X}\right)+\frac{\partial}{\partial Y}\left(\mu^*\frac{\partial U}{\partial Y}\right)\right]+\frac{1}{3}\varepsilon\left(\mu^*\frac{\partial^2 U}{\partial X^2} + \mu^*\frac{\partial^2 U}{\partial Y^2}\right)-\varepsilon^2\frac{Pr}{Da}U-\frac{1.75}{\sqrt{150\,Da}}\frac{\left|\vec{U}\right|}{\varepsilon^{3/2}}U \tag{II.87}$$

$$\rho^*\left(\varepsilon\frac{\partial V}{\partial \tau}+U\frac{\partial V}{\partial X}+v\frac{\partial V}{\partial Y}\right) = -\frac{\partial \pi}{\partial Y}+\varepsilon Pr\left[\frac{\partial}{\partial X}\left(\mu^*\frac{\partial V}{\partial X}\right)+\frac{\partial}{\partial Y}\left(\mu^*\frac{\partial V}{\partial Y}\right)\right]+\frac{1}{3}\varepsilon\left(\mu^*\frac{\partial^2 V}{\partial X^2}+\mu^*\frac{\partial^2 V}{\partial Y^2}\right) - \varepsilon^2 RaPr\frac{\rho^*-1}{2\epsilon_b}-\varepsilon^2\frac{Pr}{Da}V-\frac{1.75}{\sqrt{150\,Da}}\frac{\left|\vec{V}\right|}{\varepsilon^{3/2}}V \tag{II.88}$$

$$\sigma\left(\frac{\partial \theta}{\partial \tau}\right)+\left(U\frac{\partial \theta}{\partial X}+V\frac{\partial \theta}{\partial Y}\right) = \frac{\partial}{\partial X}k^*\frac{\partial \theta}{\partial X}+\frac{\partial}{\partial Y}k\frac{\partial \theta}{\partial Y}+\frac{\gamma-1}{2\varepsilon_b\gamma}\frac{d\bar{p}}{d\tau} \tag{II.89}$$

$$\rho^* = \frac{\bar{P}}{(2\varepsilon_b\theta+1)} \tag{II.90}$$

With [14]:

$$\sigma = \frac{\varepsilon(\rho Cp)_f + (1-\varepsilon)(\rho Cp)_s}{(\rho Cp)_f}$$

$$\sigma = \frac{(\rho Cp)_{eff}}{(\rho Cp)_f} \quad \text{(II.91)}$$

II.3.1 Dilatable Flow (Boussinesq Approximation)

The fluid completely saturates the porous medium, which is assumed to be macroscopically isotropic, homogeneous, and in local thermal equilibrium. The thermophysical properties of the porous medium are considered constant. Furthermore, the temperature differences within the flow domain are assumed to be small, justifying the use of the Boussinesq approximation.

$$\rho(T) = \rho_0[1 - \beta(T - T_0)] \quad \text{(II.92)}$$

Where: $\beta = -\frac{1}{\rho_0}(\frac{\partial \rho}{\partial T})_P$

Also, the Darcy-Brinkman-Forchheimer model is used in the momentum equation [20].

The conservation equations of mass, momentum and energy can be expressed as follows:

Fluid Region

$$\frac{\partial u}{\partial x} + \frac{\partial v}{\partial y} = 0 \quad \text{(II.93)}$$

$$\rho\left(\frac{\partial u}{\partial t} + u\frac{\partial u}{\partial x} + v\frac{\partial u}{\partial y}\right) = -\frac{\partial p}{\partial x} + \mu(\frac{\partial^2 u}{\partial x^2} + \frac{\partial^2 u}{\partial y^2}) \quad \text{(II.94)}$$

$$\rho\left(\frac{\partial v}{\partial t} + u\frac{\partial v}{\partial x} + v\frac{\partial v}{\partial y}\right) = -\frac{\partial p}{\partial y} + \mu(\frac{\partial^2 v}{\partial x^2} + \frac{\partial^2 v}{\partial y^2}) - \rho_{ref} g \quad \text{(II.95)}$$

$$\rho C_P \frac{\partial T}{\partial t} + \rho C_P\left(u\frac{\partial T}{\partial x} + v\frac{\partial T}{\partial y}\right) = k\left(\frac{\partial^2 T}{\partial x^2} + \frac{\partial^2 T}{\partial y^2}\right) \quad \text{(II.96)}$$

With: $\rho_{ref} = \rho - \rho_0 = -\rho_0\beta(T - T_0)$

Porous region

$$\frac{\partial u}{\partial x} + \frac{\partial v}{\partial y} = 0 \quad \text{(II.97)}$$

$$\frac{1}{\varepsilon}\frac{\partial u}{\partial t} + \frac{1}{\varepsilon^2}u\frac{\partial u}{\partial x} + \frac{1}{\varepsilon^2}v\frac{\partial u}{\partial y} = -\frac{1}{\rho}\frac{\partial p}{\partial x} + \frac{\mu_{eff}}{\rho\varepsilon}\nabla^2 u - D_x \quad \text{(II.98)}$$

$$\frac{1}{\varepsilon}\frac{\partial v}{\partial t} + \frac{1}{\varepsilon^2}u\frac{\partial v}{\partial x} + \frac{1}{\varepsilon^2}v\frac{\partial v}{\partial y} = -\frac{1}{\rho}\frac{\partial p}{\partial y} + \frac{\mu_{eff}}{\rho\varepsilon}\nabla^2 v + \beta(T - T_0)g - D_y \quad \text{(II.99)}$$

$$(\rho C_p)_{eff}\frac{\partial T}{\partial t} + (\rho C_p)_f\left(u\frac{\partial T}{\partial x} + v\frac{\partial T}{\partial y}\right) = k_{eff}\left(\frac{\partial^2 T}{\partial x^2} + \frac{\partial^2 T}{\partial y^2}\right) \quad \text{(II.100)}$$

$$(\rho C_p)_{eff} = \varepsilon.(\rho C_p)_f + (1-\varepsilon)(\rho C_p)_s \quad \text{(II.101)}$$

Where D_x and D_y, represent the matrix drags per unit volume of the porous medium in x and y direction respectively.$|\vec{V}|$ is the magnitude of the velocity vector given by:

$$\left|\vec{V}\right| = \sqrt{u^2 + v^2} \tag{II.102}$$

The solid matrix drag per unit volume can be expressed in the following form:

$$D = AV + BV^2 \tag{II.103}$$

For a one-dimensional flow with velocity V, the above form of drag expression is supported by a number of packed bed and fluidized bed correlations, including the widely used Ergun's (1952) correlation.

It can be shown that the contribution of the solid matrix drag for a two-dimensional flow takes the following form:

$$D_x = Au + B(u^2 + v^2)^{\frac{1}{2}}u \tag{II.104}$$

$$D_y = Av + B(u^2 + v^2)^{1/2}v \tag{II.105}$$

The constants A and B involved in the Ergun's correlation are given by:

$$A = 150\frac{(1-\varepsilon)^2}{\varepsilon^3}\frac{\mu_f}{D_p^2} \tag{II.106}$$

$$B = 1.75\frac{(1-\varepsilon)}{\varepsilon^3}\frac{\rho_f}{D_p} \tag{II.107}$$

Where D_p is the effective diameter of particles.

By introducing the permeability K of the medium:

$$K = \frac{\varepsilon^3 D_p^2}{150(1-\varepsilon)^2} \tag{II.108}$$

The solid matrix drag components D_x, D_y, become:

$$D_x = \frac{\mu_f}{K}u + \frac{1.75}{\sqrt{150}}\frac{\rho_f}{\sqrt{K}}\frac{|\vec{V}|}{\varepsilon^{3/2}}u \tag{II.109}$$

$$D_y = \frac{\mu_f}{K}v + \frac{1.75}{\sqrt{150}}\frac{\rho_f}{\sqrt{K}}\frac{|\vec{V}|}{\varepsilon^{3/2}}v \tag{II.110}$$

The effective properties of the porous medium, k_{eff}, $(\rho C_p)_{eff}$ and μ_{eff} generally depend on its porosity and the tortuosity of the solid phase as well as the local fluid velocity. In this work, the interest is not focused on the effects of these parameters, but for simplicity, the corresponding fluid properties are used throughout the study. The momentum equations in the porous region thus become:

$$\frac{1}{\varepsilon}\frac{\partial u}{\partial t} + \frac{1}{\varepsilon^2}u\frac{\partial u}{\partial x} + \frac{1}{\varepsilon^2}v\frac{\partial u}{\partial y} = -\frac{1}{\rho}\frac{\partial p}{\partial x} + \frac{\mu}{\rho\varepsilon}\nabla^2 u - \frac{\mu}{\rho K}u - \frac{1.75}{\sqrt{150}}\frac{1}{\sqrt{K}}\frac{|\vec{V}|}{\varepsilon^{3/2}}u \tag{II.111}$$

$$\frac{1}{\varepsilon}\frac{\partial v}{\partial t} + \frac{1}{\varepsilon^2}u\frac{\partial v}{\partial x} + \frac{1}{\varepsilon^2}v\frac{\partial v}{\partial y} = -\frac{1}{\rho}\frac{\partial p}{\partial y} + \frac{\mu}{\rho\varepsilon}\nabla^2 v + \beta(T - T_0)g - \frac{\mu}{\rho K}v - \frac{1.75}{\sqrt{150}}\frac{1}{\sqrt{K}}\frac{|\vec{V}|}{\varepsilon^{3/2}}v \tag{II.112}$$

The governing equations are converted to non-dimensional form using the following non-dimensional variables:

$$\tau = \frac{t}{\frac{H^2}{\alpha}}, X = \frac{x}{H}, Y = \frac{y}{H}, U = \frac{uH}{\alpha}, V = \frac{vH}{\alpha}, P = \frac{\varepsilon^2 pH^2}{\rho\alpha^2}$$

$$\theta = \frac{T-T_0}{\Delta T}, \Delta T = T_H - T_C, T_0 = \frac{T_H + T_C}{2}$$

Considering the previous assumptions, the governing equations for an unsteady 2-D problem can be written in dimensionless form:

Fluid Region

$$\frac{\partial U}{\partial X}+\frac{\partial V}{\partial Y}=0 \tag{II.113}$$

$$\frac{\partial U}{\partial \tau}+U\frac{\partial U}{\partial X}+V\frac{\partial U}{\partial Y}=-\frac{\partial P}{\partial X}+Pr\,\nabla^2 U \tag{II.114}$$

$$\frac{\partial V}{\partial \tau}+U\frac{\partial V}{\partial X}+V\frac{\partial V}{\partial Y}=-\frac{\partial P}{\partial Y}+Pr\,\nabla^2 V+Ra\,Pr\,\theta \tag{II.115}$$

$$\frac{\partial \theta}{\partial \tau}+\left(U\frac{\partial \theta}{\partial X}+V\frac{\partial \theta}{\partial Y}\right)=\left(\frac{\partial^2\theta}{\partial X^2}+\frac{\partial^2\theta}{\partial Y^2}\right) \tag{II.116}$$

Porous region

$$\frac{\partial U}{\partial X}+\frac{\partial V}{\partial Y}=0 \tag{II.117}$$

$$\varepsilon\frac{\partial U}{\partial \tau}+U\frac{\partial U}{\partial X}+V\frac{\partial U}{\partial Y}=-\frac{\partial P}{\partial X}+Pr\,\varepsilon\,\nabla^2 U-\frac{Pr}{Da}\varepsilon^2 U-1.75\sqrt{\frac{\varepsilon}{150Da}}\left|\sqrt{U^2+V^2}\right|U \tag{II.118}$$

$$\varepsilon\frac{\partial V}{\partial \tau}+U\frac{\partial V}{\partial X}+V\frac{\partial V}{\partial Y}=-\frac{\partial P}{\partial Y}+Pr\,\varepsilon\,\nabla^2 V+Ra\,Pr\,\varepsilon^2\,\theta-\frac{Pr}{Da}\varepsilon^2 V-1.75\sqrt{\frac{\varepsilon}{150Da}}\left|\sqrt{U^2+V^2}\right|V \tag{II.119}$$

$$\sigma\frac{\partial \theta}{\partial \tau}+\left(U\frac{\partial \theta}{\partial X}+V\frac{\partial \theta}{\partial Y}\right)=\left(\frac{\partial^2\theta}{\partial X^2}+\frac{\partial^2\theta}{\partial Y^2}\right) \tag{II.120}$$

With: $\sigma=\frac{\varepsilon.(\rho C_p)_f+(1-\varepsilon)(\rho C_p)_s}{(\rho C_P)_f}$

II.4 CONCLUSION

In this chapter, we have made significant progress in creating a mathematical model for compressible flow. By simplifying the equations, we have uncovered the assumptions made for different types of flows, such as low Mach number flow and incompressible flow. It's important to consider the limitations of each equation system, as they affect how applicable they are in real-life situations.

Moving forward, the next chapter will focus on a numerical method called the finite volume method. This method is a powerful tool for solving equations and obtaining numerical solutions. It allows us to simulate and analyze complex flows, considering the complexities of the compressible flow model we established in this chapter.

By combining theoretical understanding with computational techniques, we can gain a deeper knowledge of fluid dynamics and apply it to practical scenarios. The next chapter will provide valuable insights into how we can implement this mathematical model in practice, empowering us to tackle challenging problems and make informed engineering decisions.

References

[1] An Introduction to Fluid Dynamics, (n.d.). https://www.cambridge.org/core/books/an-introduction-to-fluid-dynamics.

[2] P.-L. Lions, P.-L. Lions, Mathematical Topics in Fluid Mechanics: Volume 1: Incompressible Models, Oxford University Press, Oxford, New York, 2013.

[3] S. Paolucci, On the Filtering of Sound from the Navier–Stokes Equations, NASA STIRecon Tech. Rep. N. 83 (1982) 26036.

[4] The Anelastic Approximation for Thermal Convection in: Journal of the Atmospheric Sciences Volume 26 Issue 3 (1969).

[5] J.A. Dutton, G.H. Fichtl, Approximate Equations of Motion for Gases and Liquids., J. Atmospheric Sci. 26 (1969) 241–254. https://doi.org/10.1175/1520-0469(1969)026.

[6] J. Fröhlich, Résolution numérique des équations de Navier-Stokes à faible nombre de Mach par méthode spectrale, These de doctorat, Nice, 1990.

[7] W. Sutherland, LII. The viscosity of gases and molecular force, Lond. Edinb. Dublin Philos. Mag. J. Sci. 36 (1893) 507–531. https://doi.org/10.1080/14786449308620508.

[8] T. Papanastasiou, G. Georgiou, A.N. Alexandrou, Viscous Fluid Flow, CRC Press, 2021.

[9] Theory and Applications of Viscous Fluid Flows - Radyadour Kh. Zeytounian - Google Livres.

[10] F.M. White, Viscous fluid flow, 2nd ed, McGraw-Hill, New York, 1991.

[11] J. Boussinesq, Theorie analytique de la Chaleur, Gauthier-Villars, 1903.

[12] G. Chmaycem, Étude des équations des milieux poreux et des modèles de cloques, phd thesis, Université Paris-Est, 2014.

[13] V. Lemarie, Quelques problèmes de limites singulières en mécanique des fluides compressibles, These en préparation, Université Gustave Eiffel, 2022.

[14] H. Liamena, Simulation numerique de la convection naturelle laminaire dans une cavité poreuse.

III.1. INTRODUCTION

The equations introduced in the previous chapter are nonlinear, elliptic, coupled partial differential equations. Due to their complexity, analytical solutions are not feasible, and numerical methods are employed for their solution. Various numerical techniques have been developed [1], including finite difference methods [2,3], finite element methods [4–6], finite volume methods [7–11], and spectral methods [12]. Among these methods, the finite volume method is widely used due to its numerous advantages, including:

- Conservation of momentum and energy balances: The difference equations derived from the finite volume method accurately reflect the conservation principles of momentum and energy. This ensures that the conservation principle in discretized form is satisfied for the entire numerical domain.
- Numerical robustness and ease of use: The finite volume method is known for its numerical stability and ease of implementation. It provides a formalism that closely resembles physical reality, specifically the conservation of energy and momentum balances.

In the following sections, we will describe the finite volume method in detail, highlighting its advantages and discussing its application to the solution of the conservation equations.

III.2. GENERAL FORM OF CONSERVATION EQUATIONS

To simplify the presentation, the dimensionless form of the low Mach number conservation equations, as discussed in the previous chapter, can be mathematically translated into scalar function transport equations. These equations take the general form of convection-diffusion equations ϕ:

$$\frac{\partial}{\partial t}(\rho\phi)+\nabla.\left(\rho\vec{V}\phi\right)=\nabla.(\Gamma\nabla\phi)+S_{\phi} \qquad \text{(III.1)}$$

The first term in this equation: the transient term, $\frac{\partial}{\partial t}(\rho\phi)$, represents the accumulation of ϕ in time. The second, $\nabla.\left(\rho\vec{V}\phi\right)$, represents convective transport ϕ. In the second member, the first term, $\nabla.(\Gamma\nabla\phi)$, corresponds to diffusion transport ϕ, and the last, S_{ϕ}, source term, to local production of ϕ. the termes : ϕ,Γ and S_{ϕ} and are explained in detail in Table III.1.

Table III.1: Expressions of ϕ, Γ and S_ϕ for Mach weak equations (Case of fluid region).

Equation	ϕ	Γ	S_ϕ
Continuity	ρ	0	0
Momentum following x	U	$\Pr \mu^*$	$\frac{1}{3}\nabla\mu^*\nabla.\vec{V}\Big\vert_X - \frac{\partial\pi}{\partial X}$
Momentum following y	V	$\Pr \mu^*$	$\frac{1}{3}\nabla\mu^*\nabla.\vec{V}\Big\vert_Y - \frac{\partial\pi}{\partial Y} - RaPr\frac{\rho^*-1}{2\epsilon_b}$
Energy	θ	k^*	$\frac{\gamma-1}{2\varepsilon_b\gamma}\frac{d\overline{P}}{dt}$

Table III.2: Expressions of ϕ, Γ and S_ϕ for Mach weak equations (Case of porous region).

Equation	ϕ	Γ	S_ϕ
Continuity	ρ	0	0
Momentum following x	U	$\varepsilon\, Pr\, \mu^*$	$\varepsilon\frac{1}{3}\nabla\mu^*\nabla.\vec{V}\Big\vert_X - \varepsilon^2\frac{Pr}{Da}U - \frac{1.75}{\sqrt{150\,Da}}\frac{\vert\vec{U}\vert}{\varepsilon^{3}/_{2}}U - \frac{\partial\pi}{\partial X}$
Momentum following y	V	$\varepsilon\, Pr\, \mu^*$	$\varepsilon\frac{1}{3}\nabla\mu^*\nabla.\vec{V}\Big\vert_Y - \varepsilon^2\frac{Pr}{Da}V - \frac{1.75}{\sqrt{150\,Da}}\frac{\vert\vec{V}\vert}{\varepsilon^{3}/_{2}}V - \frac{\partial\pi}{\partial Y} - \varepsilon^2 RaPr\frac{\rho^*-1}{2\epsilon_b}$
Energy	θ	k^*	$\frac{\gamma-1}{2\varepsilon_b\gamma}\frac{d\overline{P}}{dt}$

III.3 THE FINITE VOLUME METHOD

III.3.1 Principle

Conservative formulations of partial differential equations offer the advantage of being able to be reformulated integrally using the divergence theorem. The conservation principle is the fundamental law of the finite volume method. It states that the variation of a property depends on the net flow across the boundary S enveloping the volume Ω. The control volume method is, therefore, a discretization technique for solving equations written in conservative form. Its principle is very simple, initially developed in the case of compressible flows by Godunov [13] and Glimm [14], then spread to the scientific community of mechanics by Patankar & Spalding [15] in the 1970s and discussed in detail by Patankar [16] in 1980. The principle of the finite volume method is to integrate the equation to be solved on each of the control volumes.

As shown in Figure III.1, the domain is discretized using a dimensional grid (uniform or non-uniform) in both directions and oriented positively to the right (East) and upwards (North) respectively. To write the discretization scheme at a point P, we choose a nomenclature adapted to the principle of the finite-volume method for storing variables in our mesh, all with

the aim of making things easier in the subsequent discretization. We therefore consider the element P as shown in Figure III.1, and note that the uppercase indices (E, W, N, S) characterize the variables relating to the centroids adjacent to P, while the lowercase indices (e,w,n,s) refer to the faces of the element.

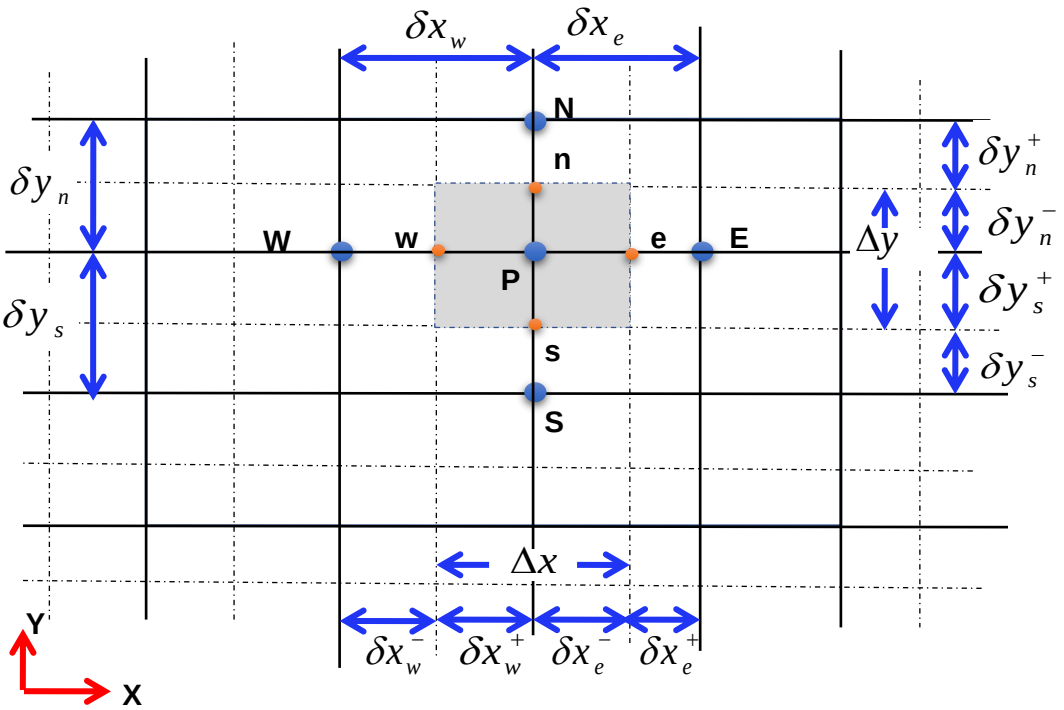

Figure III.1: 2D control volume.

III.3.2 Offset mesh

The discretization of a diffusion transport equation over a control volume using the finite volume method involves the velocity values at the volume interfaces (u_e, u_w, v_n, v_s). It is therefore advantageous to calculate these velocities directly at the interfaces (without having to perform interpolations). On the other hand, discretizing the continuity equation and the pressure gradient using linear interpolation can induce significant errors due to the "checkerboard, jagged, zig-zag" pressure or velocity distribution (an oscillating pressure field in a collocative mesh, (Figure III.2a) [17] is seen as a uniform field). To circumvent these difficulties, we prefer to use staggered grids (Figure III.2b). However, recent methods have been proposed on collocative meshes by Rhie & Chow [18], which eliminate the problem of harmful oscillations by means of appropriate interpolation [19].

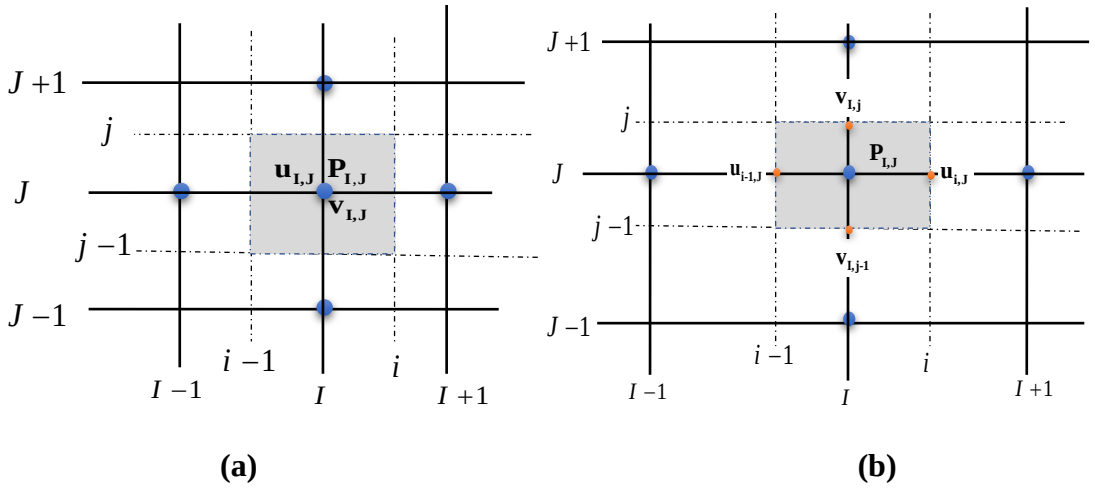

Figure III.2: Velocity-pressure formulation mesh: (a) collocative mesh; (b) offset mesh.

The main mesh (Figure III.1) is decomposed into three secondary meshes. A main mesh is constructed to compute the pressure, temperature, density (P, ϕ, ρ), and the conservation of mass equation (at the center of each control volume). Two shifted meshes, one to the right and one upwards, are used to compute the velocities (u, v) in the two directions (on the faces of the control volume). This means that not all unknowns of the problem are computed on the same computational mesh. Different meshes, control volumes, and storage points can be used for different variables. The relative arrangement of the different variables is schematically represented in Figure III.3.

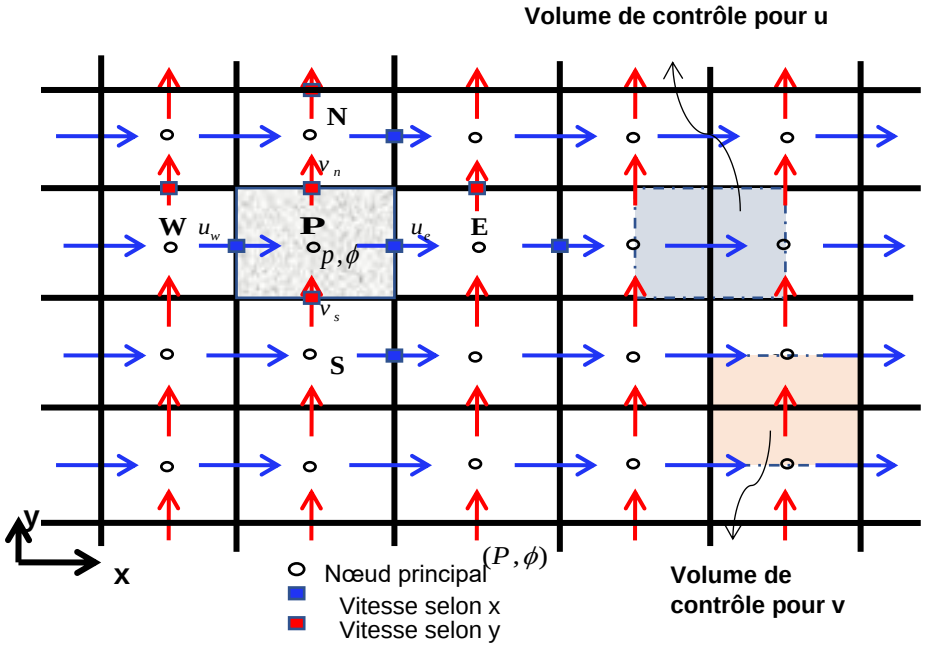

Figure III.3: Control volumes for scalars and velocities.

The MAC (Marker And Cell) approach, which is used for numerical modeling of free-surface flow, has shown to be particularly well-suited for the offset mesh, which Harlow and Welch first presented in 1965 [17]. Due to the clustering of discrete velocities around pressure nodes, which creates a very compact structure, this mesh arrangement has a number of benefits. It thus permits concise approximations with reasonably close spots. Additionally, the spatial convergence properties of the staggered mesh make it a superb option for precise simulations [16].

III.4 DISCRETIZATION OF CONSERVATION EQUATIONS

When the general version of the unstable differential equation (III.1) is integrated in time over the control volume Ω_{CV} around the present node *P*, we obtain:

$$\int_t \int_{\Omega_{CV}} \frac{\partial}{\partial t}(\rho\phi) dt d\Omega + \int_t \int_{\Omega_{CV}} div(\rho\phi\vec{u}) dt d\Omega -$$

$$\int_t \int_{\Omega_{CV}} div(\Gamma grad\,\phi) dt d\Omega = \int_t \int_{\Omega_{CV}} S_\phi dt d\Omega \qquad \text{(III.2)}$$

Using Gauss's divergence theorem, we obtain:

$$\int_t \int_{\Omega_{CV}} \frac{\partial}{\partial t}(\rho\phi) dt d\Omega + \int_t \int_{A_{CV}} (\rho\phi\vec{u}) d\vec{A} dt - \int_t \int_{A_{CV}} (\Gamma grad\,\phi) d\vec{A} dt = \int_t \int_{\Omega_{CV}} S_\phi dt d\Omega \qquad \text{(III.3)}$$

Where *A* is the surface bounding the control volume Ω_{CV} .

III.4.1 Transitional term

To integrate this particular term, we consider only the variation in time, assimilating the variable ϕ to its value at the center of the control volume:

$$I_1 = \int_t \int_{\Omega_{CV}} \frac{\partial}{\partial t} \rho\phi d\Omega dt = \left\{(\rho\phi)_P - (\rho\phi)_P^0\right\} \Delta\Omega \qquad \text{(III.4)}$$

Where Ω designates the control volume of ϕ and $\Delta\Omega$ its measurement ($\Delta\Omega = \Delta x\,\Delta y$) in the 2D case, and the exponent *0* indicates that the quantity is considered at the previous time step.

III.4.2 Convective term

$$I_2 = \int_t \int_{A_{CV}} (\rho\phi\vec{u}) d\vec{A}_n dt = \int_t \int_{A_{CV}} (\rho\phi\vec{u})(d\vec{A}_e - d\vec{A}_w + d\vec{A}_s - d\vec{A}_n) dt$$

$$= \left\{(\rho\phi uA)_e - (\rho\phi uA)_w + (\rho\phi vA)_n - (\rho\phi vA)_s\right\} \Delta t \qquad \text{(III.5)}$$

We define the variable $F_i = (\rho v A)_i$, which represents the convective mass flow through the surface *(i)*, $i = (e, w, n, s)$.

Table III.3: Convective coefficient expression.

Face	E	W	n	s
Convective mass flux	$F_e = \rho_e u_e A_e$	$F_w = \rho_w u_w A_w$	$F_n = \rho_n v_n A_n$	$F_s = \rho_s v_s A_s$

It comes that:

$$I_2 = \{F_e \phi_e - F_w \phi_w + F_n \phi_n - F_s \phi_s\} \Delta t \qquad \text{(III.6)}$$

III.4.3 Diffusive term

Finally, the gradient of ϕ at the interfaces is determined by assuming that varies linearly between each mesh point (Figure III.4). The conclusion is as follows:

$$I_3 = \int_t \int_{A_{CV}} (\Gamma grad\, \phi) d\vec{A} dt = \left\{ (\Gamma \frac{\partial \phi}{\partial x} A)_e - (\Gamma \frac{\partial \phi}{\partial x} A)_w + (\Gamma \frac{\partial \phi}{\partial y} A)_n - (\Gamma \frac{\partial \phi}{\partial x} A)_s \right\} \Delta t \qquad \text{(III.7)}$$

$$I_3 = \left((\Gamma \frac{\phi_E - \phi_P}{(\delta x)_e} A)_e - (\Gamma \frac{\phi_P - \phi_W}{(\delta x)_w} A)_w + (\Gamma \frac{\phi_N - \phi_P}{(\delta y)_n} A)_n - (\Gamma \frac{\phi_P - \phi_S}{(\delta y)_s} A)_s \right) \Delta t \qquad \text{(III.8)}$$

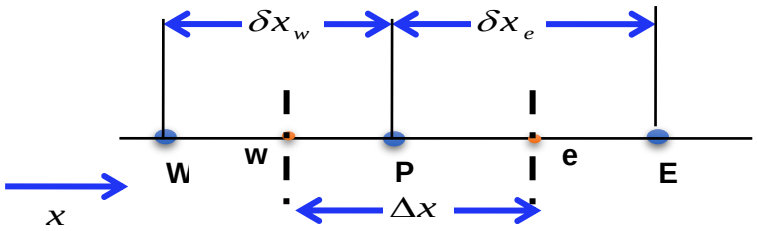

Figure III.4: Interpolation for the gradient ϕ

The diffusive coefficient is given by $D_i = \frac{\Gamma_i A_i}{\delta x_i}$, where $i = (e, w, n, s)$

Table III.4 : Diffusion coefficient expressions.

Face	E	w	n	s
Diffusion conductance	$D_e = \frac{\Gamma_e A_e}{\delta x_e}$	$D_w = \frac{\Gamma_w A_w}{\delta x_w}$	$D_n = \frac{\Gamma_n A_n}{\delta y_n}$	$D_s = \frac{\Gamma_s A_s}{\delta y_s}$

The final result is:

$$I_3 = \left(D_e (\phi_E - \phi_P) - D_w (\phi_P - \phi_W) + D_n (\phi_N - \phi_P) - D_s (\phi_P - \phi_S) \right) \Delta t \qquad \text{(III.9)}$$

Calculating conductance Γ :

In general $\Gamma_e \neq \Gamma_w$, thermal conductivity is a function of temperature $\Gamma = \Gamma(T)$ or even a function of space $\Gamma = \Gamma(x)$ for composite materials. If we consider the flux at the interface "*e*" (Figure III.5), it can be expressed as:

$$q_e = \frac{T_P - T_E}{\frac{\delta x_e^-}{\Gamma_P} + \frac{\delta x_e^+}{\Gamma_E}} = \frac{T_P - T_E}{\frac{\delta x_e}{\Gamma_e}} \qquad \text{(III.10)}$$

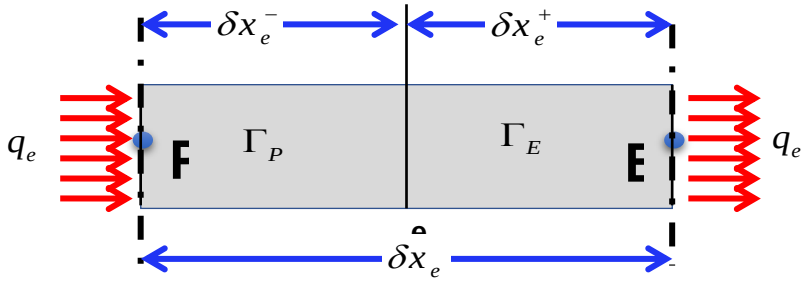

Figure III.5: Diffusivity for a composite material.

From equation (III.10), we derive the expression for thermal conductivity at the control volume interface:

$$\Gamma_e = \frac{\delta x_e}{\frac{\delta x_e^-}{\Gamma_P} + \frac{\delta x_e^+}{\Gamma_E}} = \delta x_e \frac{\Gamma_P \Gamma_E}{\Gamma_P \delta x_e^+ + \Gamma_E \delta x_e^-} \qquad \text{(III.11)}$$

If we define the parameters: $f_e = \frac{\delta x_e^+}{\delta x_e}$ and $1 - f_e = \frac{\delta x_e^-}{\delta x_e}$, equation (III.11) becomes:

$$\Gamma_e = \frac{1}{\frac{1-f_e}{\Gamma_P} + \frac{f_e}{\Gamma_E}} = \frac{\Gamma_P \Gamma_E}{f_e \Gamma_P + (1-f_e)\Gamma_E} \qquad \text{(III.12)}$$

III.4.4 Source term

Given by:

$$I_4 = \int_t \int_{\Omega_{CV}} S_\phi d\Omega = \overline{S} \Delta t \Delta\Omega \qquad \text{(III.13)}$$

Where $\overline{S}$ is the average value of *S* over the considered volume.

III.4.4.1 Linearization of the source term

The source term S_ϕ often depends on the variable ϕ . It can be expressed as a linear function of ϕ_p . Pantakar's method [16] is recommended for linearizing the source term. It involves writing:

$$\overline{S} = S_C + S_P \phi_p \tag{III.14}$$

Where S_C represents the constant part of $\overline{S}$ (which does not depend on ϕ_P), while S_P is the coefficient of ϕ_P (S_P does not represent $\overline{S}$ evaluated at *P*).

Using the expressions for I_1, I_2, I_3 and I_4 , equation (3.3) can be written in discretized form as:

$$\left\{(\rho\phi)_P - (\rho\phi)_P^0\right\}\Delta\Omega + \left\{F_e\phi_e - F_w\phi_w + F_n\phi_n - F_s\phi_s\right\}\Delta t -$$
$$\left(D_e(\phi_E - \phi_P) - D_w(\phi_P - \phi_W) + D_n(\phi_N - \phi_P) - D_s(\phi_P - \phi_S)\right)\Delta t = \left(S_C + S_P\phi_p\right)\Delta t\,\Delta\Omega \tag{III.15}$$

III.4.5 Continuity equation

In the case of Navier-Stokes equations, we also need to solve the continuity equation:

$$\frac{\partial\rho}{\partial t} + \frac{\partial}{\partial x}(\rho u) + \frac{\partial}{\partial y}(\rho v) = 0 \tag{III.16}$$

Integration of this equation over the control volume Ω_{CV} leads to:

$$\int_t \left(\int_{\Omega_{CV}} \rho d\Omega\right)dt + \int_{dt}\left(\int_{\Omega_{CV}} \frac{\partial}{\partial x}(\rho u)d\Omega\right)dt + \int_t\left(\int_{\Omega_{CV}} \frac{\partial}{\partial y}(\rho v)d\Omega\right)dt = 0 \tag{III.17}$$

$$(\rho_P - \rho_P^0)\frac{\Delta\Omega}{\Delta t} + (\rho u A)_e - (\rho u A)_w + (\rho v A)_n - (\rho v A)_s = 0 \tag{III.18}$$

This gives:

$$(\rho_P - \rho_P^0)\frac{\Delta\Omega}{\Delta t} = F_w - F_e + F_s - F_n \tag{III.19}$$

Performing the operation $[(\text{III.}15) - (\phi_P \times (\text{III.}19))]$, we obtain:

$$\left\{\rho_P^0 \frac{\Delta\Omega}{\Delta t} + F_w - F_e + F_s - F_n - S_P \Delta\Omega\right\}\phi_P + \{F_e\phi_e - F_w\phi_w + F_n\phi_n - F_s\phi_s\} -$$

$$\left(D_e\phi_E - D_e\phi_P - D_w\phi_P + D_w\phi_W + D_n\phi_N - D_n\phi_P - D_s\phi_P + D_s\phi_S\right) = S_C\Delta\Omega + \rho_P^0\phi_P^0\frac{\Delta\Omega}{\Delta t} \qquad \text{(III.20)}$$

III.4.6 Numerical schemes

In equation (III.20), the unknown variable ϕ is not yet expressed on its domain of definition (in convective terms), which are the discretization nodes. The interpolation that accomplishes this depends on the choice of spatial discretization scheme. Several schemes are available, such as CDS, upwind, exponential, hybrid, and power, which provide the value of the variable ϕ on its domain.

Assuming that $Pe = \frac{F}{D}$ represents the mesh Péclet number, the conservation equation, once implicitly discretized in time, takes the form:

$$a_P^{n+1}\phi_P^{n+1} = a_E^{n+1}\phi_E^{n+1} + a_W^{n+1}\phi_W^{n+1} + a_N^{n+1}\phi_N^{n+1} + a_S^{n+1}\phi_S^{n+1} + b \qquad \text{(III.21)}$$

The coefficients of equation (3.41) are expressed in the following general forms:

$$a_E = D_e A\left(|P_e|\right) + \ -F_e, 0 \qquad \text{(III.22)}$$

$$a_W = D_w A\left(|P_w|\right) + \ F_w, 0 \qquad \text{(III.23)}$$

$$a_N = D_n A\left(|P_n|\right) + \ -F_n, 0 \qquad \text{(III.24)}$$

$$a_S = D_s A\left(|P_s|\right) + \ F_s, 0 \qquad \text{(III.25)}$$

$$a_P = a_E + a_W + a_N + a_S + a_P^0 - S_P \qquad \text{(III.26)}$$

$$a_P^0 = \rho_P^0 \frac{\Delta\Omega}{\Delta t} \qquad \text{(III.27)}$$

$$b = S_C\Delta\Omega + a_P^0\phi_P^0 \qquad \text{(III.28)}$$

The expression in square brackets represents the maximum between the quantities and $A(|P|)$ serves as a characteristic function of the chosen scheme (Table III.4) [20].

Table III.5: Expression of the function $A(|P|)$ for different schemes.

Schéma	$A(\|P\|)$
CDS	$1-0.5\|P\|$
Upwind	**1**
Exponentiel	$\|P\|/(\exp(\|P\|)-1)$
Hybride	$[0,1-0.5\|P\|]$
Power Law	$[0,(1-0.1\|P\|)^5]$

The exponential scheme discretizes all convective and diffusive terms, unlike conventional schemes such as off-center and upstream. This discretization involves the expression of the *J* coefficients on the faces of the control volumes. These coefficients are interpolated between the two nodes separating the faces in such a way that the stationary 1D convection-diffusion equation is satisfied between these two points, regardless of the problem being solved.

The hybrid scheme [21] and power scheme [20] used in this study are derived directly from the exponential scheme. Both schemes are based on the approximation of coefficients where the exponential term appears, which can be computationally expensive. Depending on the Peclet number, the hybrid scheme performs a piecewise linear approximation of the function *A (P),* and the power scheme performs a polynomial approximation.

III.4.7 Discretization of the momentum equation

The approach to obtaining the values of the velocities u and v is to solve the Navier-Stokes equations similar to the general transport equation (III.1), replacing each of these variables with the corresponding shifted meshes to calculate the coefficients a_{nb} (a_P, a_E, a_W, a_N, a_S). The parameters are calculated so that a translation (shift) is made for the main mesh by one value $\delta x = \Delta x/2$ in the direction x to obtain u and by one value $\delta y = \Delta y/2$ in the direction y to obtain v .

Scalar quantities such as pressure, temperature, etc., will be denoted with the index (I, J), while vector components will be calculated on a grid shifted by half a mesh in the direction of the corresponding component (Figure III.6).

In this case, the pressure gradient at a node of the offset mesh is integrated by considering the pressure difference between the two neighboring points of the main mesh.

Figure III.6 shows the continuous lines of the mesh numbered using capital letters. In the x direction, the numbering is ...., I-1, I, I+1, ... etc., where scalar variables (temperature, pressure, density, etc.) are calculated. In the y direction, the numbering is ...., J-1, J, J+1, ... etc. The discontinuous lines that construct the scalar cell faces are denoted by lowercase letters: ..., i-1, i, i+1, ... and ..., j-1, j, j+1, ... in the x and y directions, respectively.

Thus, the nodes of scalar variables ($T, P, \rho.....$) are defined by the intersection of continuous lines indicated by capital letters. For example, point *P* in Figure III.6 is identified by the index (I, J). Velocity components (u, v) are stored at the centers of mesh faces (scalar cell), faces (e, w) of the scalar cell for the u component, and faces (n, s) for the v component. Their corresponding nodes are located at the intersection of a continuous line with a broken line, and are therefore defined by a combination of lowercase and uppercase letters. The u component of velocity is defined by the index (i, J), and the v component is defined by the index (I, j) (Figures III.7, III.8)

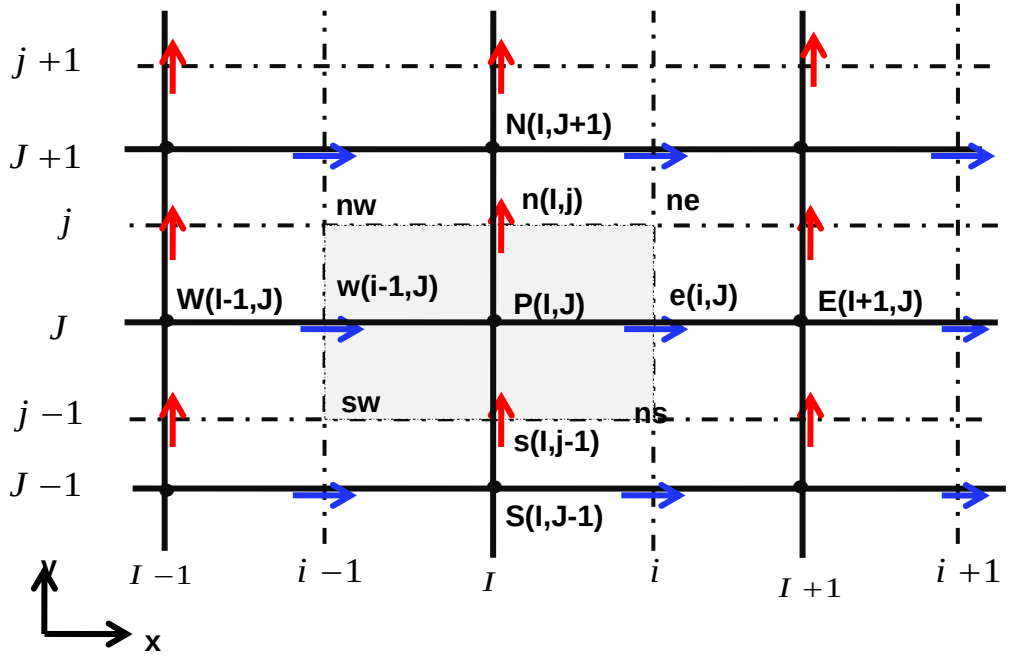

Figure III.6: Control volume for scalar quantities (P, ϕ) and continuity equation.

The offset between the pressure grid and the velocity grids allows for the calculation of velocity field divergence directly at the pressure nodes, avoiding pressure oscillations observed when using collocated grids.

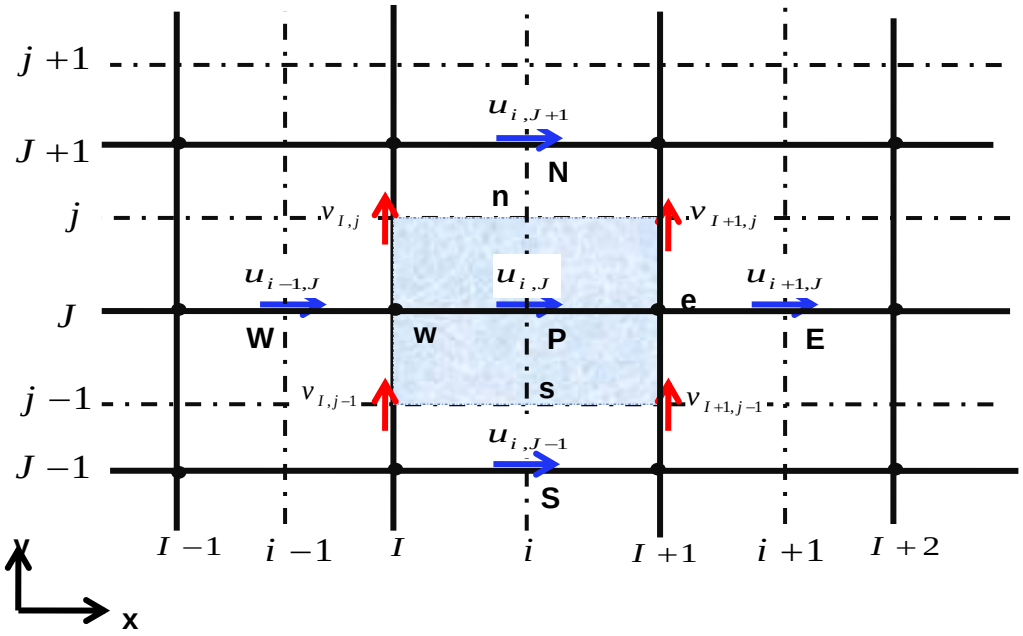

Figure III.7: Control volume for the u component and its adjacent components.

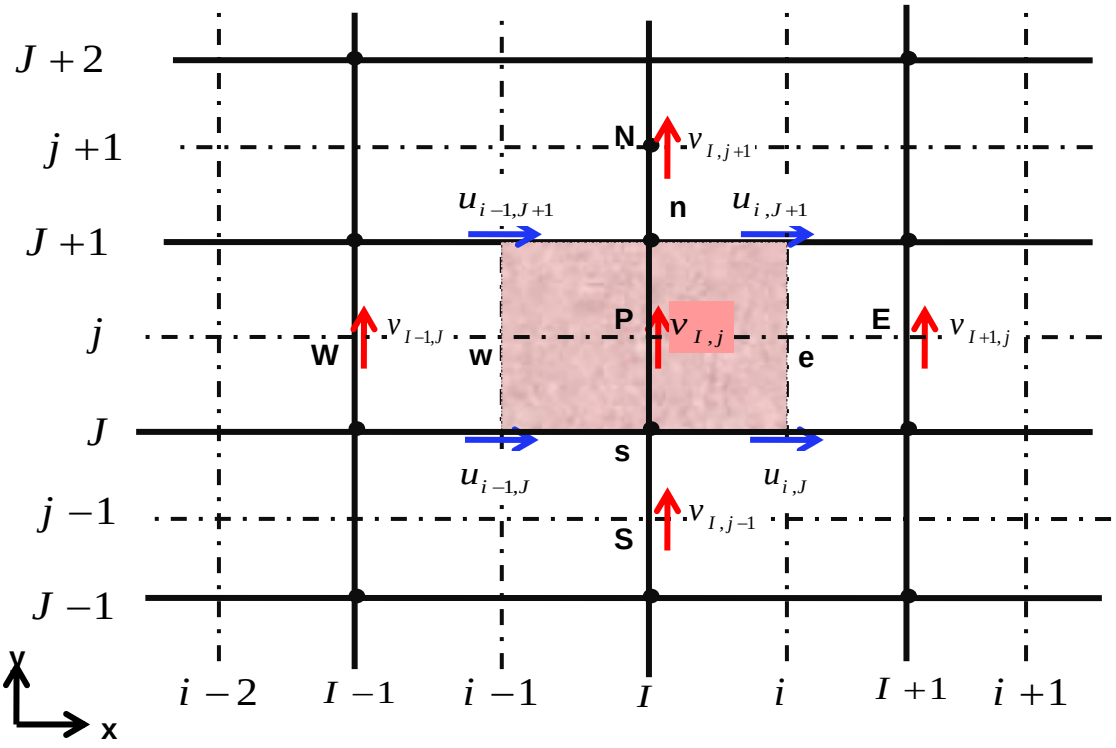

Figure III.8: Control volume for the v component and its adjacent components.

Expressed in the new coordinate system, the momentum equation in the x direction discretized at point (i, J) is given by:

$$a_{i,J}u_{i,J} = \sum a_{nb}u_{nb} - \frac{P_{I,J} - P_{I-1,J}}{\delta x_u}\Delta V_u + \overline{S}\Delta V_u \qquad \text{(III.29)}$$

Where:

$$a_{i,J}u_{i,J} = \sum a_{nb}u_{nb} + \left(P_{I-1,J} - P_{I,J}\right)A_{i,J} + b_{i,J} \qquad \text{(III.30)}$$

Where ΔV_u is the volume of the control volume of *u*, $b_{ij} = \overline{S}\Delta V_u$ is the source term of the momentum equation along x and $A_{i,J}$ is the area of the face (e or w) of the control volume of u.

In the new numbering system, the neighboring nodes E, W, N and S of the sum $\left(\sum a_{nb}u_{nb}\right)$ are given by the indices (i-1,J), (i+1,J), (i,J+1) and (i,J-1) (see Figure III.7).

The values of the coefficients $a_{i,J}$ and a_{nb} can be calculated with one of the previously presented numerical scheme differentiation methods (Upwind, Hybrid, Power....) adapted for convection-diffusion problems. The coefficients contain combinations of convective flux per unit mass F and diffusion conductance D at the faces of the *u*-velocity control volumes. Application of the new notation system (offset mesh) gives us the values of *F* and *D* for each of the faces e, w, n and s of the control volume for u.

$$F_w = (\rho u)_w = \frac{F_{i,J} + F_{i-1,J}}{2} = \frac{1}{2}\left[\left(\frac{\rho_{I,J} + \rho_{I-1,J}}{2}\right)u_{i,J} + \left(\frac{\rho_{I-1,J} + \rho_{I-2,J}}{2}\right)u_{i-1,J}\right] \qquad \text{(III.31)}$$

$$F_e = (\rho u)_e = \frac{F_{i+1,J} + F_{i,J}}{2} = \frac{1}{2}\left[\left(\frac{\rho_{I+1,J} + \rho_{I,J}}{2}\right)u_{i+1,J} + \left(\frac{\rho_{I,J} + \rho_{I-1,J}}{2}\right)u_{i,J}\right] \qquad \text{(III.32)}$$

$$F_s = (\rho v)_s = \frac{F_{I,j} + F_{I-1,j}}{2} = \frac{1}{2}\left[\left(\frac{\rho_{I,J} + \rho_{I,J-1}}{2}\right)v_{I,j} + \left(\frac{\rho_{I-1,J} + \rho_{I-1,J-1}}{2}\right)v_{I-1,j}\right] \qquad \text{(III.33)}$$

$$F_n = (\rho v)_n = \frac{F_{I,j+1} + F_{I-1,j+1}}{2} = \frac{1}{2}\left[\left(\frac{\rho_{I,J+1} + \rho_{I,J}}{2}\right)v_{I,j+1} + \left(\frac{\rho_{I-1,J+1} + \rho_{I-1,J}}{2}\right)v_{I-1,j+1}\right] \qquad \text{(III.34)}$$

$$D_w = \frac{\Gamma_{I-1,J}}{x_i - x_{i-1}} \qquad \text{(III.35)}$$

$$D_e = \frac{\Gamma_{I,J}}{x_{i+1} - x_i} \qquad \text{(III.36)}$$

$$D_s = \frac{\Gamma_{I-1,J} + \Gamma_{I,J} + \Gamma_{I-1,J-1} + \Gamma_{I,J-1}}{4(y_J - y_{J-1})} \qquad \text{(III.37)}$$

$$D_n = \frac{\Gamma_{I-1,J+1} + \Gamma_{I,J+1} + \Gamma_{I-1,J} + \Gamma_{I,J}}{4(y_{J+1} - y_J)} \tag{III.38}$$

The following movement quantity equation is analogously changed to:

$$a_{I,j} v_{I,j} = \sum a_{nb} v_{nb} + \left(P_{I,J-1} - P_{I,J}\right) A_{I,j} + b_{I,j} \tag{III.39}$$

Similarly, the coefficients $a_{I,j}$ and a_{nb} contain combinations of *F* and *D*, their values are obtained by the same calculation procedure as the speed *u* and are given by:

$$F_w = (\rho u)_w = \frac{F_{i,J} + F_{i,J-1}}{2} = \frac{1}{2}\left[\left(\frac{\rho_{I,J} + \rho_{I-1,J}}{2}\right) u_{i,J} + \left(\frac{\rho_{I-1,J-1} + \rho_{I,J-1}}{2}\right) u_{i,J-1}\right] \tag{III.40}$$

$$F_e = (\rho u)_e = \frac{F_{i+1,J} + F_{i+1,J-1}}{2} = \frac{1}{2}\left[\left(\frac{\rho_{I+1,J} + \rho_{I,J}}{2}\right) u_{i+1,J} + \left(\frac{\rho_{I,J-1} + \rho_{I+1,J-1}}{2}\right) u_{i+1,J-1}\right] \tag{III.41}$$

$$F_s = (\rho v)_s = \frac{F_{I,j-1} + F_{I,j}}{2} = \frac{1}{2}\left[\left(\frac{\rho_{I,J-1} + \rho_{I,J-2}}{2}\right) v_{I,j-1} + \left(\frac{\rho_{I,J} + \rho_{I,J-1}}{2}\right) v_{I,j}\right] \tag{III.42}$$

$$F_n = (\rho v)_n = \frac{F_{I,j} + F_{I,j+1}}{2} = \frac{1}{2}\left[\left(\frac{\rho_{I,J} + \rho_{I,J-1}}{2}\right) v_{I,j} + \left(\frac{\rho_{I,J+1} + \rho_{I,J}}{2}\right) v_{I,j+1}\right] \tag{III.43}$$

$$D_w = \frac{\Gamma_{I-1,J-1} + \Gamma_{I,J-1} + \Gamma_{I-1,J} + \Gamma_{I,J}}{4(x_I - x_{I-1})} \tag{III.44}$$

$$D_e = \frac{\Gamma_{I,J-1} + \Gamma_{I+1,J-1} + \Gamma_{I,J} + \Gamma_{I+1,J}}{4(x_{I+1} - x_I)} \tag{III.45}$$

$$D_s = \frac{\Gamma_{I,J-1}}{y_j - y_{j-1}} \tag{III.46}$$

$$D_n = \frac{\Gamma_{I,J}}{y_{j+1} - y_j} \tag{III.47}$$

III.5 VELOCITY-PRESSURE COUPLING

The Navier-Stokes equations cannot be solved independently for each velocity component because the continuity equation imposes a constraint that relates to all three components of velocity or momentum. However, if we divide the resolution by component, we refer to it as velocity prediction, which needs to be followed by a correction step to satisfy the incompressibility condition, for example ($div\vec{V} = 0$).

There are several methods that can be categorized into two families: one eliminates the pressure problem by taking the curl of the Navier-Stokes equation, and the other addresses pressure by establishing a specific equation. In the first case, we have the Vorticity-Vector Potential formulation in 3D or the Vorticity-Current Function formulation in 2D ($\Omega - \Psi$). In

the second case, we have the Primitive Speed-Pressure (*P*, *V*) formulation. In certain applications, the energy equation can also be coupled, such as in the case of natural convection.

The coupling problem arises due to the presence of velocity and pressure variables in both momentum equations. The pressure gradient acts as the driving force in these equations. Unfortunately, there is no transport equation available for the pressure variable, unlike the two velocity components. In other words, if the pressure gradient is known in advance, we can calculate the velocity field that satisfies the continuity equation. However, pressure is always as unknown as velocity. A given velocity field may satisfy the continuity equation but not the momentum transport equations. This characteristic of the equations necessitates the use of a pressure-velocity coupling algorithm.

III.5.1 SIMPLER Algorithm

Techniques for coupling the Navier-Stokes equations, equivalent to the projection method, were developed and implemented by Spalding and Patankar at Imperial College London in the 1960s-1970s. These techniques gave rise to multiple versions known as SIMPLE, SIMPLER, SIMPLEST, and so on.

The most universal and widely used algorithm is undoubtedly the SIMPLE algorithm by Patankar and Spalding [15]. Subsequent variations include SIMPLEC (van Doormal and Raithby [22]), PISO (Issa [23]), and SIMPLER (Patankar [16]), which were used in this work.

The superiority of the SIMPLER algorithm over SIMPLE lies in the fact that the derivation of the pressure equation does not involve any simplifications. In SIMPLE, the derivation of the pressure correction equation involves canceling out the term $\sum a_{nb} u'_{nb}$. Consequently, the pressure field in SIMPLER is closer to reality than that in SIMPLE since estimating an initial velocity field is generally easier than estimating a pressure field. It is worth noting that the SIMPLER algorithm does not require an initial pressure field. The pressure is directly generated from the initialization of the velocity. As a result, more consistent under-relaxation coefficients can be used for the velocities. Furthermore, no under-relaxation is necessary for the pressure. While it is true that one iteration following the SIMPLER algorithm takes about 30% more time than that of SIMPLE, this effort is largely compensated by a significant reduction in the number of iterations required for convergence.

However, in terms of computational convergence speed, the SIMPLER algorithm is 30% to 50% more efficient than SIMPLE, according to Anderson [24] and Jang [25].

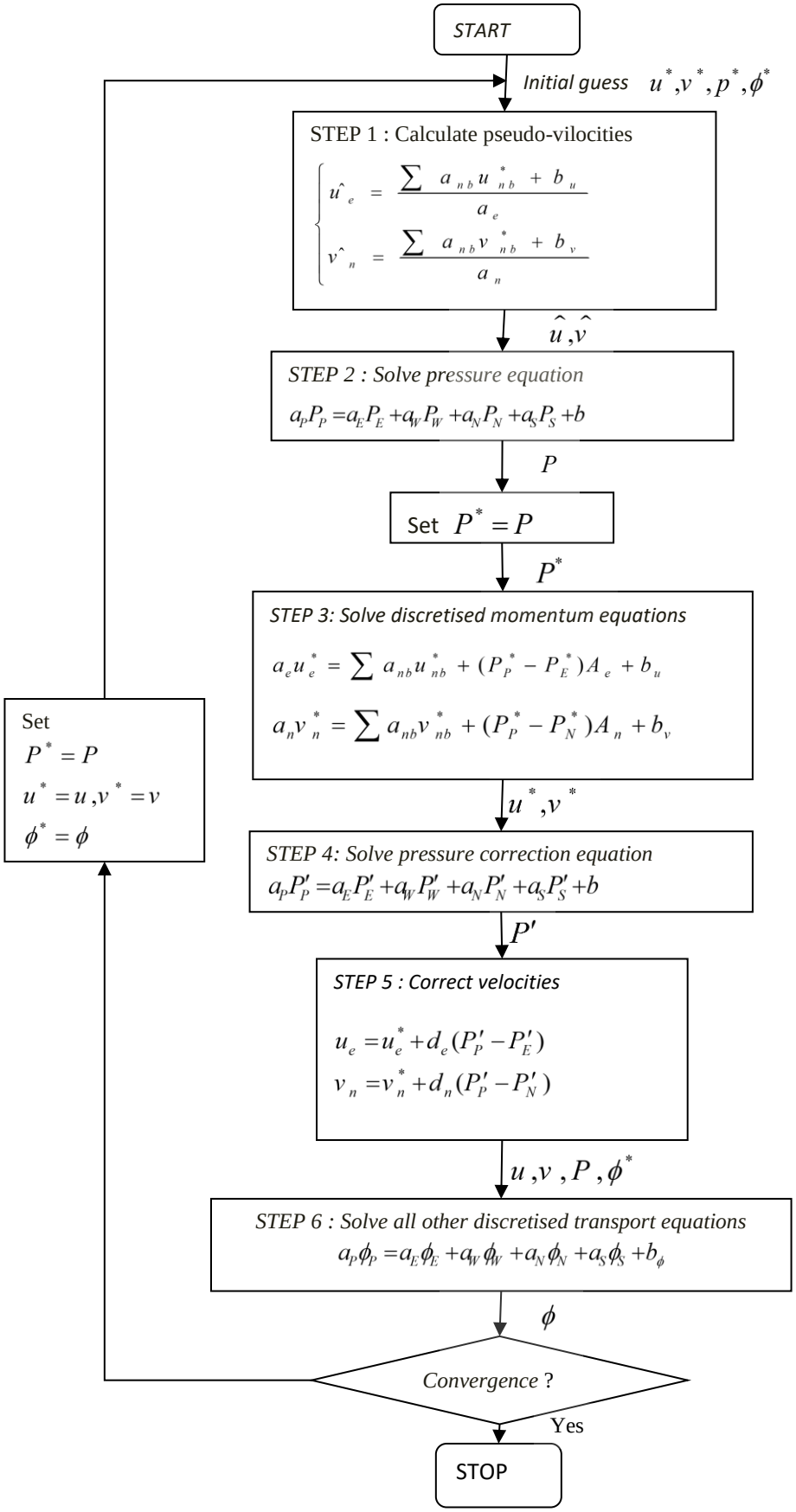

Figure III.9: SIMPLER algorithm.

III.5.2 SIMPLER transient algorithm

To describe transient phenomena, a temporal discretization is performed in addition to the spatial discretization. This is characterized by the time step Δt .

The *SIMPLER* algorithm, used to solve steady-state problems, can also be used to solve unsteady-state problems. The momentum equations now contain unsteady terms.

In unsteady regimes, with implicit formulation; the iterative SIMPLER procedure is applied at each time level until convergence is achieved. Figure III.10 shows the structure of the algorithm.

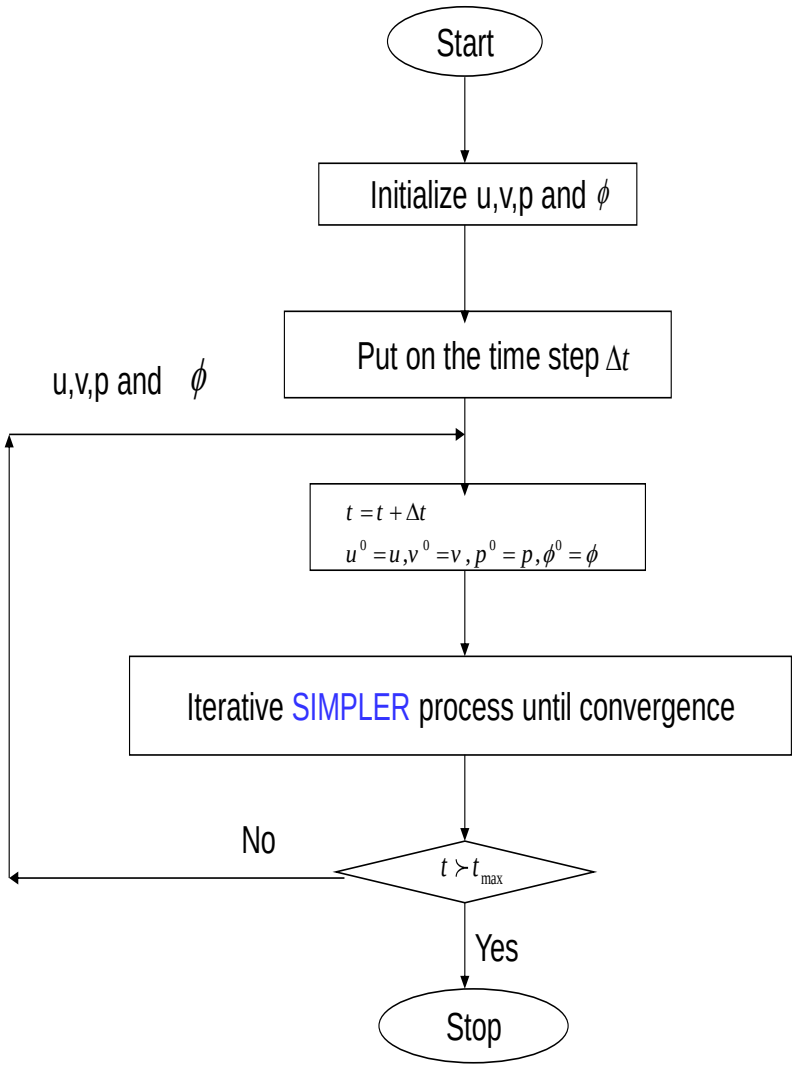

Figure III.10: Transient SIMPLER algorithm.

III.6 RELAXATION

The iterative process used in SIMPLER requires controlling the rate of change of the unknowns at each iteration. This is accomplished through sub-relaxation methods [24]:

Consider ϕ_P^* the value of ϕ_P at the current iteration. If ϕ_P satisfies equation:

$$a_P \phi_P = \sum_{nb} a_{nb} \phi_{nb} + b \tag{III.48}$$

So, for the system to be solved for the current iteration, we estimate a value of ϕ_P given by:

$$\phi_P = \frac{\sum_{nb} a_{nb} \phi_{nb} + b}{a_P} \tag{III.49}$$

The change in ϕ_P from one iteration to the next is given by:

$$\phi_P = \frac{\sum_{nb} a_{nb} \phi_{nb} + b}{a_P} - \phi_P^* \tag{III.50}$$

The change in ϕ_P is a fraction α defined by:

$$\phi_P = \phi_P^* + \alpha \left(\frac{\sum_{nb} a_{nb} \phi_{nb} + b}{a_P} - \phi_P^* \right) \tag{III.51}$$

After rearranging the terms, we find:

$$\frac{a_P}{\alpha} \phi_P = \sum_{nb} a_{nb} \phi_{nb} + b + \frac{1-\alpha}{\alpha} a_P \phi_P^* \tag{III.52}$$

Thus, the new value of the magnitude ϕ_P depends on the previous value ϕ_P^* and its correction $\Delta\phi = \frac{\sum_{nb} a_{nb} \phi_{nb} + b}{a_P} - \phi_P^*$ using the under-relaxation coefficient α whose value is strictly less than 1.

III.7 SOLVING THE LINEAR SYSTEM OF DISCRETIZED EQUATIONS

III.7.1 THOMAS algorithm (TDMA)

Developed by Thomas in 1949, this is a direct method for one-dimensional (1D) situations but can be used iteratively line by line to solve two-dimensional (2D) problems.

Finite volume discretization yields a tridiagonal system for the 1D case, a penta-diagonal system for the 2D case and a septa-diagonal system for the 3D case. Other discretization schemes give more than one diagonal, e.g., the QUICK scheme gives seven diagonals in the 2D case. In this case, the source term is two diagonals.

A tridiagonal system can be written in the general form, (see [26] for details):

$$a_i \phi_{i-1} + b_i \phi_i + c_i \phi_{i+1} = d_i \tag{III.53}$$

In matrix form, this system can be written as

$$\begin{bmatrix} b_1 & c_1 & 0 & & & 0 \\ a_2 & b_2 & c_2 & & & \\ & a_3 & b_3 & c_3 & . & \\ & & . & . & . & c_{n-1} \\ 0 & & & & a_n & b_n \end{bmatrix} \begin{bmatrix} \phi_1 \\ \phi_2 \\ . \\ . \\ \phi_n \end{bmatrix} = \begin{bmatrix} d_1 \\ d_2 \\ . \\ . \\ d_n \end{bmatrix} \tag{III.54}$$

The calculation is as follows:

- For i=2, we use the equations:

$$P_2 = \frac{b_2}{a_2},\ Q_2 = \frac{d_2 + c_2 \phi_1}{a_2} \tag{III.55}$$

- For i varying from 3 to N-1, we use the equations:

$$P_i = \frac{b_i}{a_i - c_i P_{i-1}},\ \ Q_i = \frac{d_i + c_i Q_{i-1}}{a_i - c_i P_{i-1}} \tag{III.56}$$

With $P_N = 0$ and $Q_N = \phi_N$ (where ϕ_N is a boundary condition).

The last step determines the unknowns; for i varying from N-1 to 1, we use equation: $\phi_i = P_i \phi_{i+1} + Q_i$

ϕ_1 and ϕ_N are domain boundary values.

III.7.1.1 Application of the THOMAS algorithm to 2D problems (TDMA)

Thomas' algorithm (TDMA) can be applied iteratively to solve a two-dimensional system of equations [20]. Let's consider the mesh considered in Figure III.11 and a general transport equation discretized as:

$$a_P \phi_P = a_E \phi_E + a_W \phi_W + a_N \phi_N + a_S \phi_S + b \tag{III.57}$$

To solve this system, Thomas' algorithm is applied for a selected line, for example the North-South (N-S) line. The discretized transport equation is rearranged as:

$$-a_S\phi_S + a_P\phi_P - a_N\phi_N = a_E\phi_E + a_W\phi_W + b \tag{III.58}$$

The right-hand side of equation (III.58) is assumed to be temporarily known. Equation (III.58) is of the same form as equation (III.53), with:

$$\begin{aligned} \beta_j &= a_S \\ D_j &= a_P \\ \alpha_j &= a_N \\ C_j &= a_W\phi_W + a_E\phi_E + b \end{aligned} \tag{III.59}$$

We can now solve the system along the (N-S) direction of the chosen line for values $j = 2,3,4,.....,n$ as shown in Figure III.11.

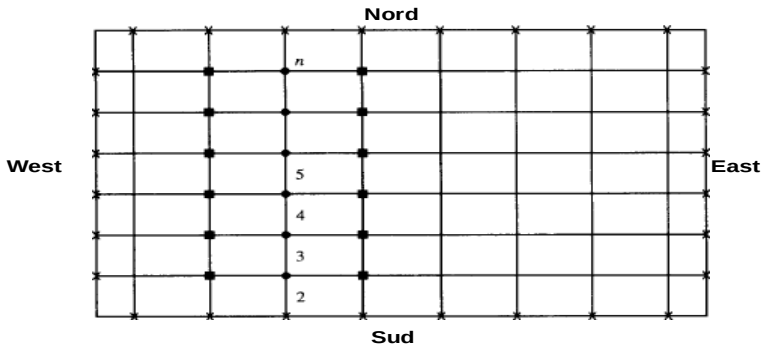

Figure III.11: Line-by-line application of the TDMA method.

- *Points at which values are calculated*
- *Points at which values are considered to be temporarily known*
- ✖ *Known values at the boundary*

On the left-hand side of equation (III.78), only the tridiagonal system can be efficiently solved by Thomas' algorithm. The solution is first calculated on the second row of the control volumes, the values on the first row are assumed to be known (known values on the boundary) and the values on the third row are assumed to be temporarily known. After the [ϕ_2] vector has been calculated using Thomas' algorithm, we move on to the [ϕ_3] vector and assume that the second line has already been calculated (in the previous iteration) and the values of the fourth line are assumed to be temporarily known, then more generally to the [ϕ_j] vector, where the entire resolution zone is thus scanned.

The line-by-line calculation procedure is repeated until the solution reaches convergence.

III.8 CONVERGENCE CRITERION

The convergence criterion used in SIMPLER is $\max\left(\phi_{n+1}-\phi_n\right)\le e_\phi$: , scanning all cells in the domain where *n* is the iteration order and ϕ denotes *U, V* or θ . In most cases e_u , e_v , e_T are taken to be less than 10^{-7}. For pressure and pressure correction, the convergence test is performed on the velocity divergence, which must be less than 10^{-7}. Steady state is assumed to be reached when the deviation between two variables calculated for two successive time steps is less than 10^{-5}.

III.9 CONCLUSION

In this chapter, we have provided a brief overview of the finite volume method as applied to fluid flows and the general steps involved in discretizing the mathematical model. Furthermore, we have presented a detailed explanation of the velocity-pressure coupling algorithms, namely SIMPLE and SIMPLER. Our focus was on the CDS, Upwind, Exponential, Hybrid, and Power schemes, which were selected for their effectiveness in terms of both results and computation time in this particular study. Additionally, we discussed the resolution of algebraic equations using the line-by-line method based on Thomas' algorithm (TDMA).

Moving forward, the next three chapters will apply the methodology outlined thus far to address specific problems. These include the analysis of natural air convection under the low Mach approximation, the coupling of natural convection in the non-Boussinesq case with radiation, and the consideration of a magnetic field gradient during the convection process.

By delving into these topics, we aim to gain deeper insights into the behavior of fluid flows and explore the interaction of convection with various physical phenomena. The application of the finite volume method, along with the specific schemes and algorithms discussed, will provide us with valuable tools to examine and understand these complex scenarios.

References

[1] R. Peyret, T.D. Taylor, Computational Methods for Fluid Flow, Springer Science & Business Media, 2012.

[2] D.L. Book, Finite-Difference Techniques for Vectorized Fluid Dynamics Calculations, Springer Science & Business Media, 2012.

[3] L.H. Msc, The Solution of Partial Differential Equations by Finite Difference Approximations: Analysing the Relative Performance of Differing Numerical Finite Difference Schemes Using Taylor Series Expansions, Amazon Digital Services LLC - Kdp Print Us, 2018.

[4] J. Donea, A. Huerta, Finite Element Methods for Flow Problems, John Wiley & Sons, 2003.

[5] D.W. Pepper, The Intermediate Finite Element Method: Fluid Flow And Heat Transfer Applications, CRC Press, 1999.

[6] O.C. Zienkiewicz, R.L. Taylor, P. Nithiarasu, The Finite Element Method for Fluid Dynamics, Butterworth-Heinemann, 2013.

[7] F. Moukalled, L. Mangani, M. Darwish, The Finite Volume Method in Computational Fluid Dynamics: An Advanced Introduction with Open FOAM® and Matlab, Springer, 2015.

[8] H.K. Versteeg, W. Malalasekera, An Introduction to Computational Fluid Dynamics: The Finite Volume Method, Pearson Education Limited, 2007.

[9] J.N. Reddy, N.K. Anand, P. Roy, Finite Element and Finite Volume Methods for Heat Transfer and Fluid Dynamics, Cambridge University Press, 2022.

[10] R. Petrova, Finite Volume Method: Powerful Means of Engineering Design, BoD – Books on Demand, 2012.

[11] Y. Nait Slimane, Méthodes de volumes finis pour des problèmes de diffusion-convection non-linéaires, These de doctorat, Paris 13, 1997.

[12] C. Canuto, M.Y. Hussaini, A. Quarteroni, T.A. Zang Jr, Spectral Methods in Fluid Dynamics, Springer Science & Business Media, 2012.

[13] S.K. Godunov, I. Bohachevsky, Finite difference method for numerical computation of discontinuous solutions of the equations of fluid dynamics, Mat. Sb. 47(89) (1959) 271–306.

[14] J. Glimm, Solutions in the large for nonlinear hyperbolic systems of equations, Commun. Pure Appl. Math. 18 (1965) 697–715.https://doi.org/10.1002/cpa.3160180408.

[15] S.V. Patankar and D.G. Spalding, Heat and Mass Transfer in Boundary Layers. 2nd edition. Intertext Books, 1970. 255 pp. £6. | Semantic Scholar, (n.d.).

[16] S. Patankar, Numerical Heat Transfer and Fluid Flow, CRC Press, Boca Raton, 2018. https://doi.org/10.1201/9781482234213.

[17] F.H. Harlow, J.E. Welch, Numerical Calculation of Time-Dependent Viscous Incompressible Flow of Fluid with Free Surface, Phys. Fluids. 8 (1965) 2182–2189. https://doi.org/10.1063/1.1761178.

[18] C.M. Rhie, W.L. Chow, Numerical study of the turbulent flow past an airfoil with trailing edge separation | AIAA Journal, (n.d.). https://arc.aiaa.org/doi/10.2514/3.8284 AIAA Journal, Vol. 21(11), pp. 1525-1532, 1983.

[19] G.D. Thiart, Finite difference scheme for the numerical solution of fluid flow and heat transfer problems on nonstaggered grids, Numer. Heat Transf. 17 (1990) 43–62.

[20] S. V. Patankar, A calculation procedure for two-dimensional elliptic situations - NASA/ADS, (n.d.). Num. Heat Transfer. Part A, Vol. 14(25), pp. 409, 1981.

[21] D. B. Spalding, A novel finite difference formulation for differential expressions involving both first and second derivatives - Spalding - 1972 - International Journal for Numerical Methods in Engineering - Wiley Online Library, (n.d.). Vol.4(4), pp.551-559, 1972.

[22] J.P. Van Doormaal, G.D. Raithby, Enhancements of the Simple Method for Predicting Incompressible Fluid Flows, Numer. Heat Transf. 7 (1984) 147–163. https://doi.org/10.1080/01495728408961817.

[23] R.I. Issa, Solution of the implicitly discretised fluid flow equations by operator-splitting, J. Comput. Phys. 62 (1986) 40–65. https://doi.org/10.1016/0021-9991(86)90099-9.

[24] D.A. Pletcher John C. Tannehill, Richard H., Computational Fluid Mechanics and Heat Transfer, 3rd ed., CRC Press, Boca Raton, 2012. https://doi.org/10.1201/b12884.

[25] D.S. Jang, R. Jetli, S. Acharya, Comparison of the Piso, Simpler, and Simplec Algorithms for the Treatment of the Pressure-Velocity Coupling in Steady Flow Problems, Numer. Heat Transf. Part - Appl. 10 (1986) 209–228.

[26] G.D. Smith, Numerical Solution of Partial Differential Equations: Finite Difference Methods, Clarendon Press, 1985.

IV.1 INTRODUCTION

Natural convection in a porous media enclosure has received considerable attention from the research community in recent years due to its many applications in engineering and environmental problems. The comprehensive literature on these applications can be found in Adjal et al. [1], Astanina et al. [2], Wu et al. [3], Dutta et al. [4], and others. Various enclosure geometries, including square [5–7], rectangular [8], triangular [9, 10], parallelepiped [11], trapezoidal [12], quadrantal [13], cubic [14], and rhombic cavities [4], have been studied.

The square cavity has been one of the most extensively studied geometries, particularly in conjunction with internal heat generation and other phenomena such as magnetic fields [15, 16], surface radiation [17], volumetric radiation [18], and porous media [19, 20]. The extended Darcy model, which incorporates the Forchheimer and Brinkman extensions [21], has been frequently employed to account for porous media effects.

Recent studies by N. Hdhiri et al. [19] and S. Hamimid et al. [17] have explored natural convection heat transfer in differentially heated square cavities filled with working fluids and porous media. These studies have examined the influence of parameters such as Prandtl number, emissivity, and internal heat generation on heat transfer rates and flow patterns. Similarly, M. S. Astanina et al. [5] investigated transient natural convection with temperature-dependent viscosity within a partially porous square cavity, while M.G. Sobamowo et al. [22] analyzed the thermal performance of a natural convection porous fin with temperature-dependent thermal conductivity and internal heat generation.

Other studies have delved into the effects of heat sink and heat source on entropy generation, MHD natural convection flow, and heat transfer in tilted porous enclosures filled with nanofluids [23], as well as the heat removal process of a heat-generating porous bed using bottom injection of a cold fluid [24]. The influence of porous medium permeability on flow mechanisms has been explored, along with the natural convection cooling of a heat source implanted on the bottom wall of a nanofluid-filled enclosure [25].

Despite these studies, there remains a gap in the research regarding the coupling between porous media, natural convection, and internal heat generation. Therefore, the objective of this chapter is to examine how the presence of a porous medium and internal heat generation affect fluid flow and heat transfer in a square cavity. The study aims to provide a better understanding of the combined effects of influential parameters such as external Rayleigh number (Ra_E), internal Rayleigh number (Ra_I), porosity (ε), and Darcy number (Da), with a particular focus on the competition between the two Rayleigh numbers (Ra_I and Ra_E).

IV.2 PHYSICAL MODEL AND GOVERNING EQUATIONS

The studied domain is a two-dimensional square enclosure of dimension H. It contains a fluid-saturated porous layer of finite thickness that is located in the center of the cavity and surrounded by two vertical fluid layers of equal widths. The vertical surfaces are maintained at constant temperatures T_C and T_H, leading to free convection motions within the cavity, and the horizontal walls are assumed to be adiabatic. Figure IV.1 depicts the composite

fluid/porous system, boundary conditions, and coordinate system for the problem under investigation.

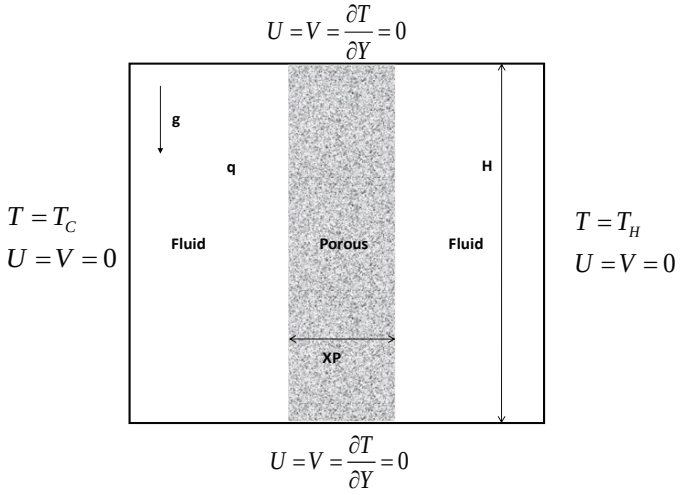

Figure IV.1: Schematic representation of the cavity

The fluid is assumed to be homogeneous and laminar and satisfies the classical hypotheses of an incompressible Newtonian fluid with internal heat generation. The porous medium is completely saturated by the fluid and is assumed to be macroscopically isotropic, homogeneous and in local thermal equilibrium. In addition, the thermophysical properties of the porous medium are considered constant. Moreover, it is hypothesized that the temperature differences in the flow domain under consideration are small enough to justify the employment of the Boussinesq approximation.

$$\rho(T) = \rho_0[1 - \beta(T - T_0)] \tag{IV.1}$$

Where: $\beta = -\frac{1}{\rho_0}(\frac{\partial \rho}{\partial T})_P$

Also, the Darcy-Brinkman-Forchheimer model is used in the momentum equation [20].

The conservation equations of mass, momentum and energy can be expressed as follows:

Fluid Region

$$\frac{\partial u}{\partial x} + \frac{\partial v}{\partial y} = 0 \tag{IV.2}$$

$$\rho\left(\frac{\partial u}{\partial t} + u\frac{\partial u}{\partial x} + v\frac{\partial u}{\partial y}\right) = -\frac{\partial p}{\partial x} + \mu(\frac{\partial^2 u}{\partial x^2} + \frac{\partial^2 u}{\partial y^2}) \tag{IV.3}$$

$$\rho\left(\frac{\partial v}{\partial t} + u\frac{\partial v}{\partial x} + v\frac{\partial v}{\partial y}\right) = -\frac{\partial p}{\partial y} + \mu(\frac{\partial^2 v}{\partial x^2} + \frac{\partial^2 v}{\partial y^2}) - \rho_{ref} g \tag{IV.4}$$

$$\rho C_P \frac{\partial T}{\partial t} + \rho C_P\left(u\frac{\partial T}{\partial x} + v\frac{\partial T}{\partial y}\right) = k\left(\frac{\partial^2 T}{\partial x^2} + \frac{\partial^2 T}{\partial y^2}\right) + q \tag{IV.5}$$

With: $\rho_{ref} = \rho - \rho_0 = -\rho_0\beta(T - T_0)$

Porous region

$$\frac{\partial u}{\partial x}+\frac{\partial v}{\partial y}=0 \tag{IV.6}$$

$$\frac{1}{\varepsilon}\frac{\partial u}{\partial t}+\frac{1}{\varepsilon^2}u\frac{\partial u}{\partial x}+\frac{1}{\varepsilon^2}v\frac{\partial u}{\partial y}=-\frac{1}{\rho}\frac{\partial p}{\partial x}+\frac{\mu_{eff}}{\rho\varepsilon}\nabla^2 u-D_x \tag{IV.7}$$

$$\frac{1}{\varepsilon}\frac{\partial v}{\partial t}+\frac{1}{\varepsilon^2}u\frac{\partial v}{\partial x}+\frac{1}{\varepsilon^2}v\frac{\partial v}{\partial y}=-\frac{1}{\rho}\frac{\partial p}{\partial y}+\frac{\mu_{eff}}{\rho\varepsilon}\nabla^2 v+\beta(T-T_0)g-D_y \tag{IV.8}$$

$$\left(\rho C_p\right)_{eff}\frac{\partial T}{\partial t}+\left(\rho C_p\right)_f\left(u\frac{\partial T}{\partial x}+v\frac{\partial T}{\partial y}\right)=k_{eff}\left(\frac{\partial^2 T}{\partial x^2}+\frac{\partial^2 T}{\partial y^2}\right)+q \tag{IV.9}$$

$$\left(\rho C_p\right)_{eff}=\varepsilon.\left(\rho C_p\right)_f+(1-\varepsilon)\left(\rho C_p\right)_s \tag{IV.10}$$

Where D_x and D_y, represent the matrix drags per unit volume of the porous medium in x and y direction respectively.$|\vec{V}|$ is the magnitude of the velocity vector given by:

$$\left|\vec{V}\right|=\sqrt{u^2+v^2} \tag{IV.11}$$

The solid matrix drag per unit volume can be expressed in the following form:

$$D=AV+BV^2 \tag{IV.12}$$

For a one-dimensional flow with velocity V, the above form of drag expression is supported by a number of packed bed and fluidized bed correlations, including the widely used Ergun's (1952) correlation.

It can be shown that the contribution of the solid matrix drag for a two-dimensional flow takes the following form:

$$D_x=Au+B(u^2+v^2)^{\frac{1}{2}}u \tag{IV.13}$$

$$D_y=Av+B(u^2+v^2)^{1/2}v \tag{IV.14}$$

The constants A and B involved in the Ergun's correlation are given by:

$$A=150\frac{(1-\varepsilon)^2}{\varepsilon^3}\frac{\mu_f}{D_p^2} \tag{IV.15}$$

$$B=1.75\frac{(1-\varepsilon)}{\varepsilon^3}\frac{\rho_f}{D_p} \tag{IV.16}$$

Where D_p is the effective diameter of particles.

By introducing the permeability K of the medium:

$$K=\frac{\varepsilon^3 D_p^2}{150(1-\varepsilon)^2} \tag{IV.17}$$

The solid matrix drag components D_x, D_y, become:

$$D_x=\frac{\mu_f}{K}u+\frac{1.75}{\sqrt{150}}\frac{\rho_f}{\sqrt{K}}\frac{|\vec{V}|}{\varepsilon^{3/2}}u \tag{IV.18}$$

$$D_y=\frac{\mu_f}{K}v+\frac{1.75}{\sqrt{150}}\frac{\rho_f}{\sqrt{K}}\frac{|\vec{V}|}{\varepsilon^{3/2}}v \tag{IV.19}$$

The effective properties of the porous medium, k_{eff}, $(\rho C_p)_{eff}$ and μ_{eff} generally depend on its porosity and the tortuosity of the solid phase as well as the local fluid velocity. In this work, the interest is not focused on the effects of these parameters, but for simplicity, the corresponding fluid properties are used throughout the study. The momentum equations in the porous region thus become:

$$\frac{1}{\varepsilon}\frac{\partial u}{\partial t}+\frac{1}{\varepsilon^2}u\frac{\partial u}{\partial x}+\frac{1}{\varepsilon^2}v\frac{\partial u}{\partial y}=-\frac{1}{\rho}\frac{\partial p}{\partial x}+\frac{\mu}{\rho\varepsilon}\nabla^2 u-\frac{\mu}{\rho K}u-\frac{1.75}{\sqrt{150}}\frac{1}{\sqrt{K}}\frac{|\vec{V}|}{\varepsilon^{3/2}}u \quad \text{(IV.20)}$$

$$\frac{1}{\varepsilon}\frac{\partial v}{\partial t}+\frac{1}{\varepsilon^2}u\frac{\partial v}{\partial x}+\frac{1}{\varepsilon^2}v\frac{\partial v}{\partial y}=-\frac{1}{\rho}\frac{\partial p}{\partial y}+\frac{\mu}{\rho\varepsilon}\nabla^2 v+\beta(T-T_0)g-\frac{\mu}{\rho K}v-\frac{1.75}{\sqrt{150}}\frac{1}{\sqrt{K}}\frac{|\vec{V}|}{\varepsilon^{3/2}}v \quad \text{(IV.21)}$$

The governing equations are converted to non-dimensional form using the following non-dimensional variables:

$$\boldsymbol{\tau}=\frac{\boldsymbol{t}}{\frac{\boldsymbol{H^2}}{\boldsymbol{\alpha}}},\ \boldsymbol{X}=\frac{\boldsymbol{x}}{\boldsymbol{H}},\ \boldsymbol{Y}=\frac{\boldsymbol{y}}{\boldsymbol{H}},\ \boldsymbol{U}=\frac{\boldsymbol{uH}}{\boldsymbol{\alpha}},\ \boldsymbol{V}=\frac{\boldsymbol{vH}}{\boldsymbol{\alpha}},$$

$$\boldsymbol{P}=\frac{\boldsymbol{\varepsilon^2 pH^2}}{\boldsymbol{\rho\alpha^2}},\ \boldsymbol{\theta}=\frac{\boldsymbol{T-T_0}}{\boldsymbol{\Delta T}},\ \boldsymbol{\Delta T}=\boldsymbol{T_H}-\boldsymbol{T_C},\ \boldsymbol{T_0}=\frac{\boldsymbol{T_H+T_C}}{\boldsymbol{2}}$$

Considering the previous assumptions, the governing equations for an unsteady 2-D problem can be written in dimensionless form:

Fluid Region

$$\frac{\partial U}{\partial X}+\frac{\partial V}{\partial Y}=0 \quad \text{(IV.22)}$$

$$\frac{\partial U}{\partial \tau}+U\frac{\partial U}{\partial X}+V\frac{\partial U}{\partial Y}=-\frac{\partial P}{\partial X}+Pr\,\nabla^2 U \quad \text{(IV.23)}$$

$$\frac{\partial V}{\partial \tau}+U\frac{\partial V}{\partial X}+V\frac{\partial V}{\partial Y}=-\frac{\partial P}{\partial Y}+Pr\,\nabla^2 V+Ra_E\,Pr\,\theta \quad \text{(IV.24)}$$

$$\frac{\partial \theta}{\partial \tau}+\left(U\frac{\partial \theta}{\partial X}+V\frac{\partial \theta}{\partial Y}\right)=\left(\frac{\partial^2\theta}{\partial X^2}+\frac{\partial^2\theta}{\partial Y^2}\right)+\frac{Ra_I}{Ra_E} \quad \text{(IV.25)}$$

Ra_E and Ra_I are the external and the internal Rayleigh numbers defined respectively as:

$Ra_E=\frac{g\beta\Delta TH^3}{(v\alpha)}$ and $Ra_I=\frac{g\beta qH^5}{(v\alpha k)}$

Porous region

$$\frac{\partial U}{\partial X}+\frac{\partial V}{\partial Y}=0 \quad \text{(IV.26)}$$

$$\varepsilon\frac{\partial U}{\partial \tau}+U\frac{\partial U}{\partial X}+V\frac{\partial U}{\partial Y}=-\frac{\partial P}{\partial X}+Pr\,\varepsilon\,\nabla^2 U-\frac{Pr}{Da}\varepsilon^2 U-1.75\sqrt{\frac{\varepsilon}{150Da}}\left|\sqrt{U^2+V^2}\right|U \quad \text{(IV.27)}$$

$$\varepsilon\frac{\partial V}{\partial \tau}+U\frac{\partial V}{\partial X}+V\frac{\partial V}{\partial Y}=-\frac{\partial P}{\partial Y}+Pr\,\varepsilon\,\nabla^2 V+Ra_E\,Pr\,\varepsilon^2\,\theta-\frac{Pr}{Da}\varepsilon^2 V-$$
$$1.75\sqrt{\frac{\varepsilon}{150Da}}\left|\sqrt{U^2+V^2}\right|V \quad \text{(IV.28)}$$

$$\sigma \frac{\partial \theta}{\partial \tau} + \left(U \frac{\partial \theta}{\partial X} + V \frac{\partial \theta}{\partial Y} \right) = \left(\frac{\partial^2 \theta}{\partial X^2} + \frac{\partial^2 \theta}{\partial Y^2} \right) + \frac{Ra_I}{Ra_E} \quad \text{(IV.29)}$$

With: $\sigma = \frac{\varepsilon.(\rho C_p)_f + (1-\varepsilon)(\rho C_p)_s}{(\rho C_P)_f}$

The boundary conditions on the vertical walls are:

$U = V = 0$, $\theta = \theta_C = -0.5$ at $X = 0$ for $0 \le Y \le 1$

$U = V = 0$, $\theta = \theta_H = 0.5$ at $X = 1$ for $0 \le Y \le 1$

The adiabaticity conditions applied on the horizontal walls gives:

$U = V = 0$, $\frac{\partial \theta}{\partial Y} = 0$ at $Y = 0$ for $0 \le X \le 1$

$U = V = 0$, $\frac{\partial \theta}{\partial Y} = 0$ at $Y = 1$ for $0 \le X \le 1$

IV.3 NUMERICAL PROCEDURE

A finite volume approach with a staggered grid is used to numerically solve the governing equations and boundary conditions. The control volumes of the grid are employed to integrate the conservation equations, and a power scheme is applied to approximate the advection-diffusion terms.

The outer iterative loop, known as the unsteady SIMPLER algorithm, is repeated until a steady state is reached, indicated by the simultaneous satisfaction of the following convergence criteria: $\left|\varphi_{ij}^{new} - \varphi_{ij}^{old}\right| \le 10^{-5}$, where φ represents the variables U, V or θ.

The average Nusselt number, which characterizes the contribution of convection through the hot vertical wall, is defined as follows:

$$Nu_{av} = -\int_0^1 \frac{\partial \theta(X,Y)}{\partial X}\Big|_{X=1} dY \quad \text{(IV.30)}$$

IV.4 GRID SENSITIVITY AND VALIDATION TEST

A grid sensitivity test is conducted to optimize the balance between required precision and computing time. This is achieved by comparing the average Nusselt numbers on the hot wall at steady state within a grid range from (120×120) to (200×200). The computational parameters for the investigated configuration are as follows: $Ra_E=10^6$, $Ra_I=10^6$, Xp=0.2, ε=0.4, and $Da=10^{-3}$. Figure IV.2 presents the results obtained from various grid configurations. It is observed that the average Nusselt number increases significantly as the grid fineness improves. Particularly, the results for mesh sizes ranging from (160×160) to (200×200) are almost identical. This demonstrates that the solution becomes independent of the mesh size starting from (160×160). Consequently, using a mesh size of (160×160) is considered an ideal compromise between precision and computation time. By employing this mesh size, we can effectively verify the accuracy of the code.

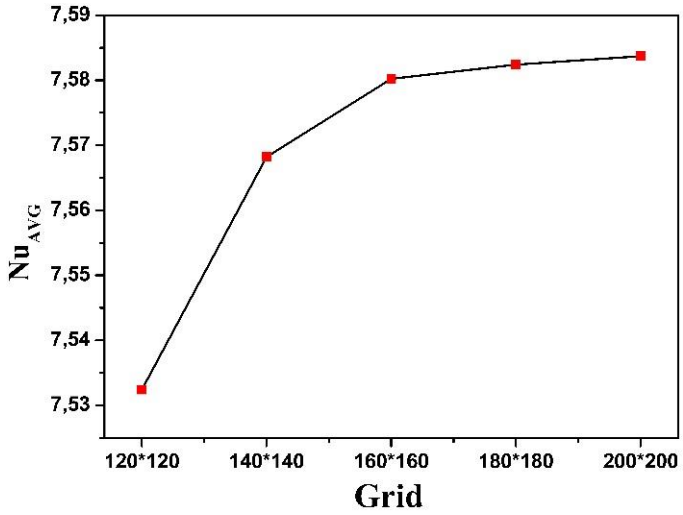

Figure IV.2: Grid size effect on the average Nusselt number

In order to examine the reliability of the proposed formulation, the code is compared to results available in the literature and tested in three different situations, which are all differentially heated cavities.

The first one is completely filled with air in the absence of an internal heat source. Figure IV.3 shows good agreement between the results of the present code and those reported by De Vahl Davis [26]. In the second configuration, the code verification is performed in the case of natural convection with internal heat generation.

The results in Figure IV.4 compare the evolution of the average Nusselt number on the hot wall for different values of the internal source S_Q. A good agreement is obtained by comparing these results with those of Berrahil et al. [16].

The third comparison is with the numerical results of N. Hdhiri et al. [19], considering the case of natural convection with internal heat generation and different working fluids in a porous medium (Figure IV.5). These results thus reinforce the accuracy of the present numerical method and the reliability of our computational code, which allows us to study natural convection in a square enclosure in the presence of an internal heat source and a porous medium.

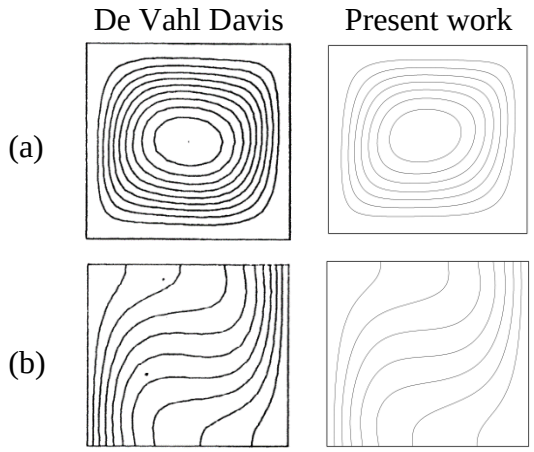

Figure IV.3: Comparison of streamlines (a) and isotherms (b) with the study of De Vahl Davis [26] for Pr=0.71 and Ra=10^4

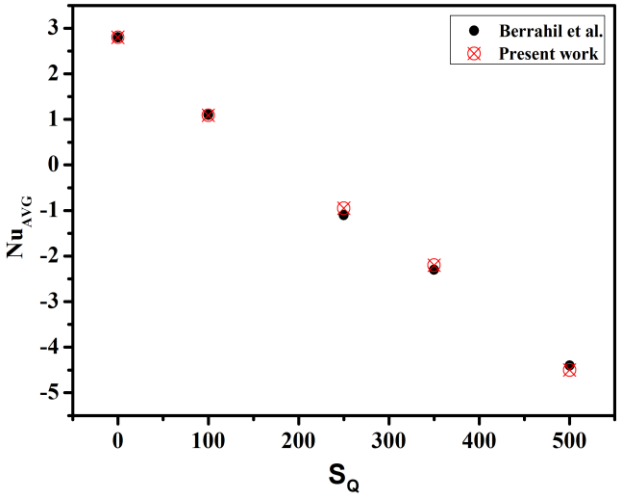

Figure IV.4: Variation of the average Nusselt number on hot wall with internal heat generation compared with the work of Berrahil et al. [16] for Pr=0.0321 and Ra_E=3.21x10^4

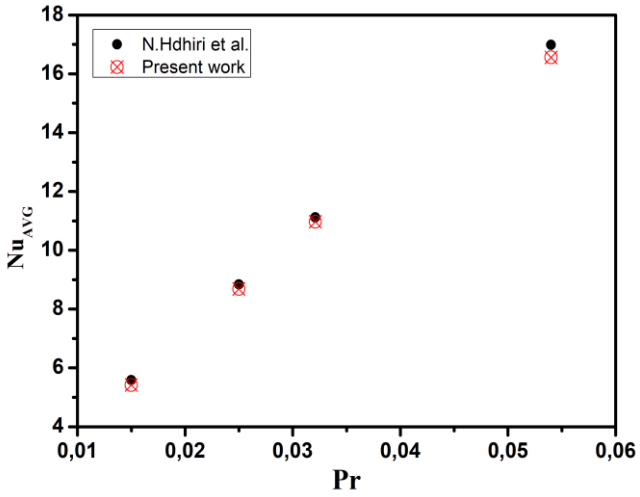

Figure IV.5: Comparison of average Nusselt number values for different Prandlt numbers with the study of N. Hdhiri et al. [19] for S_Q=500, Xp=1, Da=10^{-2} and ε=0.6.

IV.5 RESULTS AND DISCUSSIONS

For a differentially heated square cavity with an internal heat generating fluid at Pr = 0.71, a numerical study is conducted considering the following control parameters: internal Rayleigh number (Ra_I), external Rayleigh number (Ra_E), Darcy number (Da) and the porosity of the porous medium (ε). Particular effort is made to investigate the effects of these parameters on the flow and natural convection heat transfer of the porous.

IV.5.1 Influence of Ra_I and Ra_E on heat transfer and fluid flow

This section presents a typical set of results obtained for streamlines, isotherms, velocities, median temperature and average Nusselt numbers from the numerical code for different values of internal Rayleigh number Ra_I and external Rayleigh number Ra_E. In this case, the fixed parameters are: Da=10^{-3}, Xp=0,2 and ε=0.4.

IV.5.1.1 Flow fields

It can be clearly seen from Figure IV.6 that the highest velocity is obtained for $Ra_E=10^7$ when $Ra_I<7.10^8$, and for $Ra_E = 10^3$ when $Ra_I \geq 7.10^8$.

For law values of the internal Rayleigh number ($Ra_I<10^8$), the maximum velocities increase with Ra_I, except for $Ra_E=10^7$ and increase with increasing Ra_E. For large values of the internal Rayleigh number ($Ra_I>10^8$), the maximum velocity values increase with increasing Ra_I and decrease when Ra_E increases. The profiles of the maximum velocity indicate that the internal and external Rayleigh numbers are the most influential parameters on the flow fields. This effect of internal heat generation on the flow field is reasonable because internal heat generation contributes to buoyancy forces by accelerating the fluid flow (Figure IV.7).

The influence of the internal Rayleigh number (Ra_I) on the streamlines is illustrated in Figure 8 for the following test cases: homogeneous medium (Xp=0), in the presence of a porous layer (Xp=0.2), and a fully porous medium (Xp=1), with $Ra_E=10^6$.

For the two cases of homogeneous medium and fully porous medium, the streamlines are characterized by a single symmetrical counterrotating cell occupying the entire cavity when the ratio $Ra_I/Ra_E < 1$ and by an asymmetrical counterrotating cell occupying the entire cavity when the ratio $Ra_I/Ra_E =1$. This is as a result of the fluid rising in the center and falling on the sides of the enclosure due to buoyant forces produced by the difference in fluid temperature. In addition, although the shape of the circulating cells remains constant, their intensity increases as the internal Rayleigh number increases in both cases (homogeneous medium and porous medium). This asymmetrical cell moves to the left corner at the bottom of the cavity at $Ra_I/Ra_E =10$, and a second cell appears in the right corner at the top of the enclosure. These cells tend to be more intense when the internal Rayleigh number is dominant especially when $Ra_I/Ra_E>10$.

However, in the second case, when a porous layer of thickness Xp=0.2 is present in the center of the cavity, and when $Ra_I/Ra_E<1$, many cells appear due to the high buoyancy forces. When $Ra_I/Ra_E\geq1$, new cells develop and the fluid structure begins to take on new contributions. This is due to the high values of the internal heat generation parameter.

IV.5.1.2 Thermal fields

According to Figure IV.7, the presence of a heat source inside the enclosure causes an increase in the temperature of the fluid and a reduction in convective heat transfer at the hot wall for both low and high buoyancy forces (Figure IV.10). In addition, it can be observed that at high buoyancy forces the reduction in convective heat transfer is less pronounced. This can be attributed to the fluid motion being stronger in comparison to the case of low buoyancy forces.

However, the isotherms in Figure IV.9 depict a symmetric distribution for low values of the internal Rayleigh number (Ra_I), where the contours are almost parallel and the thermal boundary layers are so intense that convection phenomena are established and the external Rayleigh number is dominant. As the internal Rayleigh number (Ra_I) increases and the ration $Ra_I/Ra_E>1$, symmetry is lost and the isothermal density becomes significant near the top wall.

Due to the predominance of internal heat generation, it is the fluid that drives the heat exchange rather than the heated walls, resulting in a decrease in the intensity of thermal boundary layer development.

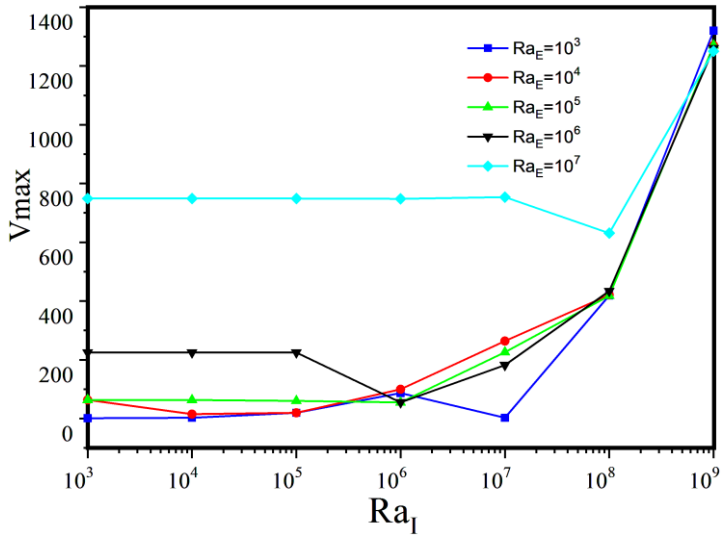

Figure IV.6: Evolution of the maximum velocity values as a function of internal and external Rayleigh numbers for Xp=0.2, Da=10^{-3} and ε=0.4

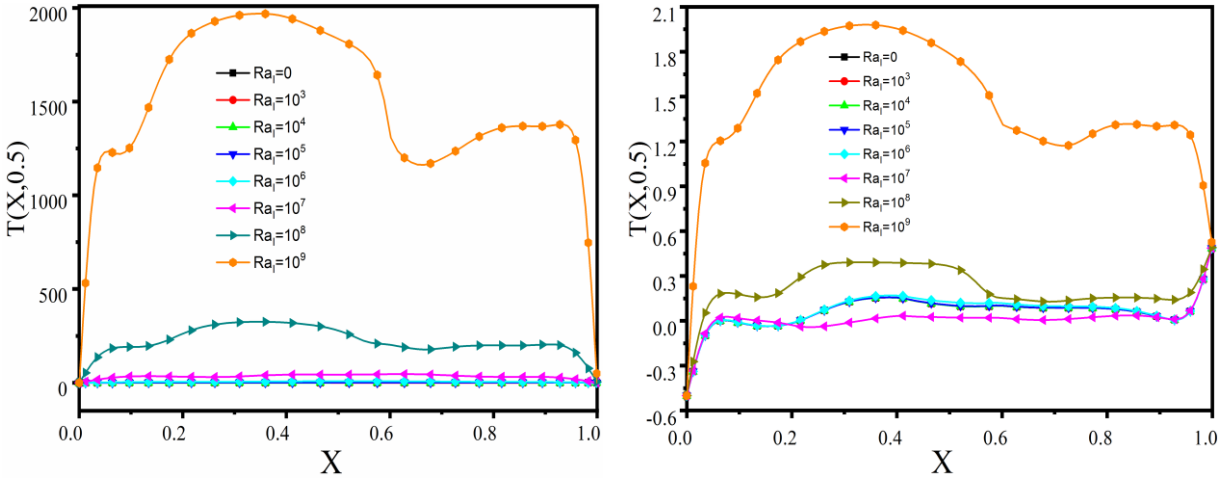

(a) ***(b)***

Figure IV.7: Temperature profiles at mid-height according to internal Rayleigh number for Xp=0.2, Da=10^{-3} and ε=0.4: (a) $Ra_E=10^4$ and (b) $Ra_E=10^7$

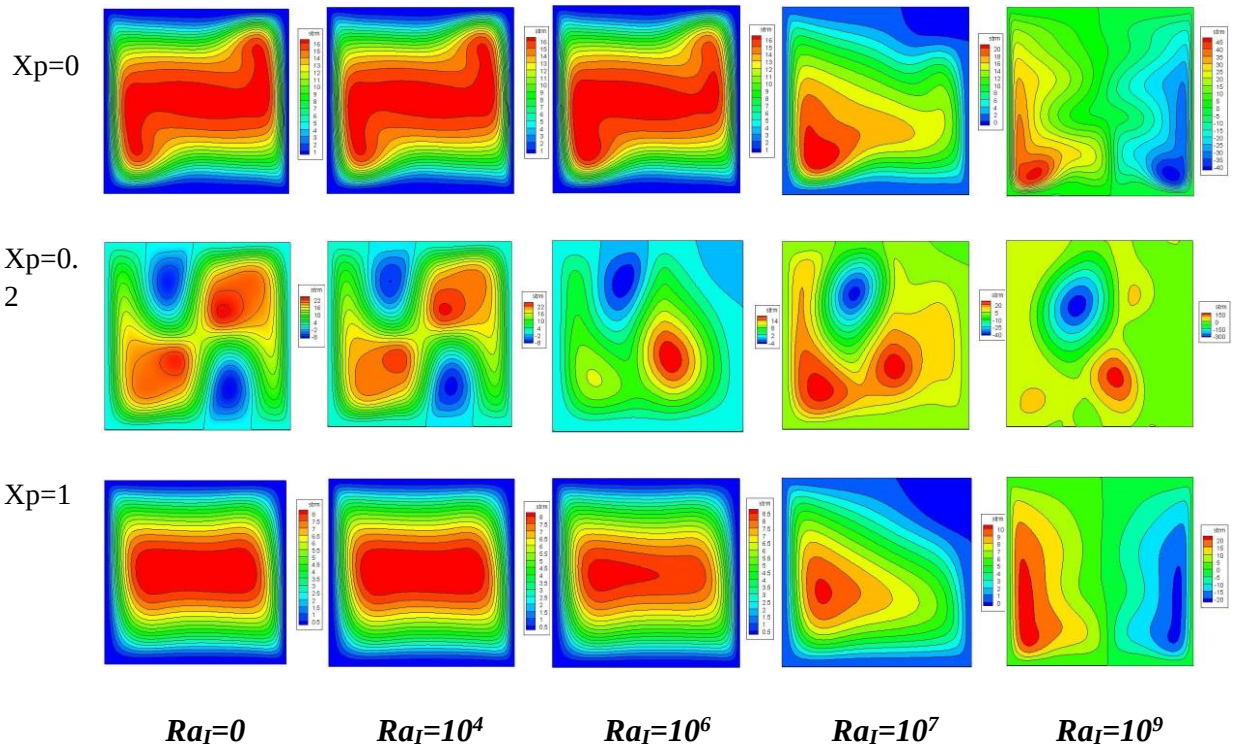

Figure IV.8: Streamlines for various values of Ra_I and $Ra_E=10^6$

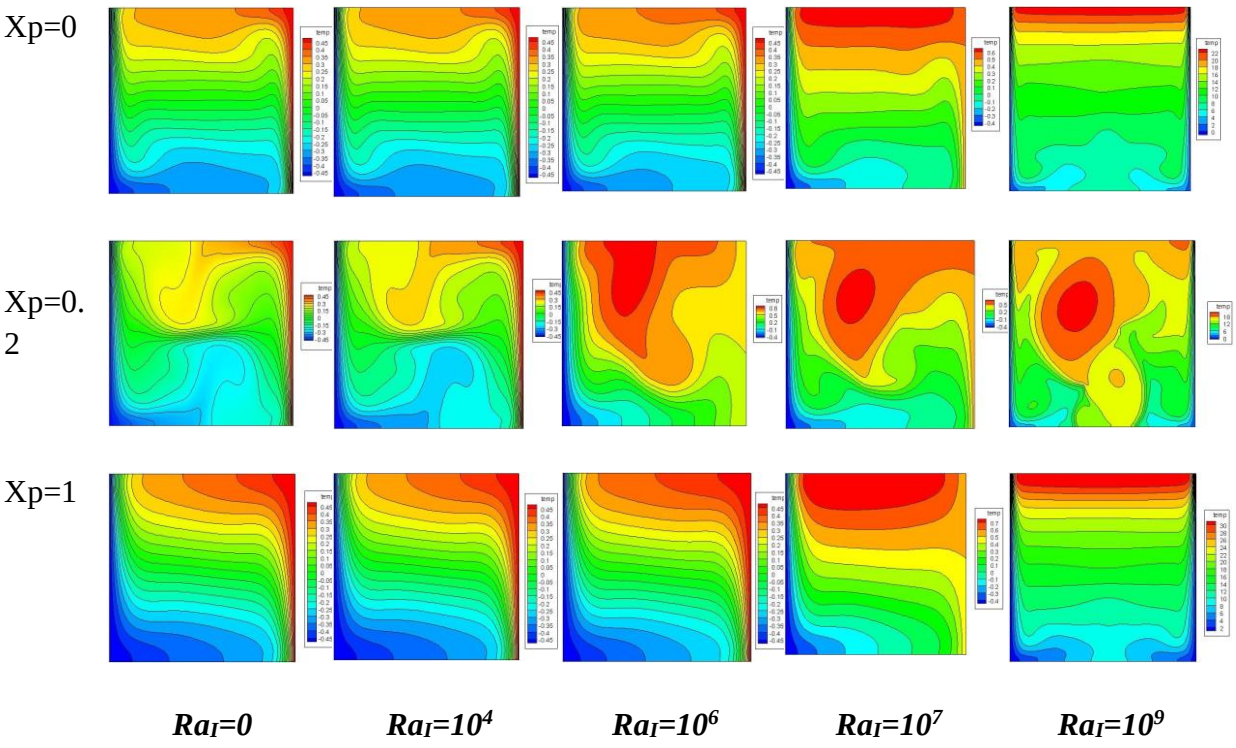

Figure IV.9: Isotherms for various values of Ra_I and $Ra_E=10^6$

As we have seen in Figures IV.7 and IV.8, the ratio Ra_I/ Ra_E is a parameter that affects the flow and temperature fields in the cavity and is also indicative of the heat transfer direction. Accordingly, two distinct regimes are observed. For $Ra_I/Ra_E \leq 1$, external heating is significant and heat transfer is an increasing function of Ra_E. For $Ra_I/Ra_E > 1$, heat

generation in the cavity becomes dominant over external heating and heat transfer becomes an increasing function of Ra_I.

For clarity of presentation and to better highlight these two regimes, Figure IV.10 illustrates the variation of the average Nusselt numbers for different values of the internal Rayleigh number (Ra_I) and the external Rayleigh number (Ra_E). The positive values of Nu_{avg} indicate that there is ascending motion near the hot wall, although circulation is slowed by the buoyancy effect generated by internal heat generation.

Therefore, as Ra_I increases, the average Nusselt number decreases, indicating the descending motion near the hot wall, and the negative sign corresponds to the apparition of the small cells previously shown in Figure IV.8. It is noticeable that the absolute value for the temperature gradient has a maximum value at the hot wall since these cells arrive at the hot wall at the upper corner; thus, the values of the average Nusselt numbers along the hot side wall are governed by the direction and intensity of the flow adjacent to the hot wall.

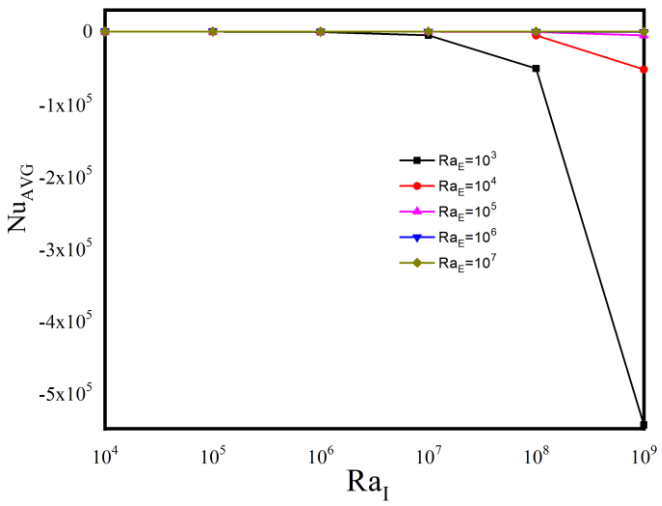

Figure IV.10: Variations of the average Nusselt number on the hot wall as a function of internal and external Rayleigh numbers

Table IV.1 summarizes some of the results obtained in terms of the average heat transfer rate along the hot wall. For $Ra_I = 0$, the average Nusselt number Nu_{avg} increases with Ra_E and takes positive values for $Ra_I/Ra_E \leq 1$.

By having a negative sign, the values of the average Nusselt number are improved by increasing the Ra_I/Ra_E ratio. According to the positive and negative Nusselt numbers, the heat exchange on the active walls results from the variations between their temperatures or that of the fluid, respectively.

It is important to note that when Ra_I/Ra_E is equal to one, the average Nusselt number is always positive. Furthermore, when $Ra_I/Ra_E > 1$ heat transfer is produced by internal heat generation. A general observation clearly shows that as the Ra_I/Ra_E ratio increases, the heat transfer increases.

Table IV.1: Average Nusselt number variations as a function of internal and external Rayleigh numbers

Ra_I \ Ra_E	10^3	10^4	10^5	10^6	10^7
0	1,0098	1,96078	4,20588	8,13745	14,94118
10^3	0,5588	2,20588	4,20588	8,02961	14,94118
10^4	-2,82353	1,48039	4,15686	8,01832	14,94118
10^5	-3,72549	-2,72549	3,71569	8,00941	14,93137
10^6	-496,9274	-42,18628	-0,45098	0,45098	14,88233
10^7	-4976,647	-488,6078	-41,71569	-3,73529	14,69608
10^8	-51088,96	-5099,421	-497,9804	-39,95098	-10,62745
10^9	-544633,9	-52345,53	-5159,451	-484,451	-30,26471

IV.5.2 Effect of Ra_I and Da

Calculations are performed for a wide range of internal Rayleigh number $0 \leq Ra_I \leq 10^9$ and with different Darcy numbers $10^{-6} \leq Da \leq 1$ taking into consideration $Ra_E=10^6$, Xp=0.2 and $\varepsilon = 0.4$. Figure IV.11 shows the relationships of the natural convection parameter Nu_{avg} with the Darcy number and the internal Rayleigh number.

As expected, we observe that the average Nusselt number (Nu_{avg}) increases with increasing Da and decrease with increasing Ra_I. This figure shows a linear dependence of the Nusselt number on the Darcy number, which implies that the strength of convective motions is enhanced with increasing permeability of the porous layer. However, this improvement is reduced near the hot wall when Ra_I is increased for the reasons mentioned previously.

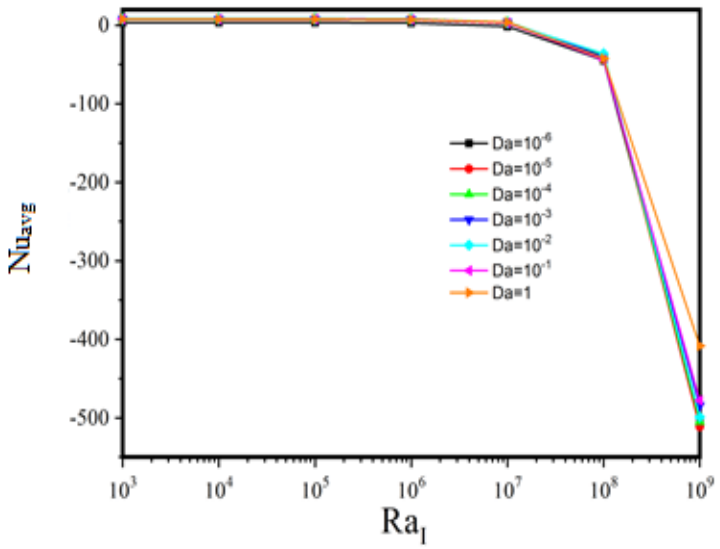

Figure IV.11: Variations of the average Nusselt number as a function of internal Rayleigh numbers and Darcy numbers for $Ra_E=10^6$

Table IV.2 also shows that the average Nusselt number is positive for low heat generation ($Ra_I/Ra_E \leq 1$), and the heat exchange is approximately constant. When $Ra_I = 10^7$, Nu_{avg} starts to take negative values, especially when the permeability of the porous layer is low ($Da=10^{-6}$). From $Ra_I > 10^7$, all values of Nu_{avg} are negative, and the heat transfer tends to improve while considering the negative sign. This means that heat is transferred from the fluid to the hot wall (the hot wall absorbs heat from the higher temperature inner fluid).

On the other hand, for law Darcy number ($Da < 10^{-5}$), heat exchange is important and $Nu_{avg\ is}$ positive except when Ra_I exceeds 10^6. For the highest values of Darcy number ($Da \geq 10^{-5}$), the Nusselt number and heat exchange remain almost constant with respect to Darcy. Figure IV.12 confirms these findings by describing the flow behavior in the cavity and determining the evolution of maximum velocities which increase with increasing Da number.

Table IV.2: Average Nusselt number variations as a function of internal Rayleigh number and Darcy number for $Ra_E=10^6$

Da / Ra_I	10^{-6}	10^{-5}	10^{-4}	10^{-3}	10^{-2}	10^{-1}	1
0	3,54902	7,53922	8,50000	8,02941	7,78431	7,71569	7,66667
10^3	3,54902	7,53922	8,50000	8,01961	7,78431	7,71569	7,66667
10^4	3,53922	7,52941	8,50000	8,01961	7,78431	7,70588	7,65686
10^5	3,50000	7,49020	8,45098	8,12745	7,73529	7,69608	7,67647
10^6	3,04902	7,03922	8,00980	7,68628	7,19608	7,14706	7,26471
10^7	-1,38235	2,77451	3,85294	3,73529	2,97059	3,17647	3,89216
10^8	-44,7255	-38,1078	-37,91177	-39,95098	-36,1078	-43,93137	-42,38235
10^9	-501,784	-511,1078	-504,5392	-484,451	-499,1078	-477,8431	-408,422

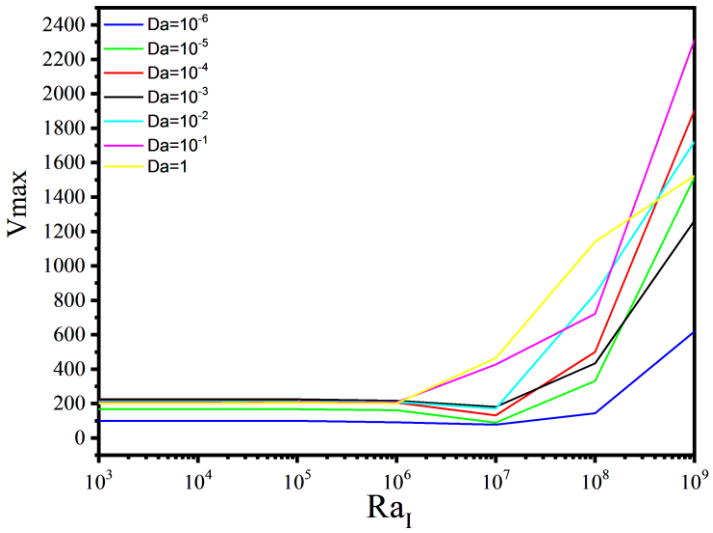

Figure IV.12: Evolution of the maximum velocity values as a function of internal Rayleigh number and Darcy number for $Ra_E=10^6$

IV.5.3 Impact of Ra_I and ε

In this section, computations are performed for a wide range of internal Rayleigh number $0 \leq Ra_I \leq 10^9$, as well as for various porosity values $0.01 \leq \varepsilon \leq 1$. The other parameters are: $Ra_E=10^6$, Xp=0.2 and Da = 10^{-3}. Figure IV.13 shows the variation of the average Nusselt number along the hot wall as a function of porosity and internal Rayleigh number. It can be seen that the heat transfer rate increases with increasing Ra_I. This may be due to enhanced convection, which leads to an increase in fluid temperature.

It is also important to note that increasing porosity does not significantly affect the average Nusselt number, especially for low Ra_I values (see Table IV.3). When $Ra_I/Ra_E>1$ an excellent heat exchange is observed for all values of porosity.

These observations are substantiated by the findings presented in Figure IV.14, which describe the flow characteristics within the cavity and establish a correlation between the evolution of maximum velocities and the increase in porosity. Interestingly, it is revealed that at low Ra_I values (< 10^6), the influence of porosity ε on the flow is minimal, whereas it becomes more pronounced as a function of ε for high internal Rayleigh values.

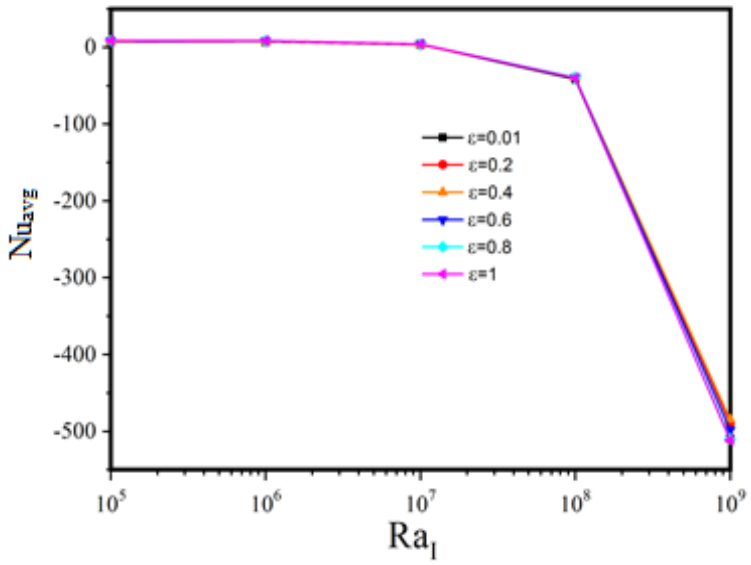

Figure IV.13: Variations of the average Nusselt number as a function of internal Rayleigh number and porosity for Da=10^{-3} and $Ra_E=10^6$

Table IV.3: Average Nusselt number variations as a function of internal Rayleigh number and porosity for $Da=10^{-3}$ and $Ra_E=10^6$

Ra_I \ ε	**0,01**	***0,2***	***0,4***	***0,6***	***0,8***	***1***
0	7,62745	7,75490	8,02941	8,48039	8,75490	8,80392
10^3	7,62745	7,75490	8,01961	8,48039	8,75490	8,80392
10^4	7,61765	7,75490	8,01961	8,48039	8,75490	8,79412
10^5	7,47059	7,71569	8,12745	8,43137	8,70588	8,74510
10^6	7,14706	7,29412	7,68628	7,98039	8,26471	8,30392
10^7	3,71569	3,29412	3,73527	4,02941	4,23529	4,10784
10^8	-41,70588	-39,3235	-39,3333	-39,46078	-39,46078	-40,15686
10^9	-509,3726	-489,951	-484,451	-498,4314	-510,0981	-511,6373

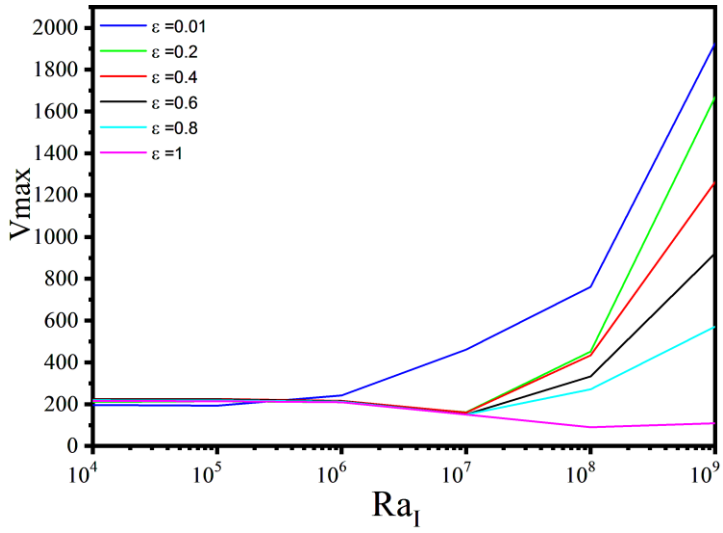

Figure IV.14: Evolution of the maximum velocity values as a function of internal Rayleigh number and porosity for $Ra_E=10^6$

IV.6 CONCLUSION

In this chapter, the focus was on investigating the heat transfer through natural convection in a square cavity subjected to differential heating. The cavity configuration includes a vertical porous layer and a uniform internal heat generation. The conservation equations of mass, momentum, and energy, which incorporate Brinkman and Forchheimer terms, were solved using the finite volume approach and the SIMPLER algorithm. Based on the ratio between the internal and external Rayleigh numbers (Ra_I/Ra_E), two distinct regimes were identified. For $Ra_I/Ra_E \leq 1$, the heat transfer is an increasing function of the external Rayleigh number. The direction of heat transfer is similar to the classical case of a differentially heated cavity, flowing from the hot wall to the cold wall. For $Ra_I/Ra_E>1$, the heat transfer is an increasing function of the internal Rayleigh number. Its direction is towards the outside of the cavity, occurring at both the hot and cold walls. In general, the presence of a porous layer with a low Darcy number or porosity value reduces heat transfer and increasing these two parameters progressively increases the heat reduction.

References

[1] Adjal S, Aklouche-benouaguef S, Zeghmati B., Natural convection in a partially porous cavity: Roads to chaos. *Numer. Heat Transf. A,* Vol. 74, Issue 8, (2018), pp. 1443-1467. https://doi.org/10.1080/10407782.2018.1525158

[2] Astanina M S, Sheremet M, Umavathi J C., Effect of thermal radiation on natural convection in a square porous cavity filled with a fluid of temperature-dependent viscosity. *Thermal Science,* Vol.22, Issue 1,(2018), pp.391 - 399. https://doi.org/10.2298/TSCI150722164A.

[3] Wu F, Lu D, Wang G (2016) Numerical analysis of natural convection in a porous cavity with the sinusoidal thermal boundary condition using a thermal nonequilibrium model. *Numer. Heat Transf. A,* Vol. 69, Issue 11, (2016), pp. 1280-1296. https://doi.org/10.1080/10407782.2015.1127025

[4] Dutta S, Pati S, Biswas AK., Thermal transport analysis for natural convection in a porous corrugated rhombic enclosure. *Heat Transf.*, Vol. 49, Issue6, (2020), pp. 3287-3313. https://doi.org/10.1002/htj.21774

[5] Astanina MS, Sheremet M, Umavathi JC., Transient natural convection with temperature-dependent viscosity in a square partially porous cavity having a heat-generating source.*Numer. Heat Transf. A,* Vol. 73, Issue 12, (2018), pp. 849-862. https://doi.org/10.1080/10407782.2018.1462007

[6] Meshram P, Bhardwaj S, Dalal A, Pati S., Effects of the inclination angle on natural convection heat transfer and entropy generation in a square porous enclosure. *Numer. Heat Transf. A*, Vol. 70, Issue 11, (2016), pp. 1271-1296. https://doi.org/10.1080/10407782.2016.1230433

[7] Aklouche-benouaguef S, Adjal S, Zeghmati B., Effect of Inclination and of Darcy Number on Bifurcations and Thermal Transfer in a Square Porous Cavity.*MATEC Web of Conferences,* Vol 307, Article Number01004, (2020), https://doi.org/10.1051/matecconf/202030701004

[8] Wu F, Zhou W, Ma X., Natural convection in a porous rectangular enclosure with sinusoidal temperature distributions on both side walls using a thermal non-equilibrium model. *International Journal of Heat and Mass Transfer,* Vol. 85, (2015), pp 756-771. https://doi.org/10.1016/J.IJHEATMASSTRANSFER.2015.02.039

[9] Rathnam V, Biswal P, Basak T., Analysis of entropy generation during natural convection within entrapped porous triangular cavities during hot or cold fluid disposal. *Numer. Heat Transf. A*, Vol. 69, Issue 9, (2016), pp. 931-956. https://doi.org/10.1080/10407782.2015.1109362

[10] Lukose L, Biswal P, Basak T., Analysis of process efficiency: Role of flow and thermal characteristics on entropy production and heat transfer rates for thermal convection in

porous beds confined within triangular configurations with hot slanted walls. *Numer. Heat Transf. A*, Vol. 81, Issue 7-12, (2022), pp. 160-186. https://doi.org/10.1080/10407782.2022.2063658

[11] Oueslati F., Ben-Beya B.,Lili T.,Numerical simulation of unsteady double-diffusive natural convection within an inclined parallelepipedic enclosure | *International Journal of Modern Physics C*. Vol. 25, No. 11, 1450058 (2014).https://www.worldscientific.com/doi/abs/10.1142/S0129183114500582.

[12] Al-Weheibi SM, Rahman MM., Convective heat transmission inside a porous trapezoidal enclosure occupied by nanofluids: local thermal nonequilibrium conditions for a porous medium. *TecnicaItaliana-Italian Journal of Engineering Science,* Vol. 61+1, No. 2, (2018), pp. 102-114. https://doi.org/10.18280/TI-IJES.620208

[13] Dutta S, Pati S, Baranyi L., Numerical analysis of magnetohydrodynamic natural convection in a nanofluid filled quadrantal enclosure. *Case Studies in Thermal Engineering,* Vol 28, (2021), 101507, https://doi.org/10.1016/j.csite.2021.101507

[14] Rihani C., Ben-Beya B., Three-dimensional natural convection of molten Lithium in a differentially heated rotating cubic cavityabout a vertical ridge - *ScienceDirect.PowderTechnology,* Vol 291, (2016), pp 97-109.

[15] Bhowmick D, Chakravarthy S, Randive P, Pati S., Numerical investigation on the effect of magnetic field on natural convection heat transfer from a pair of embedded cylinders within a porous enclosure, *Journal of Thermal Analysis and Calorimetry,* Vol 141, (2020), pp 2405–2427.https://doi.org/10.1007/s10973-020-09411-6

[16] Berrahil F, Benissaad S, Chérifa A, Médale M., Natural convection with volumetric heat generation and external magnetic field in differentially heated enclosure. *Proceedings of the Institution of Mechanical Engineers, Part C: Journal of Mechanical Engineering Science*Vol 228, Issue 15, (2014),pp 2711–2727. https://doi.org/10.1177/0954406214521792

[17] Hamimid S, Guellal M., Numerical analysis of combined natural convection-internal heat generation source-surface radiation. *Thermal Science,*Vol 20, (2016),pp 1879–1889.

[18] Rachedi N, Bouafia M, Guellal M, Hamimid S., Effect of radiation on the flow structure and heat transfer in a 2-D gray medium. *Thermal Science, Vol*23, (2019), pp 3603–3614. https://doi.org/10.2298/TSCI180108117R

[19] Hdhiri N, Souayeh B, Alfannakh H, Ben Beya B., Natural Convection Study with Internal Heat Generation on Heat Transfer and Fluid Flow Within a Differentially Heated Square Cavity Filled with Different Working Fluids and Porous Media, *Bio Nano Science,* Vol 9, (2019), pp 702–722.

[20] Hamimid S, Guellal M, Amroune A, Zeraibi N., Effect of a Porous Layer on the Flow Structure and Heat Transfer in a Square Cavity. *Fluid Dynamics & Materials Processing*, Vol 8, (2012), pp 69-90. https://doi.org/10.3970/fdmp.2011.008.069

[21] Brinkman HC, On the permeability of media consisting of closely packed porous particles. *Flow, Turbulence and Combustion*, Vol 1, (1949), pp 81–86. https://doi.org/10.1007/BF02120318

[22] Sobamowo MG, Kamiyo OM, Adeleye OA., Thermal performance analysis of a natural convection porous fin with temperature-dependent thermal conductivity and internal heat generation. *Thermal Science and Engineering Progress*Vol 1, (2017),pp 39–52. https://doi.org/10.1016/j.tsep.2017.02.007

[23] Rashad AM, Armaghani T, Chamkha AJ, Mansour MA., Entropy generation and MHD natural convection of a nanofluid in an inclined square porous cavity: Effects of a heat sink and source size and location. *Chinese Journal of Physics,*Vol 56,(2018),pp 193–211. https://doi.org/10.1016/j.cjph.2017.11.026

[24] Chakravarty A, Datta P, Ghosh K, et al., Mixed convective heat transfer in an enclosure containing a heat-generating porous bed under the influence of bottom injection. *International Journal of Heat and Mass Transfer,*Vol 117,(2018), pp 645–657. https://doi.org/10.1016/j.ijheatmasstransfer.2017.10.046

[25] Aminossadati SM, Ghasemi B., Natural convection cooling of a localised heat source at the bottom of a nanofluid-filled enclosure. *European Journal of Mechanics - B/Fluids*Vol 28, (2009), pp 630–640. https://doi.org/10.1016/j.euromechflu.2009.05.006

[25] De Vahl Davis G, Jones IP., Natural convection in a square cavity: A comparisonexercise. *Int JNumer Meth Fluids,*Vol 3, (1983), pp 227–248. https://doi.org/10.1002/fld.1650030304

V.1 INTRODUCTION

The study of heat transfer by natural convection in porous media is an area of research that holds significant importance in various fields, such as geothermal energy, environmental restoration, and heat insulation. Several recent studies [1-4] have focused on understanding the interplay between natural convection and porous media, emphasizing the crucial role of the properties of the porous medium. Enhancing heat transfer in cavities using porous materials has garnered considerable attention, with factors such as permeability, porosity, and the thickness of the porous layer identified as key influencers of convective heat transfer [5-7]. By manipulating these parameters, it is possible to achieve improved thermal management, enhanced energy efficiency, and overall system performance

Earlier research has examined various aspects of natural convection in porous media. For instance, Hamimid et al. [8] conducted an analysis of buoyancy-driven convection within a square cavity containing a porous layer saturated by a binary fluid. Yan et al. [9] focused on the migration of a dense salt plume affected by high-permeability inclusions. By emphasizing the disparity between gas and water permeability, Tanikawa et al. [10] highlighted its significance in understanding fluid flow dynamics. Additionally, Tan et al. [11] developed predictive models for both permeability and porosity in porous media. Civan [12] made valuable contributions by exploring variations in porosity and permeability through fractal properties. Habbachi et al. [13] investigated natural convection heat transfer within a cubic enclosure featuring a central porous medium. In contrast, Ouarhlent et al. [14] studied heat transfer in a cubic chamber partially filled with porous material. The work of Lee et al. [15] focused on electrode performance in fuel cells, while Gao et al. [16] extensively studied transport phenomena in porous media. Lastly, Kan et al. [17] analyzed the effects of porosity on laminar flow and drag reduction.

While heat transfer in porous media has significant industrial applications, there is a research gap concerning natural convection in a porous medium filled with a compressible gas at low Mach numbers. This chapter aims to address this gap by examining the impact of porous media properties on the thermal and dynamic characteristics of natural convection in such a gas, with a specific focus on the low Mach number model. To accurately simulate fluid dynamics at velocities much lower than the speed of sound, the low Mach number approximation method is employed. This approach allows for a comprehensive understanding of the phenomenon.

This chapter investigates variations in thermophysical properties, such as thermal viscosity and conductivity, which are temperature-dependent. By considering these factors collectively, the study aims to establish a comprehensive understanding of the interplay between porous media properties and compressible gas behavior, specifically concerning the thermal and dynamic characteristics of the system.

The uniqueness of this study lies in integrating multiple parameters, including porous media properties, compressible gas behavior, and the use of the low Mach number approximation, inside a square cavity with defined boundary conditions. The study examines how porous media properties influence fluid motion, heat transfer, and the Nusselt number,

which serves as a metric for assessing heat transfer rates in both fluids and porous media. This comprehensive examination aims to improve the understanding of natural convection in porous materials with compressible fluids, while exploring its potential applications in various fields.

V.2 MATHEMATICAL FORMULATION

The system under study is a two-dimensional square cavity of dimension H. The enclosure contains a Newtonian fluid with variable properties, including density ρ, molecular viscosity μ, thermal conductivity k, and temperature T. Positioned at the bottom of the cavity is a fluid-saturated porous layer with finite thickness. The porous medium is fully saturated with fluid and is assumed to exhibit macroscopic isotropy, homogeneity, and local thermal equilibrium. The temperatures of the vertical surfaces are maintained at T_H and T_C (T_H>T_C), resulting in laminar free convection within the cavity. Given the lack of any influence from the horizontal walls, it can be postulated that these surfaces exhibit adiabatic characteristics. The enclosure's four walls adhere to boundary conditions of no-slip and zero-mass flux. The initial conditions include constant distributions of reference pressure P_0 and temperature $T_0 = (T_H + T_C)/2$, as well as a stationary flow with $V=0$.

Figure V.1 shows the boundary conditions, coordinate system, and the combined fluid/porous system relevant to the investigation.

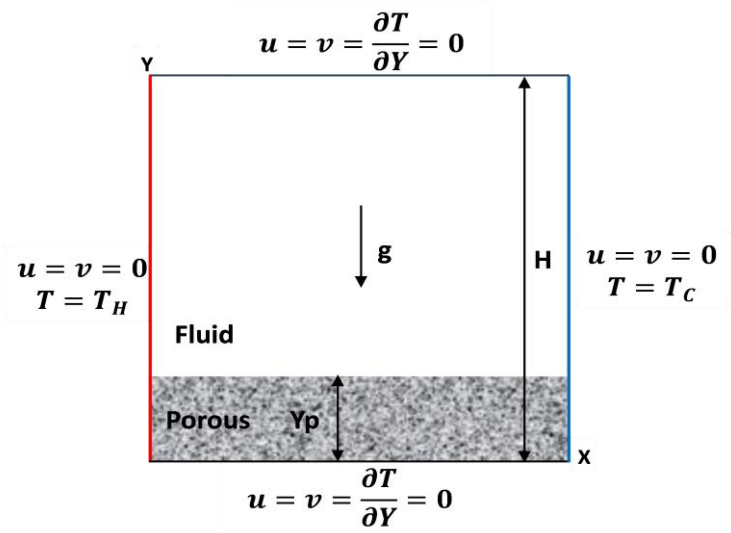

Figure V.1: Physical geometry and associated boundary conditions

To accurately capture significant temperature variations within the differentially heated cavity, a low Mach number flow model is used [18-20]

The use of low Mach number (LMN) models allows for the precise representation of these variations, overcoming the limitations associated with the Boussinesq assumption. Moreover, these models maintain the characteristic pressure-density decoupling observed in incompressible flows.

Under the given conditions, the Navier-Stokes equations are expanded in a series using a small parameter M^2, where M represents the Mach number. The total pressure p is further decomposed into the mean thermodynamic pressure $\bar{p}$ and the dynamic pressure p'.

The following equations represent the dimensional governing equations for the system:

Fluid region:

$$\frac{\partial \rho}{\partial t} + \frac{\partial \rho u}{\partial x} + \frac{\partial \rho v}{\partial y} = 0 \tag{V.1}$$

$$\rho\left(\frac{\partial u}{\partial t} + u\frac{\partial u}{\partial x} + v\frac{\partial u}{\partial y}\right) = -\frac{\partial \acute{p}}{\partial x} + \left[\frac{\partial}{\partial x}\left(\mu\frac{\partial u}{\partial x}\right) + \frac{\partial}{\partial y}\left(\mu\frac{\partial u}{\partial y}\right)\right] + \frac{1}{3}\left(\mu\frac{\partial^2 u}{\partial x^2} + \mu\frac{\partial^2 u}{\partial y^2}\right) \tag{V.2}$$

$$\rho\left(\frac{\partial v}{\partial t} + u\frac{\partial v}{\partial x} + v\frac{\partial v}{\partial y}\right) = -g(\rho - \rho_0) - \frac{\partial \acute{p}}{\partial y} + \left[\frac{\partial}{\partial x}\left(\mu\frac{\partial v}{\partial x}\right) + \frac{\partial}{\partial y}\left(\mu\frac{\partial v}{\partial y}\right)\right] + \frac{1}{3}\left(\mu\frac{\partial^2 v}{\partial x^2} + \mu\frac{\partial^2 v}{\partial y^2}\right) \tag{V.3}$$

$$\rho C_p\left(\frac{\partial T}{\partial t} + u\frac{\partial T}{\partial x} + v\frac{\partial T}{\partial y}\right) = \frac{\partial}{\partial x}\left(k\frac{\partial T}{\partial x}\right) + \frac{\partial}{\partial y}\left(k\frac{\partial T}{\partial y}\right) + \frac{d\bar{p}}{dt} \tag{V.4}$$

$$\bar{p} = \rho RT \tag{V.5}$$

Porous region:

$$\frac{\partial \rho}{\partial t} + \frac{\partial \rho u}{\partial x} + \frac{\partial \rho v}{\partial y} = 0 \tag{V.6}$$

$$\rho\left(\frac{1}{\varepsilon}\frac{\partial u}{\partial t} + \frac{1}{\varepsilon^2}u\frac{\partial u}{\partial x} + \frac{1}{\varepsilon^2}v\frac{\partial u}{\partial y}\right) = -\frac{\partial p'}{\partial x} + \frac{1}{\varepsilon}\left[\frac{\partial}{\partial x}\left(\mu\frac{\partial u}{\partial x}\right) + \frac{\partial}{\partial y}\left(\mu\frac{\partial u}{\partial y}\right) + \frac{1}{3}\Delta\mu\Delta\vec{V}\right] - D_x \tag{V.7}$$

$$\rho\left(\frac{1}{\varepsilon}\frac{\partial v}{\partial t} + \frac{1}{\varepsilon^2}u\frac{\partial v}{\partial x} + \frac{1}{\varepsilon^2}v\frac{\partial v}{\partial y}\right) = -\frac{\partial p'}{\partial y} + \frac{1}{\varepsilon}\left[\frac{\partial}{\partial x}\left(\mu\frac{\partial v}{\partial x}\right) + \frac{\partial}{\partial y}\left(\mu\frac{\partial v}{\partial y}\right) + \frac{1}{3}\Delta\mu\Delta\vec{V}\right] - g(\rho - \rho_0) - D_y \tag{V.8}$$

$$(\rho Cp)_{eff}\left(\frac{\partial T}{\partial t}\right) + (\rho Cp)_f\left[u\frac{\partial T}{\partial x} + v\frac{\partial T}{\partial y}\right] = \frac{\partial}{\partial x}k\frac{\partial T}{\partial x} + \frac{\partial}{\partial y}k\frac{\partial T}{\partial y} + \frac{d\bar{p}}{dt} \tag{V.9}$$

$$\left(\rho C_p\right)_{eff} = \varepsilon.\left(\rho C_p\right)_f + (1-\varepsilon)\left(\rho C_p\right)_s \tag{V.10}$$

$$\bar{p} = \rho RT \tag{V.11}$$

The parameters D_x and D_y in the momentum equations correspond to the drag forces per unit volume of the porous medium along the x and y directions, respectively.

In the case of one-dimensional flow with velocity V, the drag expression is based on various correlations for packed and fluidized beds, such as the well-known Ergun's (1952) correlation. For a two-dimensional flow, the contribution of the solid matrix drag can be mathematically expressed as follows:

$$D_x = \frac{\mu_f}{K}u + \frac{1.75}{\sqrt{150}}\frac{\rho_f}{\sqrt{K}}\frac{|\vec{V}|}{\varepsilon^{3/2}}u \tag{V.12}$$

$$D_y = \frac{\mu_f}{K}v + \frac{1.75}{\sqrt{150}}\frac{\rho_f}{\sqrt{K}}\frac{|\vec{V}|}{\varepsilon^{3/2}}v \tag{V.13}$$

Where: $|\vec{V}| = \sqrt{u^2 + v^2}$

The walls of the system adhere to non-slip boundary conditions, which leads to the following expressions for the boundary and initial conditions:

$u = v = T = 0$, at $t = 0$

$u = v = 0, T = T_H$ for $0 \le y \le H$ and $x = 0$

$u = v = 0, T = T_C$ for $0 \le y \le H$ and $x = H$

$u = v = 0,\ \frac{\partial T}{\partial y} = 0$ for $0 \le x \le H$ and $y = 0$

$u = v = 0,\ \frac{\partial T}{\partial y} = 0$ for $0 \le x \le H$ and $y = H$

The governing equations are supplemented by Sutherland's law for the temperature dependence of transport properties, μ and k:

$$\frac{\mu(T)}{\mu_0} = \left(\frac{T}{T_0}\right)^{3/2}\frac{T_0 + S_\mu}{T + S_\mu} \quad \text{and} \quad k(T) = \mu(T)\frac{Cp_0 k_0}{\nu_0}$$

Where $S_\mu = 110.5\ K$

Depending on the case studied, it is assumed that these properties either vary with temperature or remain constant.

The equations of momentum in the porous region can be expressed as:

$$\rho\left(\frac{1}{\varepsilon}\frac{\partial u}{\partial t} + \frac{1}{\varepsilon^2}u\frac{\partial u}{\partial x} + \frac{1}{\varepsilon^2}v\frac{\partial u}{\partial y}\right) = -\frac{\partial p'}{\partial x} + \frac{1}{\varepsilon}\left[\frac{\partial}{\partial x}\left(\mu\frac{\partial u}{\partial x}\right) + \frac{\partial}{\partial y}\left(\mu\frac{\partial u}{\partial y}\right) + \frac{1}{3}\Delta\mu\Delta\vec{V}\right]$$

$$-\mu\frac{u}{K} - \frac{1.75\rho}{\sqrt{150K}}\frac{|\vec{V}|}{\varepsilon^{3/2}}u \tag{V.14}$$

$$\rho\left(\frac{1}{\varepsilon}\frac{\partial v}{\partial t} + \frac{1}{\varepsilon^2}u\frac{\partial v}{\partial x} + \frac{1}{\varepsilon^2}v\frac{\partial v}{\partial y}\right) = -\frac{\partial p'}{\partial y} + \frac{1}{\varepsilon}\left[\frac{\partial}{\partial x}\left(\mu\frac{\partial v}{\partial x}\right) + \frac{\partial}{\partial y}\left(\mu\frac{\partial v}{\partial y}\right) + \frac{1}{3}\Delta\mu\Delta\vec{V}\right] - g(\rho - \rho_0)$$

$$-\mu\frac{v}{K} - \frac{1.75\rho}{\sqrt{150K}}\frac{|\vec{V}|}{\varepsilon^{3/2}}v \tag{V.15}$$

To make the conservation equations (V.1-V.6, V.9-V.11, V.14, and V.15) dimensionless, the following dimensionless parameters are used

$$\boldsymbol{\tau = \frac{\alpha t}{H^2}},\ \boldsymbol{X = \frac{x}{H}},\ \boldsymbol{Y = \frac{y}{H}},\ \boldsymbol{U = \frac{uH}{\alpha}}, \boldsymbol{V = \frac{vH}{\alpha}},\ \boldsymbol{\pi = \frac{\varepsilon^2 p' H^2}{\rho \alpha^2}},\ \boldsymbol{\bar{P} = \frac{\bar{p}}{p_0}},\ \boldsymbol{\theta = \frac{T - T_0}{\Delta T}},$$

Where: $\boldsymbol{\Delta T = T_H - T_C}$, $\boldsymbol{T_0 = \frac{T_H + T_C}{2}}$, $\boldsymbol{\varepsilon_b = \frac{\Delta T}{2T_0}}$

The governing equations are transformed into their dimensionless form, as shown below

Fluid region:

$$\frac{\partial \rho^*}{\partial \tau} + \frac{\partial \rho^* U}{\partial X} + \frac{\partial \rho^* V}{\partial Y} = 0 \tag{V.13}$$

$$\rho^* \left(\frac{\partial U}{\partial \tau} + U \frac{\partial U}{\partial X} + V \frac{\partial U}{\partial Y}\right) = -\frac{\partial \pi}{\partial X} + Pr \left[\frac{\partial}{\partial X}\left(\mu^* \frac{\partial U}{\partial X}\right) + \frac{\partial}{\partial Y}\left(\mu^* \frac{\partial U}{\partial Y}\right) + \frac{1}{3} \nabla \mu^* \nabla . \vec{V}\right] \tag{V.14}$$

$$\rho^* \left(\frac{\partial V}{\partial \tau} + U \frac{\partial V}{\partial X} + V \frac{\partial V}{\partial Y}\right) = -\frac{\partial \pi}{\partial Y} - RaPr \frac{\rho^* - 1}{2\epsilon_b} + Pr \left[\frac{\partial}{\partial X}\left(\mu^* \frac{\partial V}{\partial X}\right) + \frac{\partial}{\partial Y}\left(\mu^* \frac{\partial V}{\partial Y}\right) + \frac{1}{3} \nabla \mu^* \nabla . \vec{V}\right] \tag{V.15}$$

$$\rho^* \left(\frac{\partial \theta}{\partial \tau} + U \frac{\partial \theta}{\partial X} + V \frac{\partial \theta}{\partial Y}\right) = \frac{\partial}{\partial X}\left(k^* \frac{\partial \theta}{\partial X}\right) + \frac{\partial}{\partial Y}\left(k^* \frac{\partial \theta}{\partial Y}\right) + \frac{\gamma - 1}{2\varepsilon_b \gamma} \frac{d\bar{P}}{d\tau} \tag{V.16}$$

$$\rho^* = \frac{\bar{P}}{(2\varepsilon_b \theta + 1)} \tag{V.17}$$

Porous region:

$$\frac{\partial \rho^*}{\partial \tau} + \frac{\partial \rho^* U}{\partial X} + \frac{\partial \rho^* V}{\partial Y} = 0 \tag{V.18}$$

$$\rho^* \left(\frac{1}{\varepsilon}\frac{\partial U}{\partial \tau} + \frac{1}{\varepsilon^2} U \frac{\partial U}{\partial X} + \frac{1}{\varepsilon^2} V \frac{\partial U}{\partial Y}\right) = -\frac{1}{\varepsilon^2}\frac{\partial \pi}{\partial X} + \frac{1}{\varepsilon} Pr \left[\frac{\partial}{\partial X}\left(\mu^* \frac{\partial U}{\partial X}\right) + \frac{\partial}{\partial Y}\left(\mu^* \frac{\partial U}{\partial Y}\right) + \frac{1}{3} \nabla \mu^* \nabla . \vec{V}\right] - \frac{Pr}{Da} U - \frac{1.75}{\sqrt{150\ Da}} \frac{|\vec{V}|}{\varepsilon^{3/2}} U \tag{V.19}$$

$$\rho^* \left(\frac{1}{\varepsilon}\frac{\partial V}{\partial \tau} + \frac{1}{\varepsilon^2} U \frac{\partial V}{\partial X} + \frac{1}{\varepsilon^2} V \frac{\partial V}{\partial Y}\right) = \frac{1}{\varepsilon^2}\frac{\partial \pi}{\partial Y} + \frac{1}{\varepsilon} Pr \left[\frac{\partial}{\partial X}\left(\mu^* \frac{\partial V}{\partial X}\right) + \frac{\partial}{\partial Y}\left(\mu^* \frac{\partial V}{\partial Y}\right) + \frac{1}{3} \nabla \mu^* \nabla . \vec{V}\right] - RaPr \frac{\rho^* - 1}{2\epsilon_b} - \frac{Pr}{Da} V - \frac{1.75}{\sqrt{150\ Da}} \frac{|\vec{V}|}{\varepsilon^{3/2}} V \tag{V.20}$$

$$\sigma \frac{\partial \theta}{\partial \tau} + U \frac{\partial \theta}{\partial X} + V \frac{\partial \theta}{\partial Y} = \frac{\partial}{\partial X}\left(k^* \frac{\partial \theta}{\partial X}\right) + \frac{\partial}{\partial Y}\left(k^* \frac{\partial \theta}{\partial Y}\right) + \frac{\gamma - 1}{2\varepsilon_b \gamma} \frac{d\bar{P}}{d\tau} \tag{V.21}$$

$$\rho^* = \frac{\bar{P}}{(2\varepsilon_b \theta + 1)} \tag{V.22}$$

With:

$$\sigma = \frac{\varepsilon(\rho Cp)_f + (1 - \varepsilon)(\rho Cp)_s}{(\rho Cp)_f} \tag{V.23}$$

The governing equations for the cavity flow and heat transfer are influenced by dimensionless numbers that play a crucial role. These dimensionless numbers are defined as follows:

$Da = K/H^2$ Darcy number
$Pr = \nu/\alpha$ Prandtl number
$Ra = g\beta\Delta T H^3/\nu\alpha$ Rayleigh number

The corresponding dimensionless boundary conditions are:

$U = V = 0, \theta = \theta_H$ for $0 \leq Y \leq 1$ and $X = 0$

$U = V = 0, \theta = \theta_C$ for $0 \leq Y \leq 1$ and $X = 1$

$U = V = 0, \frac{\partial\theta}{\partial Y} = 0$ for $0 \leq X \leq 1$ and $Y = 0$

$U = V = 0, \frac{\partial\theta}{\partial Y} = 0$ for $0 \leq X \leq 1$ and $Y = 1$

The dimensionless transport coefficients $\mu^*(\theta)$ and $k^*(\theta)$ are given, respectively, by:

$$\mu^*(\theta) = (2\varepsilon_b\theta + 1)^{3/1}\frac{1+S_\mu/T_0}{2\varepsilon_b\theta+1+S_\mu/T_0} \quad \text{and} \quad k^*(\theta) = \frac{\mu^*(\theta)}{Pr}$$

V.3 NUMERICAL MODELLING

The governing differential equations for velocity, pressure, and temperature fields in two dimensions are solved numerically using a finite volume technique. Advection-diffusion terms are approximated using a power scheme (refer to chapter three). To handle the pressure-velocity coupling, the SIMPLER (Semi-Implicit Method for Pressure Linked Equations Revised) method with a staggered grid, as detailed in Patankar [18], is employed. The equations are formulated for transient analysis, and an entirely implicit transient differencing scheme is used iteratively until convergence to a steady state is achieved. The algebraic equations are solved using a combination of the line-by-line method, which includes both direct (Thomas algorithm) and iterative (Gauss-Seidel) methods. This approach involves solving the discretized equations with two directional sweeps.

V.4 GRID SENSITIVITY

To optimize the trade-off between accuracy and computation time, a mesh sensitivity test was conducted in a domain with varying grid sizes, ranging from (80×80) to (260×260). The test compared the average Nusselt numbers on the hot wall in steady state (Table V.1). The configuration under consideration is defined by the following computational parameters: Ra=10^6, Yp=0.2, ε=0.4, Da=10^{-5}, ΔT=360 K. Initially, the medium is at rest and has a uniform temperature of T0=300K, with a corresponding Prandtl number of 0.71.

Figure V.2a presents the results obtained for different grid resolutions. It is observed that as the mesh becomes finer, the average Nusselt values decrease. For grid sizes ranging from (160×160) to (260×260), the results yield similar values, indicating that the solution becomes independent of the mesh beyond (160×160). Therefore, (160×160) is considered the optimal compromise between accuracy and computation time, and it is used to validate the code. Figure V.2b illustrates the mesh model diagram. The number of meshes is 25600.

Table V.1: Average Nusselt number for different mesh sizes

	80×80	***100×100***	***120×120***	***140×140***	***160×160***	***240×240***	***260×260***
Nu_H	7,1572	7,1091	7,0826	7,0652	7,05299	7,0535	7,05329
$\Delta Nu_H(\%)$	0,67	0,37	0,25	0,17	0,01	0,003	/
Nu_C	7,1112	7,075	7,04312	7,01976	7,0012	6,9981	6,99619
$\Delta Nu_C(\%)$	0,51	0,45	0,33	0,26	0,04	0,03	/

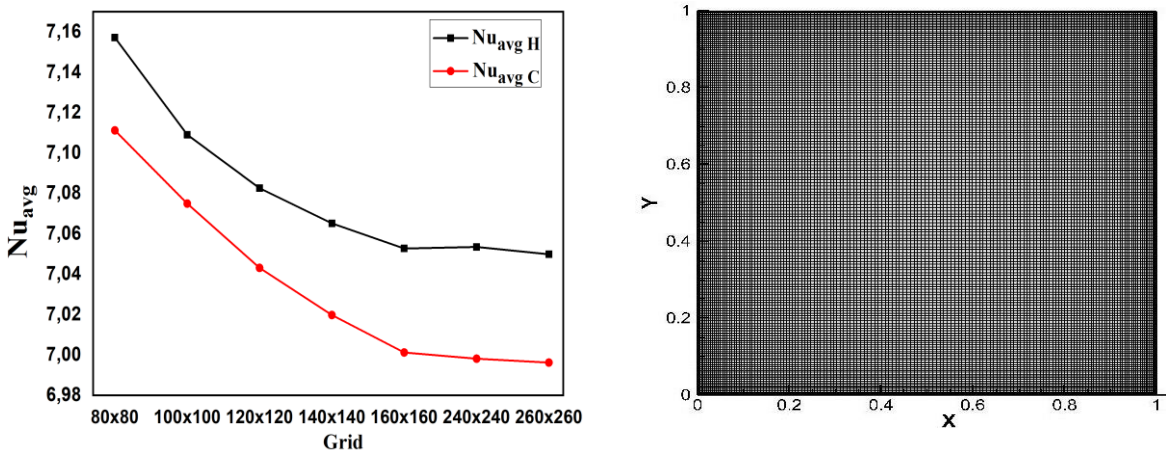

(a) **(b)**

Figure V.2: Mesh sensitivity test (a) Evolution of average Nusselt numbers for different grid values (b) Mesh diagram

V.5 VALIDATION TESTS

The code utilized in this study underwent verification by comparing our findings with those of previous studies [13,14] and [21]. Figure V.3 illustrates the temperature distribution at mid-height (Y=0.5). To ensure the validity of our research, we replicated the conditions of the modeling setup described in Habbachi et al. [13], specifically by setting Yp=Xp at the center of the cavity. This allowed us to compare our results with theirs by examining different thicknesses of the porous layer (Yp), with $Ra=10^5$ and $Da=10^{-6}$. To ensure the code was working correctly, we used a Boussinesq code to predict how porous materials interact with natural convection. Our numerical results aligned well with the previous findings reported by Habbachi et al.

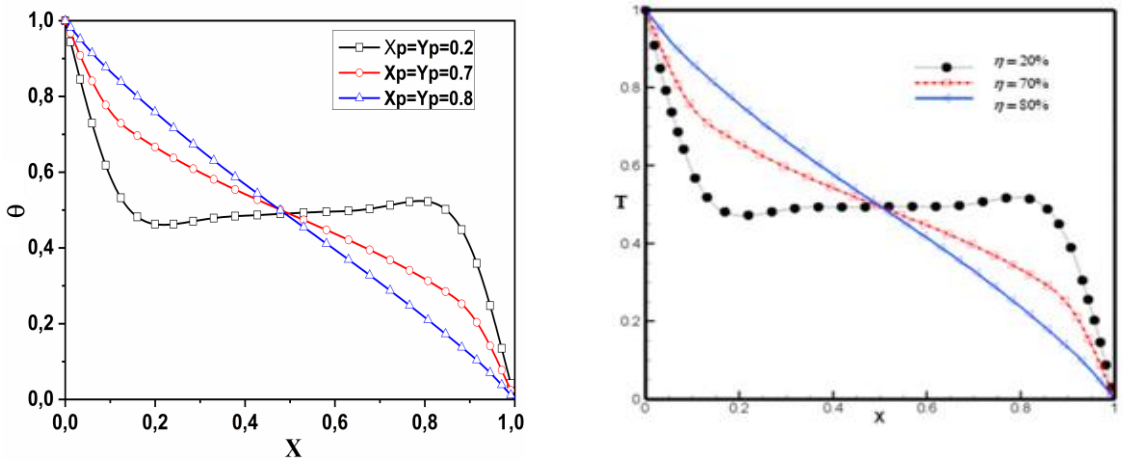

Present work Habbachi et al.

Figure V.3: Temperature profiles for Ra=10^5, ε=0.2, Da=10^{-6}, and various values of dimensionless thickness of the porous layer in a vertical median plan (Y=0.5).

Figure V.4 depicts the average Nusselt number distribution across various Rayleigh numbers. Consistent with the methodology outlined by Ouarhlent et al. [14], comparable configurations were employed, featuring a square-shaped porous layer (where Xp=Yp) positioned at the center of the enclosure. This setup allowed for a comparative analysis between our results and those of Ouarhlent et al. across different porous layer thicknesses (Yp or η) and for Da=10^{-6}. Notably, the parameter η, chosen at 20%, 50%, and 80% in the investigation conducted by Ouarhlent et al., represents the dimension Yp of the square porous layer as a percentage of the cavity's unit dimension. To assess the interaction between porous media and natural convection, the code was validated using the Boussinesq model. The numerical results from this investigation align with those previously reported by Ouarhlent et al. [14].

The conclusions drawn are supported by the findings presented in Table V.2, which indicate minimal relative differences. Specifically, a marginal variance of 0.2% is noted for Ra=10^6, while average differences of 2.43%, 3.04%, and 6.04% are recorded for Yp values of 0.2, 0.5, and 0.8, respectively.

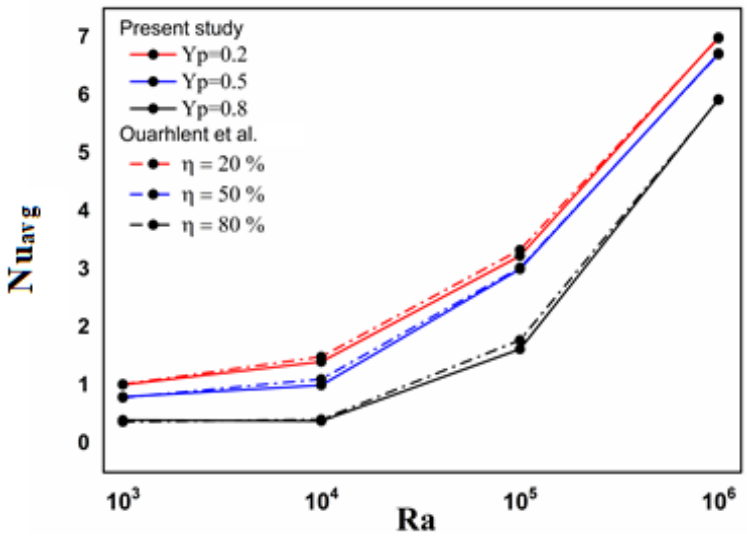

Figure V.4: Variation of average Nusselt numbers with different Rayleigh numbers and for Da=10^{-6} (Comparative analysis)

Table V.2: Relative difference in Nusselt numbers between our investigation and the findings of Ouarhlent et al. [14]

Yp / Ra	*0.2*	*0.5*	*0.8*
10^3	0,77	1,77	8,47
10^4	5,62	9,39	6,79
10^5	3,12	0,75	8,71
10^6	0,20	0,24	0,20
Average deviations	2,43	3,04	6,04

Additionally, validation of the non-Boussinesq code was performed against a benchmark solution representing convection in a partially heated square cavity without a porous material. Tests were conducted for both constant and variable characteristics, focusing on a significant temperature difference (ε_b=0.6) at Ra=10^6, with a reference temperature of T_0=300 K. The results, as presented in Table V.3, demonstrated excellent agreement with the findings reported by P. Quéré et al.[21], particularly regarding the average Nusselt number.

Table V.3: Comparative analysis between the average Nusselt numbers in this study and those reported by Le Quéré et al. [21]

	Constant properties		**Variable properties**	
	Le Quéré	Present work	Le Quéré	Present work
$\mathbf{Nu_H}$	8.85978	8.854992	8.6866	8.679508
$\mathbf{Nu_C}$	8.85978	8.863162	8.6866	8.700842
$\overline{\mathbf{P}}$	0.856338	0.85576	0.924487	0.923238

Overall, the code used in this study was validated by comparing our results with those of previous studies [13,14] and [21]. The verification process involved replicating physical configurations, employing Boussinesq and non-Boussinesq codes, and evaluating the consistency of our findings with established benchmarks and reference data.

V.6 RESULTS AND DISCUSSIONS

V.6.1 Impact of constant and variable thermophysical properties under large temperature differences

This section employs the low Mach number code to examine the influence of the Boussinesq parameter (ε_b) on heat transfer and fluid dynamics in the presence of a horizontal porous layer at the bottom of the cavity. Two cases are compared: one featuring constant temperature-dependent fluid characteristics and the other with variable properties following Sutherland's law.

The simulation parameters are set as follows: Pr = 0.71, $Ra=10^6$, T_0 = 300 K, $Da=10^{-5}$, Yp=0.2 and ε=0.4. To examine the impact of the Boussinesq parameter, different values ranging from ε_b = 0.017 to 0.6 are considered. In the Boussinesq solution, the temperature difference (ΔT) is set to 10 K. It should be noted that in previous works, it was demonstrated that, under the condition $\varepsilon b \leq 0.05$, corresponding to a temperature difference $\Delta T \leq 30°C$, the incompressible model using the Boussinesq approximation can be applied to simulate both pure natural convection and combined natural convection with surface radiation [22, 23].

Figures V.5-V.11 provide an opportunity for two simultaneous comparisons. They present the results obtained for three cases: Boussinesq (ε_b = 0.017), weak non-Boussinesq (ε_b = 0.3), and strong non-Boussinesq (ε_b = 0.6) at $Ra = 10^6$. These simulations are conducted in the presence of a porous layer with a porosity of ε = 0.4 and low permeability characterized by the Darcy number $Da = 10^{-5}$, with a dimensionless thickness of Yp = 0.2. The main goal is to explore the impact of the Boussinesq parameter on flow and heat transfer phenomena. Additionally, these figures enable a comparison of the results achieved with constant versus variable fluid properties. This analysis allows us to examine how fluid properties affect both flow and heat transfer.

Figure V.5 illustrates how the parameter ε_b influences the flow by presenting the vertical and horizontal velocity profiles at Y=0.5 and X=0.5, respectively. The U component profiles show that, in contrast to the scenario with a low εb value (ε_b=0.017), the boundary layer contracts near the lower wall due to the presence of the porous layer (Yp=0.2) and expands near the opposite wall. The V component profiles along the vertical sides exhibit a similar pattern, albeit with varying ratios. It is worth noting that the flow for the V component remains unchanged in the stratification zone, while the peak at the cold vertical wall is significantly larger for ε_b=0.6 compared to ε_b=0. 017. Additionally, there is a distinction in the maximum value of the V component within the boundary layer between constant and variable fluid properties, despite the porous layer being located at the bottom of the cavity. However, for the U component, this difference is more pronounced throughout the entire enclosure, except for the region occupied by the porous layer, where the flow remains stagnant due to the low permeability and porosity of the porous material.

Figure V.6 displays the horizontal and vertical fluid temperature profiles. At ε_b=0.6, the thermal boundary layer thickens near the hot wall and thins near the cold wall, causing a shift of the temperature peaks towards the cold wall. This behavior is solely attributed to non-Boussinesq factors.

As ε_b increases for the variable properties, the fluid within the central region becomes hotter, leading to a reduction in stratification. The vertical temperature profile is impacted by the existance of the porous layer at the cavity's base.

The porous layer significantly influences the vertical temperature profile, with the most pronounced effect depending on factors such as the variation of fluid characteristics with temperature and the high value of ε_b.

Figure V.7 illustrates the temperature distribution on the horizontal walls. For small values of ε_b, the presence of a porous layer is observed to result in a slight reduction in temperature profiles on the bottom wall (Y = 0). In this region, the impact of fluid properties on heat exchange is relatively minimal. However, on the upper wall, the effects of fluid properties become more pronounced. When comparing the cases of constant properties (CP) and variable properties (VP) for ε_b = 0.6, a notable difference in temperature distribution is observed. The utilization of variable properties greatly enhances thermal transfer at the upper wall. It is important to note that the temperature distribution on the horizontal walls is higher when considering variable properties compared to constant properties, especially in the presence of large temperature differences.

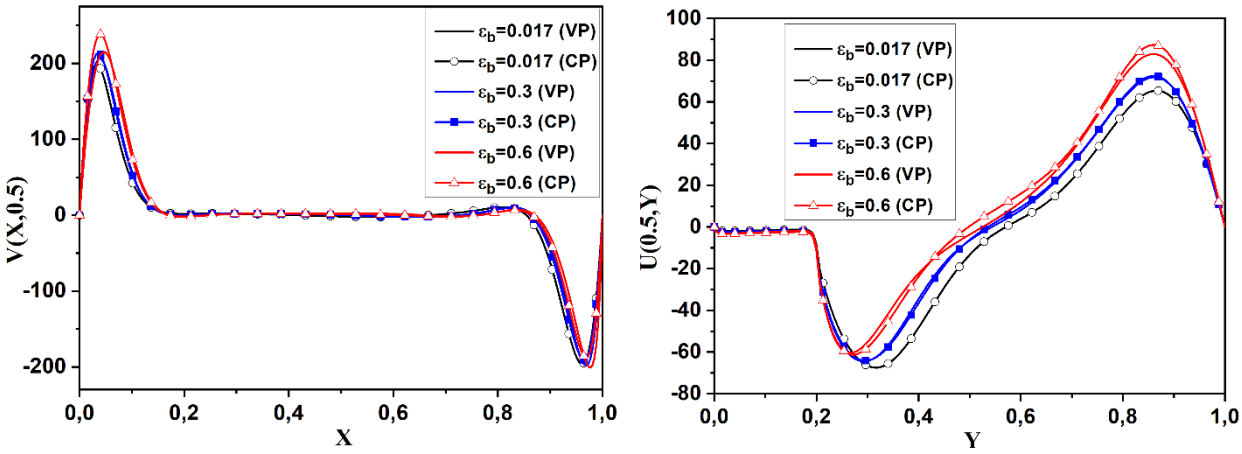

(a) (b)

Figure V.5: Vertical (a) and horizontal (b) velocities for Ra=10^6, Da=10^{-5}, Yp=0.2, ε = 0.4 and different values of ε_b

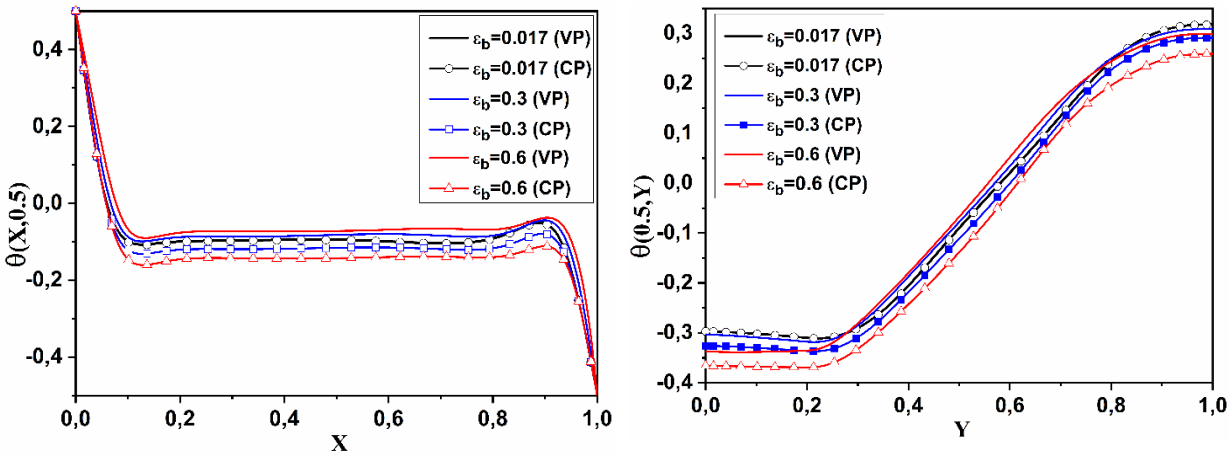

(a) (b)

Figure V.6: Cross-section of horizontal (a) and vertical (b) temperature profiles for $Ra=10^6$, $Da=10^{-5}$, Yp=0.2, ε = 0.4 and different values of ε_b

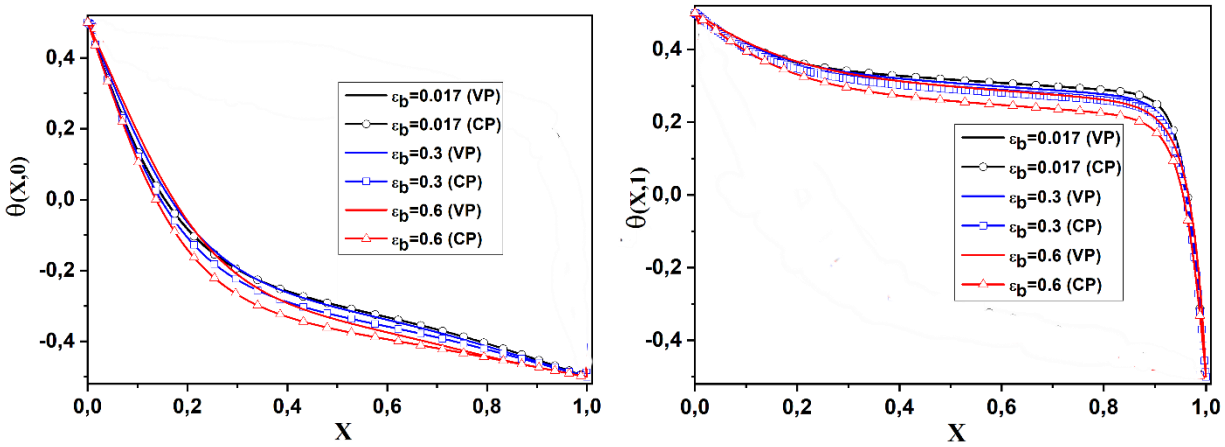

(a) (b)

Figure V.7: Distributions of lower (a) and upper (b) wall temperatures for $Ra=10^6$, $Da=10^{-5}$, Yp=0.2, ε = 0.4 and different values of ε_b.

Figure V.8 illustrates the streamlines, isotherms, pressure, and density profiles. In general, when the temperature difference is small (ε_b = 0.017), there are no significant variations between the solutions for variable and constant properties and all profiles exhibit a symmetrical structure relative to the core region of the cavity. The isotherms on the horizontal sidewalls indicate the presence of temperature gradients towards the bottom wall. Additionally, due to the low permeability and porosity of the porous layer, there is a moderate flow in the vicinity of the porous layer along the streamlines. As ε_b increases to 0.3, the flow intensifies, resulting in the loss of symmetry in the streamlines, isotherms, pressure, and density contours. When the temperature difference becomes large (ε_b = 0.6), the symmetry of the flow is completely disrupted.

Figure V.9 also demonstrates the effect of fluid properties on heat transfer and flow. In both the boundary layers and the core cavity, the temperature rises notably. The impact of fluid properties and the porous layer on streamlines and pressure is most noticeable near the cavity's bottom wall, in the middle, and close to the top. It is important to note that, whether the properties are constant or variable, the boundary layers near the hot wall maintain a thicker profile, indicating that the primary cause of this phenomenon is the nonlinear variation of density, especially for $\varepsilon_b = 0.6$.

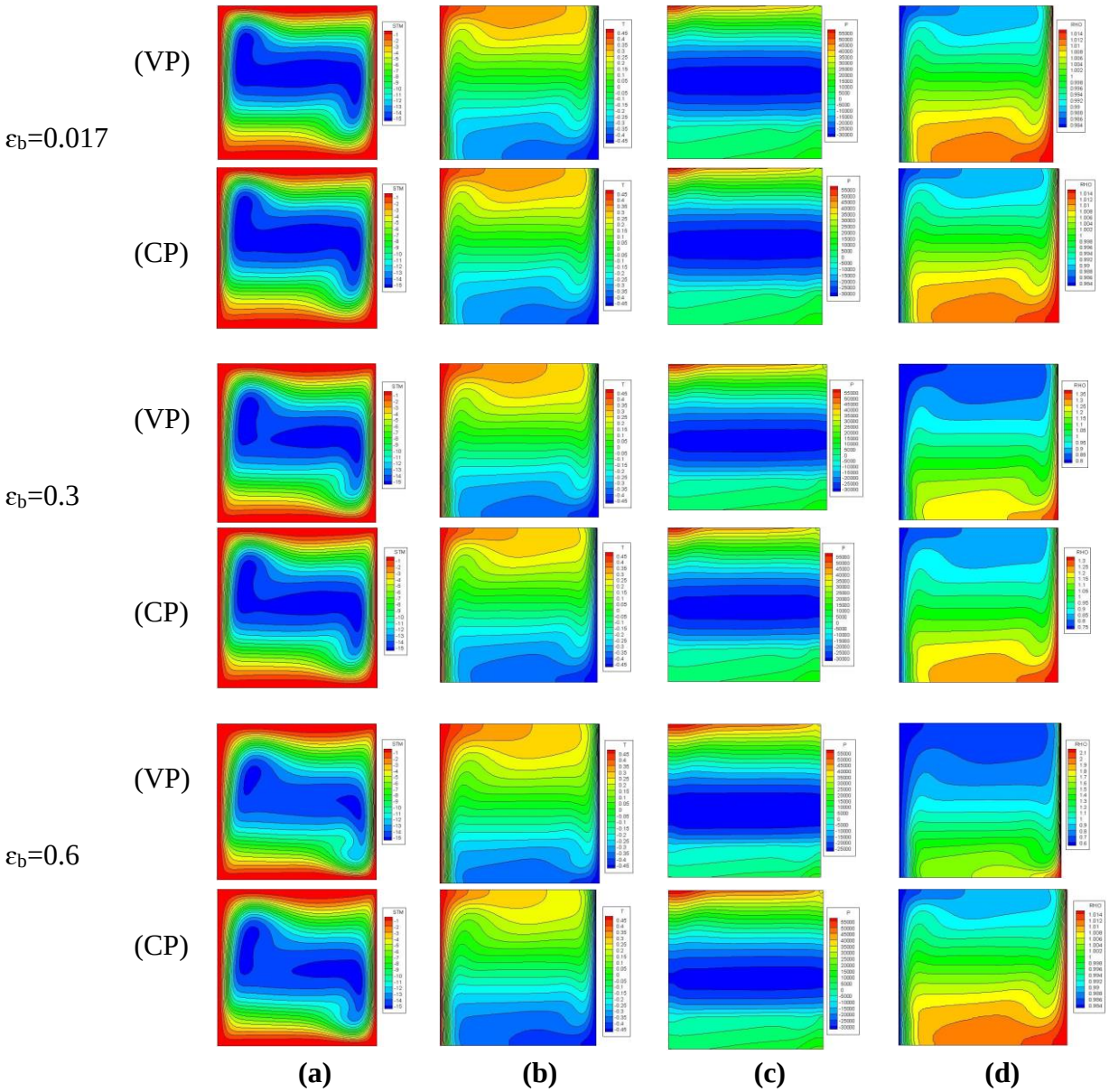

Figure V.8: Streamlines (a), isotherms (b), pressure (c) and density (d) profiles for variable (VP) and constant (CP) properties and for different values of ε_b

Figure V.9 illustrates the changes in the Nusselt number at the hot and cold walls. When examining convective heat transfer, significant variations are observed in the patterns of the hot and cold walls based on the Boussinesq parameter ε_b. This behavior is particularly pronounced at the top of the cavity, where the Nusselt number is higher for $\varepsilon_b = 0.6$ on the hot wall compared to $\varepsilon_b = 0.017$. Conversely, the opposite behavior is observed on the cold wall.

The presence of the porous layer also affects heat transfer. For Y ≤Yp, regardless of the value of ε_b and whether the properties are constant or variable, the Nusselt number remains almost constant. However, when Y >Yp, the profiles of the Nusselt number are no longer constant, and increasing the values of the Boussinesq parameter (ε_b> 0.017) leads to higher Nusselt number values. Incorporating variable properties somewhat enhances heat exchange at the top wall compared to fixed properties.

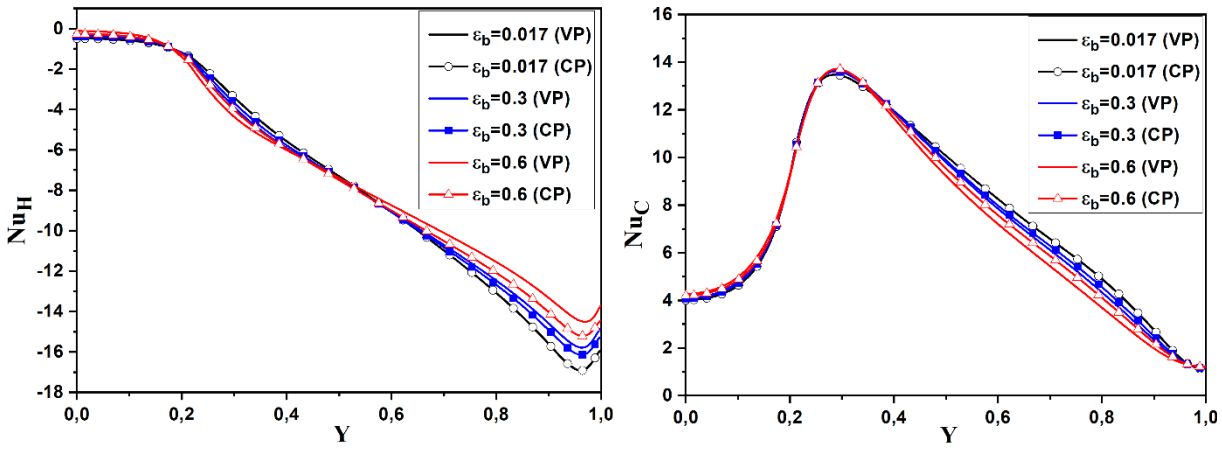

Figure V.9: Variations of convective Nusselt numbers at the hot and cold walls for Ra=10^6, Da=10^{-5}, Yp=0.2 and ε = 0.4

Figure V.10 presents the variations in the average Nusselt numbers (Nu_{avg}) considering different Darcy (Da) numbers (a), and porosity (ε) numbers (b). When low Darcy and porosity numbers are considered (Da ≤10^{-5} and ε ≤ 0.4), the porous layer acts as a solid block and approaches nearly isothermal conditions, as shown in Figure V.6 (a, b). As the porosity and permeability increase, the flow penetrates the porous region, resulting in a monotonic increase in heat transfer.

Eventually, for very high porosity and permeability values (Da > 10^{-4}, ε> 0.4), where the friction within the porous medium becomes minimal, the Nu_{avg} stabilizes at a constant value, resembling the solution for a completely fluid-filled cavity. These scenarios showcase a progressive shift from conduction to convection within the porous zone. We have specifically chosen these values of porosity and permeability for further analysis, which will be elaborated in detail in our future work.

The incompressible approach based on the Boussinesq hypothesis is applicable for simulating natural convection in a cavity without a porous medium (Yp=0) as well as convection in a cavity containing a porous medium (Yp>0) for low temperature gradients. According to Figure V.11, when the temperature difference (ΔT) is less than 30°C, which corresponds to a value of the Boussinesq coefficient ($\varepsilon_b \leq 0.05$), there are no significant

differences between constant properties and variable properties. However, as the temperature difference increases, there is a substantial divergence between the results of the Boussinesq model and those of the low Mach number model, especially when ε_b reaches its highest value of 0.6, corresponding to $\Delta T = 360°C$. It can be observed that variable properties exhibit greater heat exchange than constant properties, as noted previously.

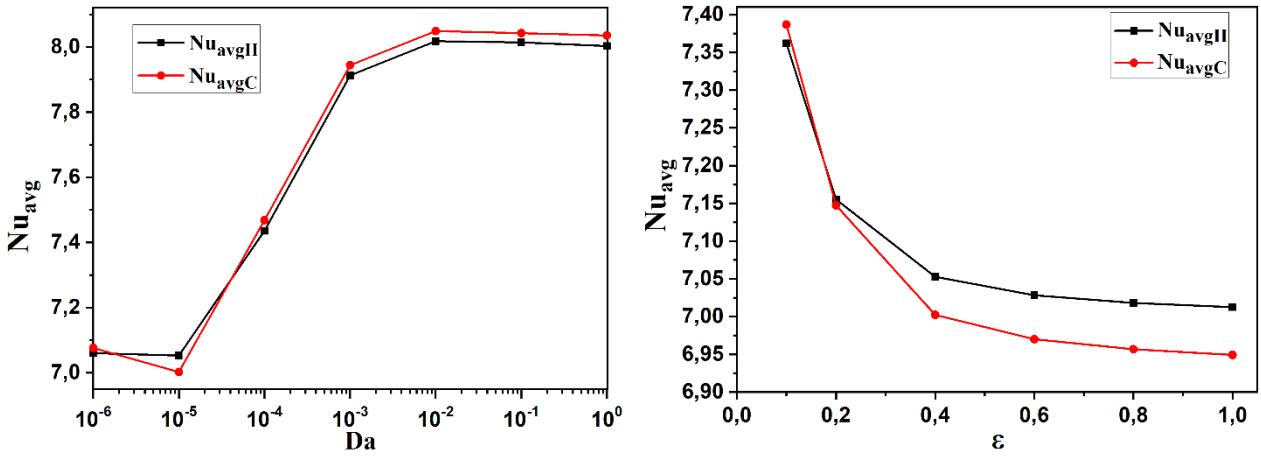

Figure V.10: Variation of the average Nusselt number as a function of Darcy number (a) for $\varepsilon = 0.4$ and porosity ε (b) for $Da=10^{-5}$

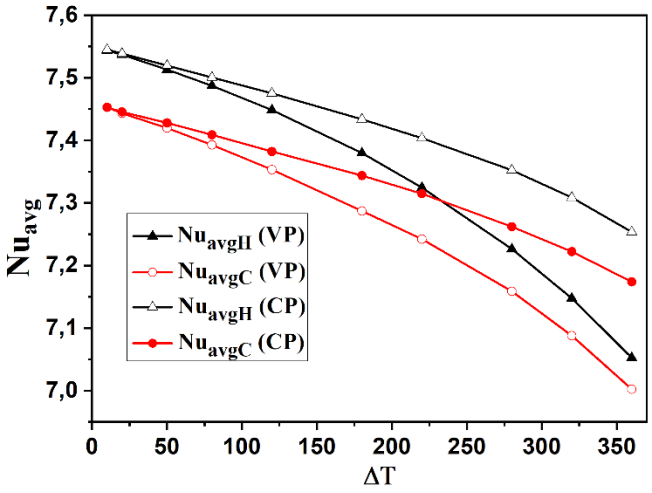

Figure V.11: Variation of the average Nusselt number as a function of difference temperature ΔT for $Da=10^{-5}$ and $\varepsilon = 0.4$

V.6.2 Impact of porosity characteristics the flow and heat transfer

The objective of this section is to explore the effects of fluid penetration into the porous layer and the related heat transfer mechanisms. Our proposed modeling configuration involves the placement of a porous layer at the base of a square enclosure. We investigate variations in the permeability of the porous layer (measured by the Darcy number) and the porosity (ε) across the non-dimensional thickness (Yp) of the porous layer, spanning from 0 to 1. Throughout the computational analyses, we keep the Rayleigh number ($Ra = 10^6$) and Boussinesq parameter ($\varepsilon_b = 0.6$) constant.

V.6.2.1 Influence of Darcy number

The Darcy number plays a crucial role in comprehending the dynamics of heat transfer and fluid flow within porous materials. Adjusting the Darcy number reveals its impact on both the horizontal and vertical temperature profiles, as illustrated in Figure V.12. As the Darcy number rises (indicating increased permeability and fluid flow through the porous medium), even with Yp=0.2, the heat transfer process becomes more effective. A higher Darcy number results in a more uniform horizontal temperature distribution and a reduction in temperature differentials across the porous layer. This phenomenon is attributed to enhanced convective heat transfer, driven by significant temperature gradients at ε_b=0.6.

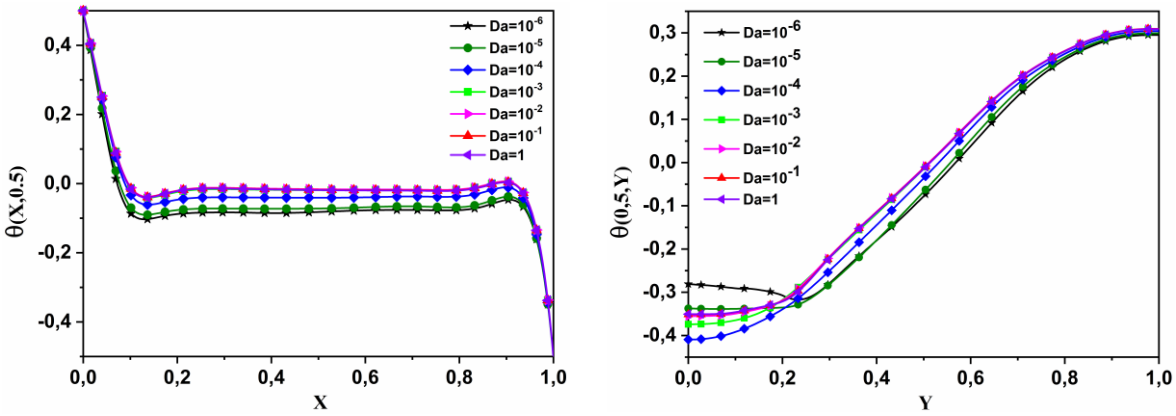

(a) (b)

Figure V.12: Temperature profiles at the midpoint height Y= 0.5 (a) and the midpoint plane X=0.5 (b) for Ra=10^6, Yp=0.2, ε = 0.4, ε_b=0.6, and different Darcy number values

In terms of fluid dynamics (see Figure V.13), a rise in the Darcy number leads to higher velocities within the porous medium (Y≤Yp). This enhanced flow is attributed to the decreased resistance to fluid motion resulting from higher permeability. As a result, the fluid tends to distribute more uniformly in the remaining cavity (Y>Yp). However, changes in the Darcy number have a relatively minor influence on vertical velocities. Vertical flow is predominantly governed by buoyancy forces, influenced by parameters such as the Rayleigh number (Ra) and the Boussinesq parameter (ε_b). While the Darcy number impacts flow patterns and the presence of a porous layer with limited permeability results in a rapid velocity reduction within the fluid region, its effect on vertical velocities is less significant compared to horizontal velocities. This suggests that heat transfer predominantly occurs via conduction within the porous region.

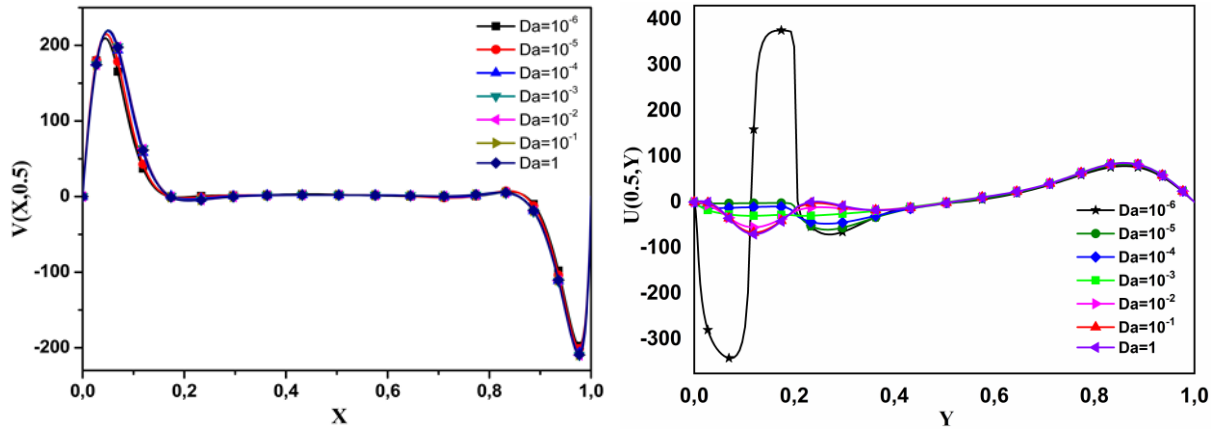

(a) (b)

Figure V.13: Vertical (a) and horizontal (b) velocities at the horizontal cross section and the vertical cross section for Ra=10^6, Yp=0.2, ε = 0.4, ε_b=0.6, and different Darcy numbers

Figure V.14 demonstrates the impact of the Darcy number on streamlines and isotherms. At low Darcy numbers (Da≤10^{-5}), the porous layer behaves as a solid wall, exhibiting nearly uniform temperatures. With increasing permeability (Da>10^{-5}), fluid flow penetrates the porous medium, leading to improved heat transfer. At very high Darcy numbers (Da≥10^{-2}), streamlines and isotherms stabilize, remaining relatively constant. This stability signifies that the streamlines and isotherms indicate that the convective flow patterns and temperature distribution reach an equilibrium, ensuring consistent heat transfer efficiency.

This balance is reflected in the attainment of a uniform average Nusselt number, akin to fully fluid-filled enclosures. Notably, there is a substantial rise in Nu for lower Darcy values (refer to Figure V.15). These findings illustrate a gradual shift from conduction-dominated to convection-dominated heat transfer within the porous domain. Additionally, the decrease in the average Nusselt number between scenarios with a small Boussinesq parameter (ε_b=0.017) and a large Boussinesq parameter (ε_b=0.6) can be attributed to the impact of large temperature differences and the thermodependency of thermophysical properties.

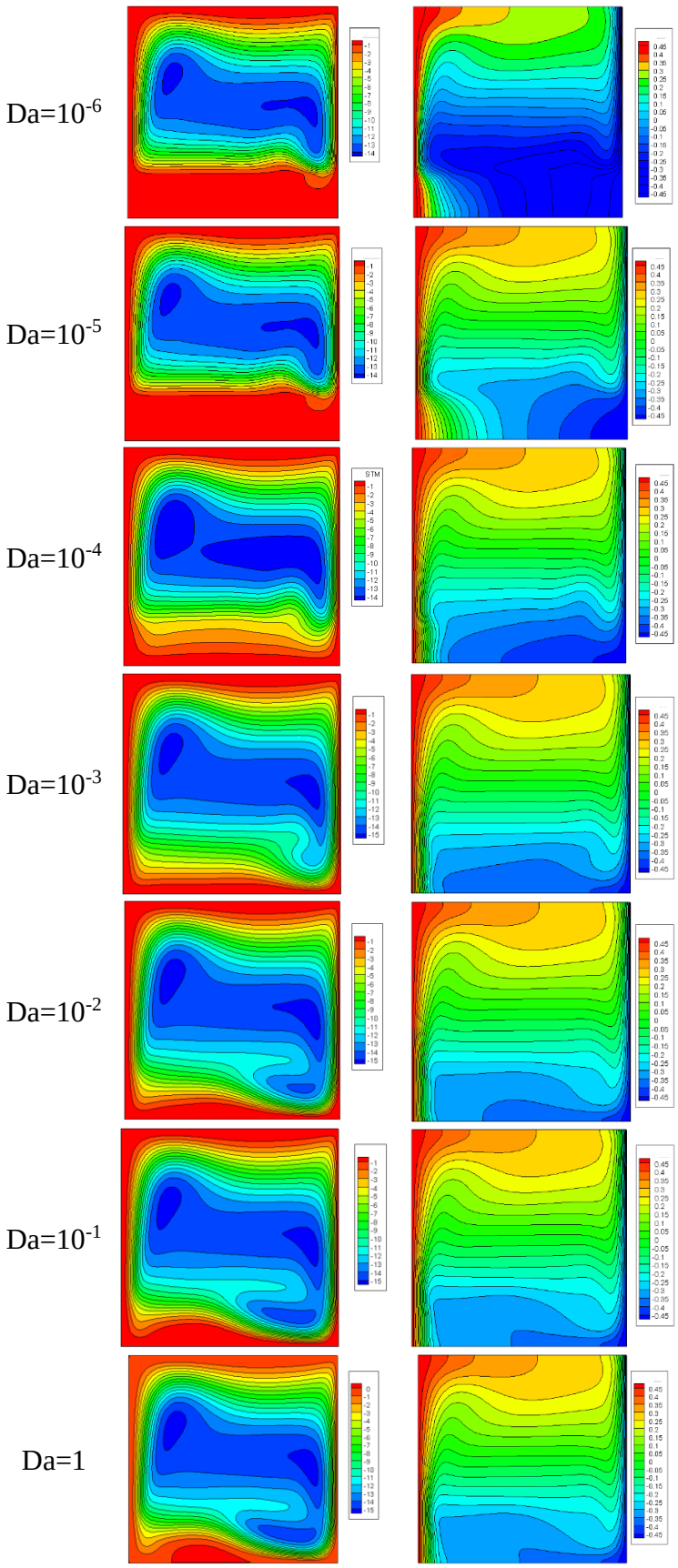

Figure V.14: Streamlines (a), isotherms (b), for $Ra=10^6$, Yp=0.2, $\varepsilon = 0.4$, $\varepsilon_b = 0.6$, and different values of Darcy number

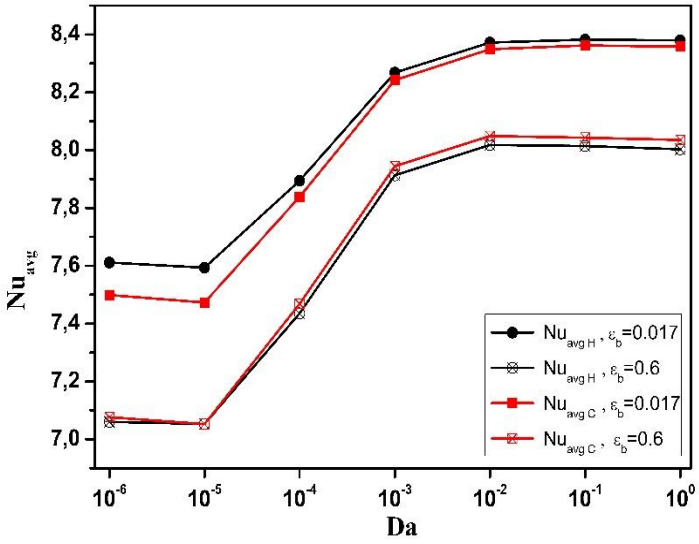

Figure V.15: Variations of the average Nusselt number as a function of Darcy number, for low (ε_b=0.017) and high (ε_b=0.6) temperature differences

V.6.2.2 Impact of porosity ε

The porosity of a porous material represents the fraction of voids or pores relative to the total volume of the substance. These voids or pores acts as conduits for fluid circulation within the porous medium. Thus, adjusting the porosity parameter directly affects the volume of space accessible for fluid motion, consequently influencing the dynamics of heat transfer and fluid flow.

An increase in porosity implies a greater presence of voids within the porous material, which creates wider channels for fluid flow. This increase in void space decreases the interaction between the solid matrix and the fluid, consequently reducing the efficiency of convective heat transfer. As a result, the temperature distribution within the cavity changes, often showing more pronounced temperature gradients across the porous layer (see Figure 16). Elevated porosity values typically correspond to diminished heat transfer effectiveness due to reduced convective thermal effects.

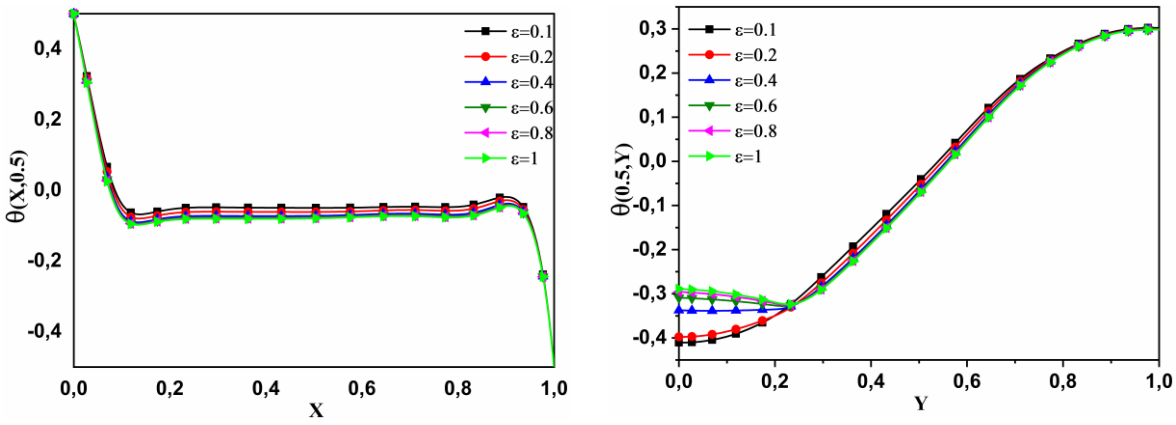

(a) (b)

Figure V.16: Temperature profiles at mid-height Y= 0.5 (a) and mid-plane X=0.5 (b) for Ra=10^6, Yp=0.2, Da=10^{-5}, ε_b = 0.6, and different values of porosity coefficient

Figure V.17 illustrates that higher porosity values are associated with lower horizontal and vertical velocities in fluid flow. This decline is a result of the increased empty space resulting from higher porosity, which in turn raises the resistance to fluid flow. Consequently, fluid velocities diminish, enhancing flow through the porous media (Yp≤0.2).

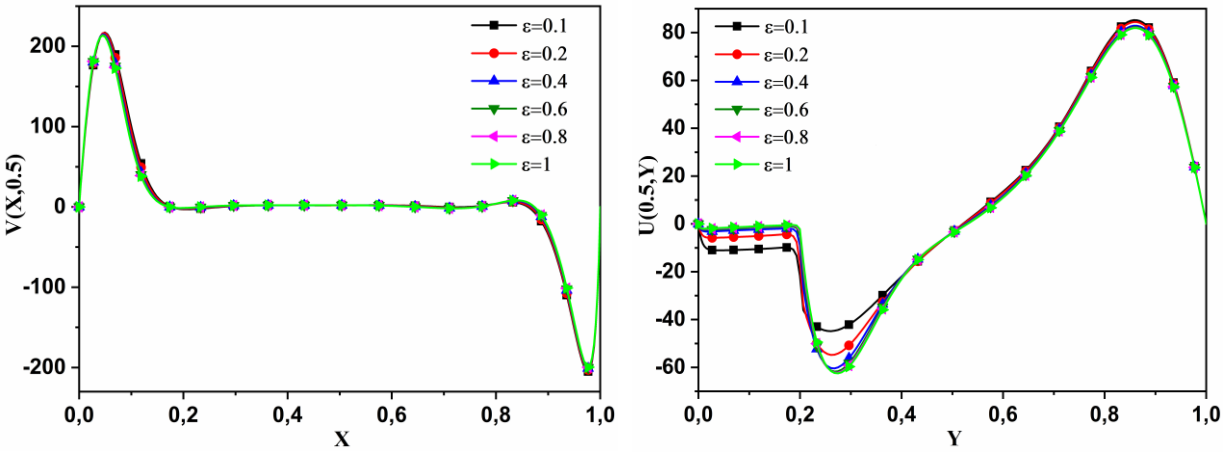

(a) (b)

Figure V.17: Vertical (a) and horizontal (b) velocities for $Ra=10^6$, Yp=0.2, $Da=10^{-5}$, ε_b = 0.6, and different values of porosity coefficient

Changes in porosity significantly impact streamlines and isotherms, which, in turn, reflect changes in fluid flow patterns and heat transfer characteristics within the porous medium (see Figure V.18). Greater porosity values ($\varepsilon > 0.4$) promote increased fluid penetration, leading to larger temperature gradients across the porous material. Conversely, lower porosity values ($\varepsilon \leq 0.4$) yield more intricate streamlines and smoother isotherms, signifying enhanced convective heat transfer and reduced temperature gradients.

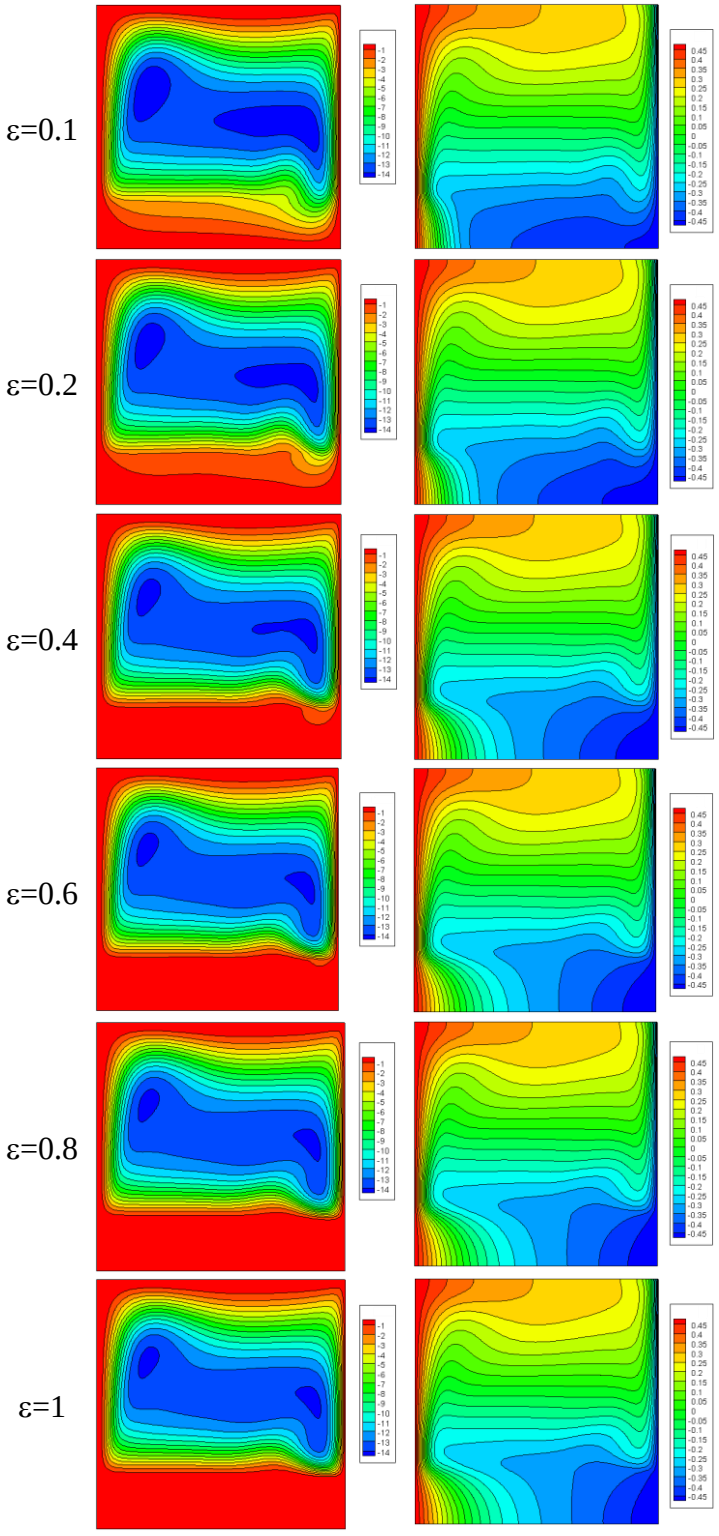

Figure V.18: Streamlines (a), isotherms (b), for Ra=10^6, Yp=0.2, Da = 10^{-5}, ε_b = 0.6, and different values of porosity coefficient

The distribution of the average Nusselt number, as depicted in Figure V.19, illustrates a relationship between the porosity number and heat transfer. It is apparent that with the increase in the porosity number, the average Nusselt number initially decreases. However, it eventually stabilizes at relatively constant values ($\varepsilon \geq 0.6$). This observation suggests the

presence of a critical porosity value beyond which further increases have minimal effect on heat transfer and fluid flow. This result aligns with previous studies indicating that higher porosity encourages fluid penetration, leads to larger temperature gradients, and enhanced convective heat transfer. Conversely, lower porosity values result in smoother flow patterns, reduced temperature gradients, and improved convective heat transfer efficiency.

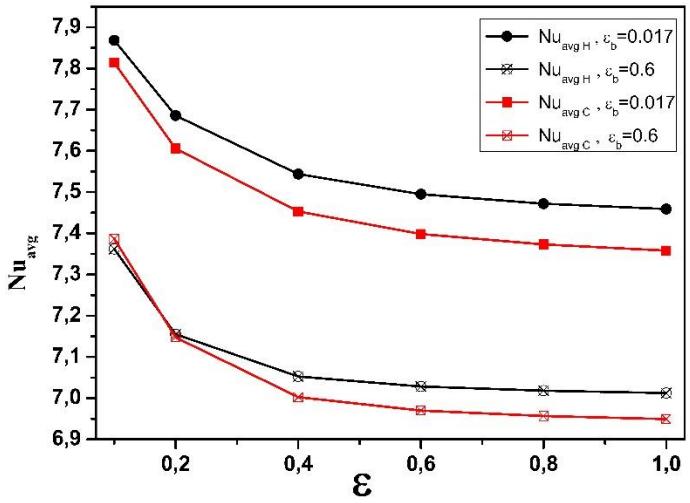

Figure V.19: Variations of the average Nusselt number as a function of Porosity coefficient for low (ε_b = 0.017) and large (ε_b = 0.6) temperature differences

V.6.2.3 Impact of porous layer thickness Yp

Our study also examines the impact of the dimensionless porous layer thickness (Yp) on both flow patterns and heat transfer processes. In Figure V.20, temperature profiles in the horizontal and vertical midplanes (X=0.5 and Y=0.5) are depicted for different Yp values. For thinner porous layers (Yp ≤ 0.4), the temperature profiles exhibit notable gradients, indicating a predominantly convective situation with stratification at the cavity's base. In contrast, with an increase in Yp (Yp> 0.4), the temperature profiles tend to adopt a more linear trend, resembling the behavior typically observed in a fully conductive cavity.

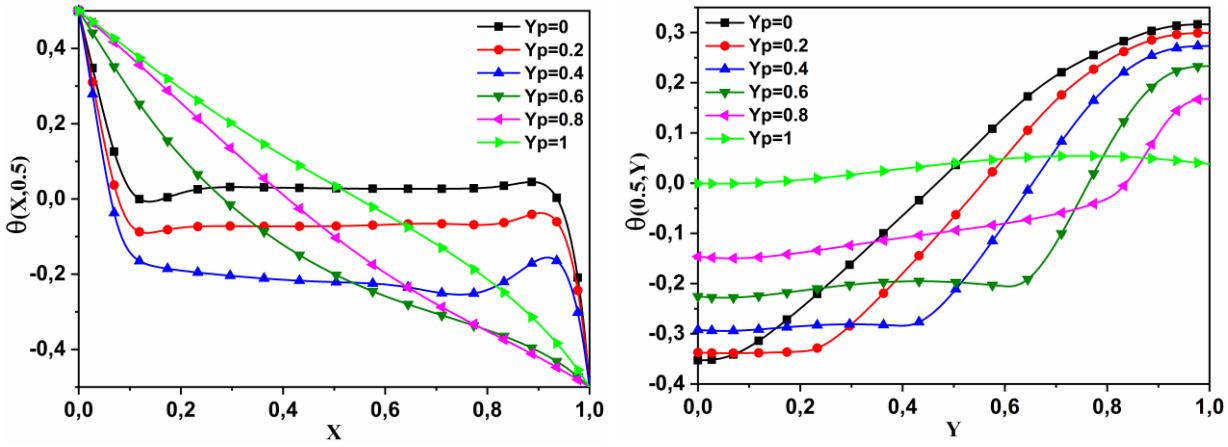

(a) (b)

Figure V.20: Temperature profiles at mid-height Y= 0.5 (a) and mid-plane X=0.5 (b) for Ra=10^6, Da=10^{-5}, ε = 0.4, ε_b = 0.6, and different layer thickness values.

Figure V.21 illustrates the profiles of horizontal and vertical velocities in the transverse plane (X-Y). Within the porous region, the velocity profile demonstrates a near-linear pattern. At Yp=0, the profiles signify a purely convective nature. Furthermore, the vertical velocity profiles exhibit a symmetric feature, each profile displaying two peaks within the boundary layers. These peaks diminish in amplitude as the porous layer thickness increases. At Yp=1, representing a fully porous enclosure, both velocity profiles become predominantly linear, indicating a primarily conductive flow. Each horizontal velocity profile also reveals two peaks near the vertical wall, gradually transitioning to a more linear behavior as they approach the bottom of the cavity. Notably, the profiles indicate the absence of circulation in the lower region of the cavity.

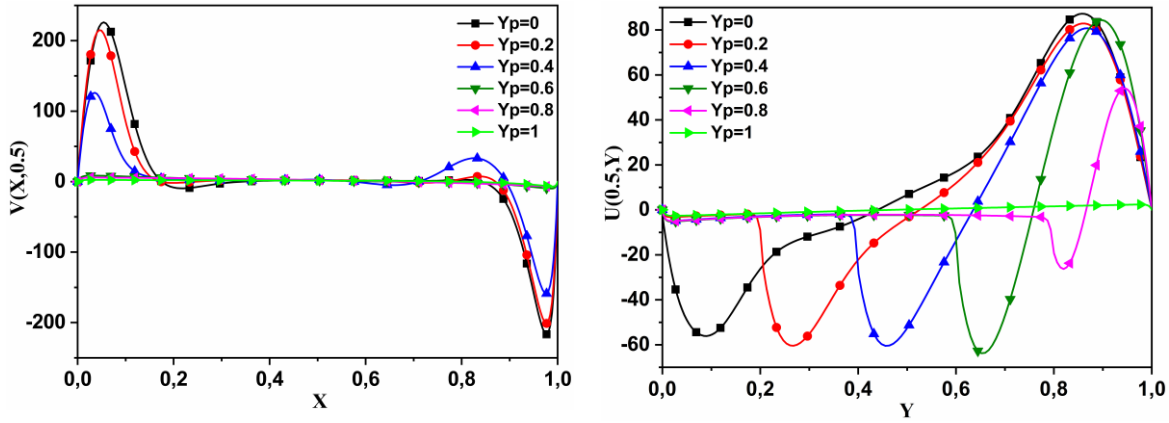

(a) (b)

Figure V.21: Vertical (a) and horizontal (b) velocities for Ra=10^6, ε=0.4, Da=10^{-5}, ε_b = 0.6, and different layer thickness values

In Figure V.22, contour plots depict isotherms and streamlines, offering insights into flow and heat transfer characteristics. For Yp=0 (no porous layer), the streamlines reveal two cells rotating clockwise at the cavity center, illustrating pure natural convection. With an increase in the porous layer thickness (Yp ≥ 0.2), the strength of these cells diminishes compared to the initial scenario, until reaching the configuration of a fully porous cavity (Yp = 1), where a single cell dominates the cavity space.

For a fully porous cavity (Yp = 1), the isotherms within the porous medium exhibit a predominantly vertical orientation, indicating vertical heat conduction through the porous material. Heat is conducted from the warmer (high-temperature) fluid in the upper region to the cooler (low-temperature) fluid in the lower region. With a substantial thickness of the porous layer (Yp = 1), flow obstruction within the porous medium is notable, and flow primarily occurs through diffusion in the porous material.

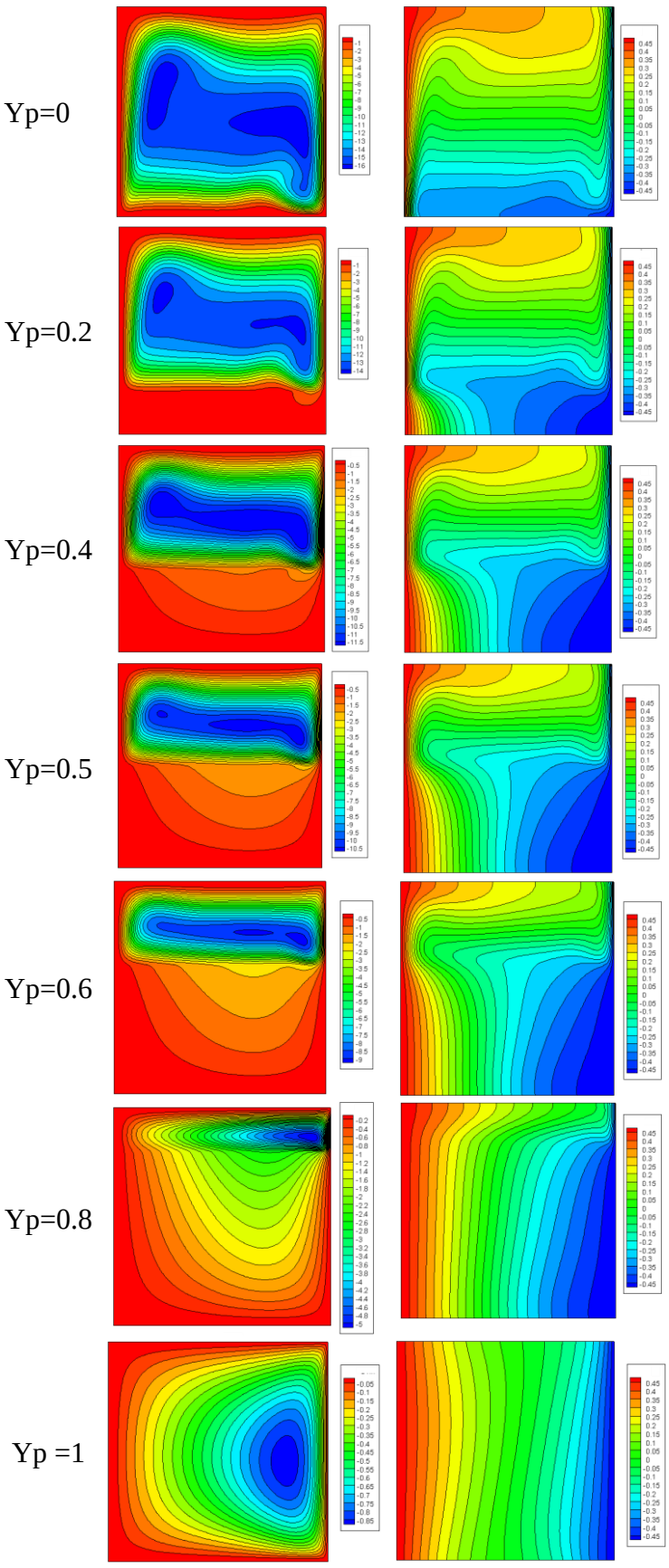

Figure V.22: Streamlines (a), isotherms (b), for Ra=10^6, ε = 0.4, Da = 10^{-5}, ε_b = 0.6 and different layer thickness values

Figure V.23 illustrates the distribution of the Nusselt number concerning the dimensionless thickness of the porous layer (Yp). The plot illustrates that as the porous layer thickness tends towards zero, corresponding to pure natural convection, the Nusselt number converges to a singular value. likewise, as the thickness of the porous medium approaches unity, representing a state of pure conduction, the flow transitions towards a predominantly conductive regime across the medium.

The influence of a porous medium on natural convection flow is more significant compared to a system without a porous medium. The presence of a porous medium significantly alters the characteristics of fluid flow and heat transfer within the system. However, when examining the average Nusselt number, which acts as an indicator of convective heat transfer, the impact of the porous medium is relatively minor until a certain porosity value is attained, approximately around Yp = 0.8. This suggests that within this range, the porosity of the medium has limited effects on heat transfer.

However, prior to reaching this critical porosity value, a considerable decrease in the average Nusselt number is observed. This reduction is attributed to the inhibition of spontaneous convection movement caused by the presence of the porous medium. In other words, the porous medium hampers the natural flow of the fluid, leading to a reduction in convective heat transfer.

The graph can be divided into three distinct zones. The initial zone signifies a predominantly diffusive region, indicating minimal flow effects (Yp ≥ 0.8). The third zone corresponds to mostly convective flow, leading to substantial heat transfer (Yp=0). The intermediate zone is characterized by a drastic decline in the Nusselt number as a function of Yp.

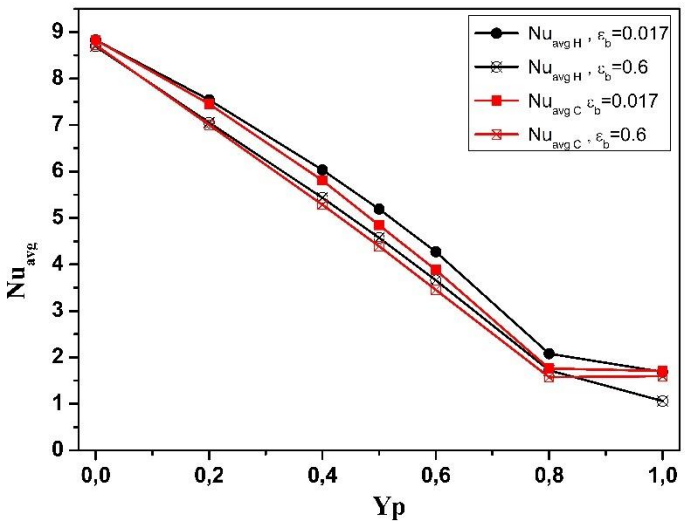

Figure V.23: Variations of the average Nusselt number as a function of layer thickness for low (ε_b= 0.017) and large (ε_b = 0.6) temperature differences

V.7 CONCLUSIONS

This chapter presented a comprehensive analysis of the coupled natural convection and porous media within a square cavity, employing a Low-Mach-number approach and a control volume method. By examining the effects of temperature difference, porous layer characteristics (porosity and permeability), and temperature-dependent fluid properties (constant or variable), we have gained valuable insights into the flow patterns and heat transfer performance of the system. Key findings from this study can be summarized as follows:

- Under non-Boussinesq conditions and with increasing temperature gradient, there is a notable difference between the solutions obtained using compressible ($\varepsilon_b > 0.017$) and incompressible ($\varepsilon_b = 0.017$) models. Hence, the coupled natural porous media system can be accurately simulated by employing the compressible model with the assumption of a low Mach number.
- Fluid compressibility in porous media can have a significant impact on natural convective heat transfer. It can change the fluid flow patterns, thereby affecting the rate of heat transfer. Furthermore, fluid compressibility can also influence the thermal expansion and contraction of the porous medium, introducing additional complexity to the system.
- The presence of a porous layer at the bottom of the cavity reduces stratification in the central region and promotes flow along the horizontal walls and at the upper section of the cavity. This configuration also decreases fluid temperatures, resulting in substantial alterations in flow patterns and temperature distribution.
- Variations in thermophysical properties can significantly affect thermal transmission and flow patterns.
- The presence of a low-permeability porous layer caused a significant decrease in heat transmission. In contrast, it was noted that heat transfer coefficients increased with higher permeability of the porous material. The Nusselt number achieves its peak at a low porosity value of 0.1 and stabilizes at a consistent value as porosity rises to 0.8. This indicates the presence of an optimal porosity range for maximizing heat transfer efficiency.
- With the increases in the Darcy number, the thermal and dynamic fields within the porous layer becomes more pronounced. This implies that as permeability rises, the behavior starts resembling that of a fluid medium. The Nusselt number reaches its maximum and remains stabilizes when the Darcy number reaches 10^{-2}, indicating the optimal condition for heat transfer efficiency in relation to Darcy permeability.
- The Nusselt number exhibited an inverse correlation with the increase in Yp (the porous layer thickness), converging towards a steady value when the thickness approached zero, indicating pure natural convection. Similarly, as Yp approached unity, it stabilized at an almost consistent value at Yp = 0.8, akin to the porosity-related behavior, highlighting the significance of thickness in regulating the heat transfer efficiency within the porous medium. The flow through the porous medium transitioned towards a fully conductive state.

The conclusions drawn in this chapter have significant implications for enhancing the design and performance of systems integrating porous layers across diverse engineering applications.

In the realm of thermal engineering, understanding the influence of permeability and porosity on heat transfer facilitates the advancement of more effective thermal management strategies for energy-efficient buildings and heat exchange systems. Similarly, in geothermal energy and oil recovery sectors, a deep understanding of fluid flow and heat transfer in porous reservoirs aids in optimizing recovery conditions and elevating energy production rates. Profound insights into heat transfer in porous media are crucial for designing and optimizing heat exchangers in the petroleum industry. Furthermore, utilizing porous materials in electronics cooling enhances the performance and reliability of electronic systems. These outcomes also have the potential to refine mathematical models and simulation methodologies for fluid dynamics simulations that incorporate porous media effects.

References

[1] M. V. Farahani, M. Mousavi Nezhad. On the effect of flow regime and pore structure on the flow signatures in porous media, Phys. Fluids. 34 (11), 115139 (2022) https://doi.org/10.1063/5.0120201

[2] A. Hassanpouryouzband, E. Joonaki, M. V. Farahani, S. Takeya, C. Ruppel, J. Yang, N. J. English, J. M. Schicks h, K. Edlmann, H. Mehrabian, Z. M. Aman, B. Tohidi, Gas hydrates in sustainable chemistry, Chem. Soc. Rev. 49 (15), 5225-5309 (2020). https://doi.org/10.1039/C8CS00989A

[3] M. V. Farahani, A. Hassanpouryouzband, J. Yang, B. Tohidi, Heat transfer in unfrozen and frozen porous media: Experimental measurement and pore-scale modelling, Water Resour. Res. 56(9), p.e 2020WR027885 (2020). https://doi.org/10.1029/2020WR027885

[4] A. Hassanpouryouzband, J. Yang, B. Tohidi, E. Chuvilin, V. Istomin, B. Bukhanov, A. Cheremisin, Co_2 capture by injection of flue gas or CO_2–N_2 mixtures into hydrate reservoirs: dependence of CO_2 capture efficiency on gas hydrate reservoir conditions, Environ. Sci. Tech. 52 (7), 4324–4330 (2018). https://doi.org/10.1021/acs.est.7b05784

[5] D. Damene, Z. Alloui, I. Alloui, P. Vasseur, Variable Permeability Effects on Natural Convection in a Vertical Porous Layer with Uniform Heat Flux from the Side, Transp Porous Med. 137, 287–306 (2021). https://doi.org/10.1007/s11242-021-01553-x.

[6] O.R. Alomar, Analysis of variable porosity, thermal dispersion, and local thermal non-equilibrium on two-phase flow inside porous media, Applied Thermal Engineering. 154, 263–283 (2019). https://doi.org/10.1016/j.applthermaleng.2019.03.069.

[7] S.Z. Shuja, B.S. Yilbas, S.M.A. Khan, Flow over a porous structure in a square cavity: effects of the porous structure size and porosity on the heat transfer performance and fluid pressure loss, Heat Transfer Research. 46 (12), 1081-1099 (2015). https://doi.org/10.1615/HeatTransRes.2015005342.

[8] S. Hamimid, M. Guellal, A. Amroune, N. Zeraibi, Effect of a porous layer on the flow structure and heat transfer in a square cavity, Fluid Dynamics & Materials Processing. 8(1), 69–90 (2011). https://doi.org/10.3970/fdmp.2011.008.069

[9] M. Yan, C. Lu, J. Yang, Y. Xie, J. Luo, Impact of low- or high-permeability inclusion on free convection in a porous medium, Geofluids. 2019, e8609682 (2019). https://doi.org/10.1155/2019/8609682

[10] W. Tanikawa, T. Shimamoto, Klinkenberg effect for gas permeability and its comparison to water permeability for porous sedimentary rocks, Hydrology and Earth System Sciences Discussions. 3, 1315–1338 (2006). https://doi.org/10.5194/hessd-3-1315-2006.

[11] X.-H. Tan, X.-P. Li, J.-Y. Liu, L.-H. Zhang, Z. Fan, Study of the effects of stress sensitivity on the permeability and porosity of fractal porous media, Physics Letters A. 379(39), 2458–2465 (2015). https://doi.org/10.1016/j.physleta.2015.06.025.

[12] F. Civan, Scale effect on porosity and permeability: Kinetics, model, and correlation, AIChE Journal. 47, 271–287. (2001). https://doi.org/10.1002/aic.690470206.

[13] F. Habbachi, F.S. Oueslati, R. Bennacer, M. Ganaoui, A. Elcafsi, Three-dimensional simulation of natural convection in cubic cavity partially filled with porous media, Energy Procedia. 139, 617–623 (2017). https://doi.org/10.1016/j.egypro.2017.11.262.

[14] F. Ouarhlent, A. Soudani, Numerical study of thermal convection in a porous medium (in French), Journal of Renewable Energies. 21 (4), 495–504 (2018). https://doi.org/10.54966/jreen.v21i4.707.

[15] H.-K. Lee, J.-H. Park, D.-Y. Kim, T.-H. Lee, A study on the characteristics of the diffusion layer thickness and porosity of the PEMFC, Journal of Power Sources. 131 (1-2), 200–206 (2004). https://doi.org/10.1016/j.jpowsour.2003.12.039.

[16] Y. Gao, A. Montana, F. Chen, Evaluation of porosity and thickness on effective diffusivity in gas diffusion layer, Journal of Power Sources. 342, 252–265 (2017). https://doi.org/10.1016/j.jpowsour.2016.12.052.

[17] C. Kang, P. Mirbod, Porosity effects in laminar fluid flow near permeable surfaces, Phys. Rev. E. 100, 013109 (2019). https://doi.org/10.1103/PhysRevE.100.013109.

[18] S.A. Suslov, S. Paolucci, Nonlinear analysis of convection flow in a tall vertical enclosure under non-Boussinesq conditions, J. Fluid Mech. 344, 1–41 (1997). https://doi.org/10.1017/S0022112097005971.

[19] S. A. Suslov, Analysis of coupling between hydrodynamic and thermal instabilities in non-boussinesq convection, Nonlinear Anal. Theory Methods Appl. 63 (5-7), e1435–e1443. (2005). https://doi.org/10.1016/j.na.2005.01.057

[20] S. Hamimid, M. Guellal, M. Bouafia, Numerical study of natural convection in a square cavity under non-Boussinesq condition, Therm. Sci. 20 (5), 1509-1517 (2016). https://doi.org/10.2298/TSCI130810084H.

[21] P. Quéré, C. Weisman, H. Paillère, J. Vierendeels, E. Dick, R. Becker, M. Braack, J. Locke, Modelling of natural convection flows with large temperature differences: a benchmark problem for low Mach number solvers. Part 1, Reference solutions, Mathematical Modelling and Numerical Analysis. 39 (2005) 609–616. https://doi.org/10.1051/M2AN:2005027.

[22] Hamimid, S., Guellal, and Bouafia, M. "Numerical Simulation of Combined Natural Convection Surface Radiation for Large Temperature Gradients," *J. Thermophys. Heat Transf.*, Vol 29 (3), 2015, pp.636–645, https://doi.org/10.2514/1.T4437

[23] Gray, D. D., and Giorgini, A., "The Validity of the Boussinesq Approximation for Liquids and Gases," *International Journal of Heat and Mass Transfer*, Vol. 19, 1976, pp. 545–551, https://doi.org/10.1016/0017-9310(76)90168-X.

VI.1 INTRODUCTION

In a variety of natural phenomena and engineering applications, such as grain storage, air-conditioning systems and building insulation [1,2], as well as in many industrial applications such as furnaces, combustion equipment, burners, electronic component cooling and printed circuit boards [3–5], the interplay between natural convection and heat transfer in porous/fluid composite domains is apparent in problems of natural convection coupled with thermal radiation [6,7]. Most of these applications involve significant temperature variations and require modeling that takes into account real variations in fluid properties and the impact of compressibility. The low Mach number (LMN) assumption is an important numerical issue for low-velocity compressible flows, as it allows realistic fluctuations in fluid properties and compressibility effects [8,9]. Global pressure is divided into two terms: mean thermal pressure and dynamic pressure. This decomposition eliminates acoustic waves, enabling substantial fluctuations in density as a function of temperature. Numerous numerical models and tests have been carried out in recent years to study natural convection and heat transfer processes in cavities, with and without thermal radiation [10–12]. The differentially heated cavity problem is a famous case in CFD code verification that focuses on the influence of surface thermal radiation on natural circulation in a differentially heated cavity filled with a porous medium and with large temperature changes.

Several previous studies have been conducted on the coupling of natural convection and surface radiation phenomena [13–17]. Hamimid et al. used a numerical approach with a finite volume method to investigate the combined laminar natural convection and surface radiation in a differentially heated square cavity. The study analyzed the impact of emissivity on temperature and velocity profiles within the cavity and presented results for convective and radiative Nusselt numbers under various conditions [13]. Another numerical analysis was conducted to study the combined effects of laminar natural convection, internal heat generation, and surface radiation. The researchers employed a finite volume method with a staggered grid and the SIMPLER algorithm to examine an air-filled square cavity with uniform emissivity on all four walls. The study reported results illustrating the influence of emissivity and internal heat generation on streamlines and temperature contours within the cavity. It also presented the effects of different parametric conditions on convective and radiative Nusselt numbers [14].

This chapter focuses on investigating natural convection and heat transfer in a differentially heated cavity partially filled with a porous layer while considering the influence of surface thermal radiation. The cavity is a square enclosure with an adiabatic condition applied to the upper and lower walls. By varying the emissivity of the vertical surface radiation within the cavity (ranging from 0 to 1), we aim to understand the specific impacts of low permeability ($Da = 10^{-5}$) and high permeability ($Da = 10^{-3}$) of the porous medium on heat transfer and fluid flow phenomena. To obtain quantitative and qualitative information, we will perform simulations by setting up appropriate scenarios and analyzing the results. This chapter endeavor will provide a comprehensive understanding of the complex relationships between convection, radiation, temperature differences, and characteristics of the porous medium.

VI.2 PROBLEM FORMULATION

This study investigates a two-dimensional square cavity with a side H (FigureVI.1). The cavity is filled with a porous layer at its bottom and a variable-property Newtonian fluid. The natural convection problem is characterized by two vertically heated walls with specified temperatures $T_c, T_h \succ T_c$. The assumption is made that horizontal surfaces experience combined contributions from both convection and radiation $-k\frac{\partial T}{\partial y}+q_r=0$. All four walls are subjected to no-slip and zero-mass flux boundary conditions $\vec{V}=0$, maintaining the same emissivity value.

A Cartesian (x, y) coordinate system is employed, and the gravitational vector $\vec{g}$ is applied along the y-coordinate. Initial conditions include constant pressure p_0 and temperature T_0 distributions, as well as stationary flow $\vec{V}=0$. The Boussinesq parameter $\varepsilon_b=\Delta T/2T_0$ is introduced using the mean temperature and the temperature difference between the walls $\Delta T = T_h - T_c$.

U=V=0, $\theta=\theta_i$ for $\tau = 0$

U=V=0, $\theta=\theta_C=0.5$ for $0 \le Y \le 1$ and X= 0

U=V=0, $\theta=\theta_F=-0.5$ for $0 \le Y \le 1$ and X= 1

U=V=0, $\frac{\partial\theta}{\partial Y}-NrQr=0$ for $0 \le X \le 1$ and Y= 0

U=V=0, $\frac{\partial\theta}{\partial Y}-NrQr=0$ for $0 \le X \le 1$ and Y= 1

A flow model developed for low Mach numbers[13–15] is used to investigate the dynamics of the heated cavity. In this case, the Navier-Stokes equations are expressed as powers of a very small parameter M² (where M denotes the Mach number). The total pressure P is then divided into two components: average thermodynamic pressure $\overline{p}(t)$ and dynamic pressure P'. At an initial temperature of 300 K, the fluid (air) is considered to behave as an ideal gas in the current study. Sutherland's law is applied to calculate the transport parameters μ (T) and k (T).

$$\mu=\left(2\varepsilon_b T+1\right)^{3/2}\frac{\left(1+S_\mu/T_0\right)}{2\varepsilon_b T+1+S_\mu/T_0} \tag{VI.1}$$

Where S_μ=110.4 [18]. The conductivity is given by:

$$k(T)=\frac{\mu(T)}{\mathrm{Pr}} \tag{VI.2}$$

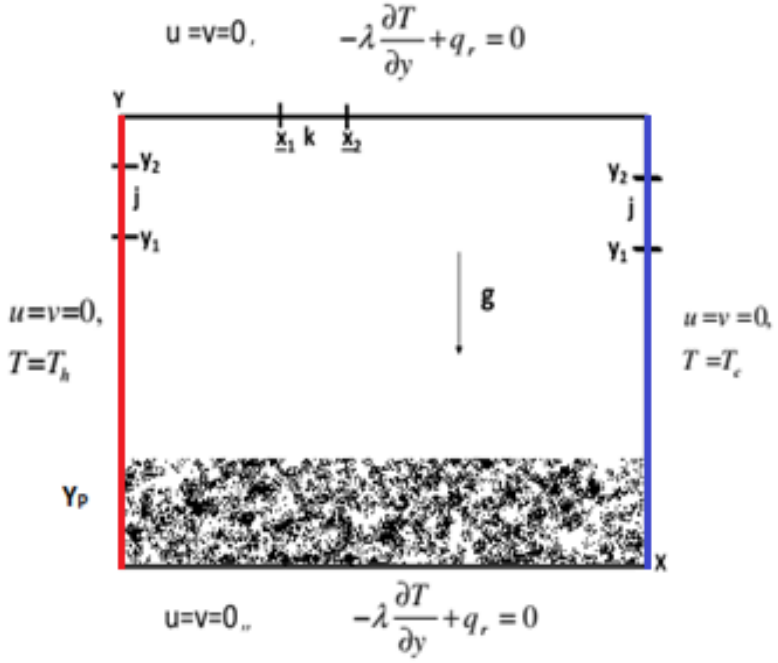

FigureVI.1: Flow configuration and coordinate system.

VI.3 GOVERNING EQUATIONS

The Low-Mach-Number equations are used to represent this flow as we are concerned with a case of significant temperature variations [16,19].

Fluid Region

$$\frac{\partial \rho}{\partial t}+\frac{\partial \rho u}{\partial x}+\frac{\partial \rho v}{\partial y}=0 \qquad \text{(VI.3)}$$

$$\rho\left(\frac{\partial u}{\partial t}+u\frac{\partial u}{\partial x}+v\frac{\partial v}{\partial y}\right)=-\frac{\partial p'}{\partial x}+\left\{\frac{\partial}{\partial x}\left(\mu\frac{\partial u}{\partial x}\right)+\frac{\partial}{\partial y}\left(\mu\frac{\partial u}{\partial y}\right)+\frac{1}{3}\nabla\mu\nabla.\vec{V}\right\} \qquad \text{(VI.4)}$$

$$\rho\left(\frac{\partial v}{\partial t}+u\frac{\partial v}{\partial x}+v\frac{\partial v}{\partial y}\right)=-g(\rho-\rho_0)-\frac{\partial p'}{\partial y}+\left\{\frac{\partial}{\partial x}\left(\mu\frac{\partial v}{\partial x}\right)+\frac{\partial}{\partial y}\left(\mu\frac{\partial v}{\partial y}\right)+\frac{1}{3}\nabla\mu\nabla.\vec{V}\right\} \qquad \text{(VI.5)}$$

$$\rho c_p\left(\frac{\partial T}{\partial t}+V\nabla T\right)=\left(\nabla.k\nabla T\right)+\frac{d\bar{p}}{dt} \qquad \text{(VI.6)}$$

$$\bar{p}=\rho RT \qquad \text{(VI.7)}$$

Porous region

$$\frac{\partial \rho}{\partial t}+\frac{\partial \rho u}{\partial x}+\frac{\partial \rho v}{\partial y}=0 \tag{VI.8}$$

$$\rho\left(\frac{1}{\varepsilon}\frac{\partial u}{\partial t}+\frac{1}{\varepsilon^2}u\frac{\partial u}{\partial x}+\frac{1}{\varepsilon^2}v\frac{\partial u}{\partial y}\right)=-\frac{\partial P'}{\partial x}+\frac{1}{\varepsilon}\left[\frac{\partial}{\partial x}\left(\mu\frac{\partial u}{\partial x}\right)+\frac{\partial}{\partial y}\left(\mu\frac{\partial u}{\partial y}\right)+\frac{1}{3}\Delta\mu\Delta\vec{V}\right]$$

$$-\mu\frac{u}{K}-\frac{1.75\rho}{\sqrt{150K}}\frac{|\vec{V}|}{\varepsilon^{3/2}}u \tag{VI.9}$$

$$\rho\left(\frac{1}{\varepsilon}\frac{\partial v}{\partial t}+\frac{1}{\varepsilon^2}u\frac{\partial v}{\partial x}+\frac{1}{\varepsilon^2}v\frac{\partial v}{\partial y}\right)=-\frac{\partial P'}{\partial y}+\frac{1}{\varepsilon}\left[\frac{\partial}{\partial x}\left(\mu\frac{\partial v}{\partial x}\right)+\frac{\partial}{\partial y}\left(\mu\frac{\partial v}{\partial y}\right)+\frac{1}{3}\Delta\mu\Delta\vec{V}\right]-g(\rho-\rho_0)$$

$$-\mu\frac{v}{K}-\frac{1.75\rho}{\sqrt{150K}}\frac{|\vec{V}|}{\varepsilon^{3/2}}v \tag{VI.10}$$

$$(\rho Cp)_{eff}(\frac{\partial T}{\partial t})+(\rho Cp)_f\left[u\frac{\partial T}{\partial x}+v\frac{\partial T}{\partial y}\right]=\frac{\partial}{\partial x}k\frac{\partial T}{\partial x}+\frac{\partial}{\partial y}k\frac{\partial T}{\partial y}+\frac{d\bar{p}}{dt} \tag{VI.11}$$

$$\left(\rho C_p\right)_{eff}=\varepsilon.\left(\rho C_p\right)_f+(1-\varepsilon)\left(\rho C_p\right)_s \tag{VI.12}$$

$$\left|\vec{V}\right|=\sqrt{u^2+v^2} \tag{VI.13}$$

The non-dimensional variables are used to make the non-dimensional equations.

$$\tau=\frac{\alpha t}{H^2},\ X=\frac{x}{H},\ Y=\frac{y}{H},\ U=\frac{uH}{\alpha},V=\frac{vH}{\alpha},\ \Pi=\frac{\varepsilon^2 p'H^2}{\rho\alpha^2},\ \overline{P}=\frac{\overline{p}}{p_0},\ \theta=\frac{T-T_0}{\Delta T}$$

$$\text{where: } \Delta T=T_H-T_C\ ,\ T_0=\frac{T_H+T_C}{2}$$

Fluid Region

$$\frac{\partial \rho^*}{\partial t}+\frac{\partial \rho^* U}{\partial X}+\frac{\partial \rho^* V}{\partial Y}=0 \tag{VI.14}$$

$$\rho^*\left(\frac{\partial U}{\partial \tau}+U\frac{\partial U}{\partial X}+V\frac{\partial U}{\partial Y}\right)=-\frac{\partial \Pi}{\partial X}+\Pr\left\{\frac{\partial}{\partial X}\left(\mu^*\frac{\partial U}{\partial X}\right)+\frac{\partial}{\partial Y}\left(\mu^*\frac{\partial U}{\partial Y}\right)+\frac{1}{3}\nabla\mu^*\nabla.\vec{V}\right\} \tag{VI.15}$$

$$\rho^*\left(\frac{\partial V}{\partial \tau}+U\frac{\partial V}{\partial X}+V\frac{\partial V}{\partial Y}\right)=-\frac{\partial \Pi}{\partial Y}-Ra\Pr\frac{\rho^*-1}{2\varepsilon_b}+\Pr\left\{\frac{\partial}{\partial X}\left(\mu^*\frac{\partial V}{\partial X}\right)+\frac{\partial}{\partial Y}\left(\mu^*\frac{\partial V}{\partial Y}\right)+\frac{1}{3}\nabla\mu^*\nabla.\vec{V}\right\} \tag{VI.16}$$

$$\rho c_p\left(\frac{\partial \theta}{\partial \tau}+U\frac{\partial \theta}{\partial X}+V\frac{\partial \theta}{\partial Y}\right)=\frac{\partial}{\partial X}\left(k^*\frac{\partial \theta}{\partial X}\right)+\frac{\partial}{\partial Y}\left(k^*\frac{\partial \theta}{\partial Y}\right)+\frac{\gamma-1}{2\varepsilon_b\gamma}\frac{d\overline{P}}{d\tau} \tag{VI.17}$$

$$\rho=\frac{\overline{P}}{(2\varepsilon_b T+1)} \tag{VI.18}$$

Porous region

$$\frac{\partial \rho}{\partial t}+\frac{\partial \rho U}{\partial X}+\frac{\partial \rho V}{\partial Y}=0 \tag{VI.19}$$

$$\rho\left(\frac{1}{\varepsilon}\frac{\partial U}{\partial \tau}+\frac{1}{\varepsilon^2}U\frac{\partial U}{\partial X}+\frac{1}{\varepsilon^2}V\frac{\partial U}{\partial Y}\right)=-\frac{1}{\varepsilon^2}\frac{\partial \Pi}{\partial X}+\frac{1}{\varepsilon}\Pr\left\{\frac{\partial}{\partial X}\left(\mu\frac{\partial U}{\partial X}\right)+\frac{\partial}{\partial Y}\left(\mu\frac{\partial U}{\partial Y}\right)+\frac{1}{3}\nabla\mu\nabla.\vec{V}\right\} - \frac{\Pr}{Da}U-\frac{1.75}{\sqrt{150Da}}\frac{\left|\vec{V}\right|}{\varepsilon^{3/2}}U \tag{VI.20}$$

$$\rho\left(\frac{1}{\varepsilon}\frac{\partial V}{\partial \tau}+\frac{1}{\varepsilon^2}U\frac{\partial V}{\partial X}+\frac{1}{\varepsilon^2}V\frac{\partial V}{\partial Y}\right)=-\frac{1}{\varepsilon^2}\frac{\partial \Pi}{\partial Y}+\frac{1}{\varepsilon}\Pr\left\{\frac{\partial}{\partial X}\left(\mu\frac{\partial V}{\partial X}\right)+\frac{\partial}{\partial Y}\left(\mu\frac{\partial V}{\partial Y}\right)+\frac{1}{3}\nabla\mu\nabla.\vec{V}\right\}-Ra.\Pr\frac{(\rho-1)}{2\varepsilon_b} - \frac{\Pr}{Da}V-\frac{1.75}{\sqrt{150Da}}\frac{\left|\vec{V}\right|}{\varepsilon^{3/2}}V \tag{VI.21}$$

$$\sigma\frac{\partial \theta}{\partial \tau}+U\frac{\partial \theta}{\partial X}+V\frac{\partial \theta}{\partial Y}=\frac{\partial}{\partial X}\left(k\frac{\partial \theta}{\partial X}\right)+\frac{\partial}{\partial Y}\left(k\frac{\partial \theta}{\partial Y}\right)+\frac{\gamma-1}{2\varepsilon_b\gamma}\frac{d\overline{P}}{d\tau} \tag{VI.22}$$

$$\rho=\frac{\overline{P}}{(2\varepsilon_b T+1)} \tag{VI.23}$$

With $\boldsymbol{\sigma=\frac{\varepsilon(\rho c_p)_f+(1-\varepsilon)(\rho c_p)_s}{(\rho c_p)_f}}$

VI.4 RADIATIVE ANALYSIS

The surface radiation does not modify the equations governing fluid motion but only alters the thermal boundary conditions. The coupling of natural convection with surface radiation occurs solely through the thermal boundary conditions. Without surface radiation, the adiabatic condition implies that the temperature gradient normal to these walls is zero. In the presence of surface radiation, the adiabatic condition is translated by the balance between conductive and radiative fluxes:

$$-k\frac{\partial T}{\partial y}\Big|_{y=0,\ H}+q_r=0 \tag{VI.24}$$

$q_r$is the net radiative flux density, determined by the following systems of equations:

$$q_r=\frac{\varepsilon}{1-\varepsilon}(\sigma T^4-J) \tag{VI.25}$$

$$AJ=b \tag{VI.26}$$

J is the radiosity vector

A is a matrix whose elements are given by:

$$A_{ij}=\delta_{ij}-(1-\varepsilon)F_{ij} \tag{VI.27}$$

and

$$b_i=\varepsilon\sigma T_i^4 \tag{VI.28}$$

The system describing the surface radiation is non-dimensionalized using the following parameters:

- The radiation temperature is non-dimensionalized by T_0, thus:

$$\Theta = \frac{T}{T_0} = \theta \frac{\Delta T}{T_0} + 1 = \frac{\theta}{\theta_0} + 1 \quad \text{(VI.29)}$$

Where: $\theta_0 = \frac{T_0}{\Delta T}$

- The radiation flux q_r is non-dimensionalized by σT_0^4 , thus:

$$Q_r = q_r / \sigma T_0^4 \quad \text{(VI.30)}$$

If the enclosure consists of *N* walls, the dimensionless radiosity of wall *i* is obtained by solving the following system:

$$\sum_{j=1}^{N} (\delta_{ij} - (1 - \varepsilon_i) F_{i-j}) R_j = \varepsilon_i \Theta_i^4 \quad \text{(VI.31)}$$

Where *R* is the dimensionless radiosity defined as:

$$R = J / \sigma T_0^4 \quad \text{(VI.32)}$$

Consequently, the dimensionless radiative flux density along a surface A_i is expressed as:

$$Q_{r,i} = R_i - \sum_{j=1}^{N} R_j F_{i-j} \quad \text{(VI.33)}$$

VI.4.1 Boundary conditions

Since the coupling of natural convection with surface radiation occurs solely through the thermal boundary conditions, the corresponding dimensionless boundary conditions are given by:

$U = V = 0,\ \theta = \theta_0$ for $\tau = 0$ (VI.34)

$U = V = 0,\ \theta = \theta_C = -0.5$ for $0 \le Y \le 1$ and $X = 0$ (VI.35)

$U = V = 0,\ \theta = \theta_H = 0.5$ for $0 \le Y \le 1$ and $X = 1$ (VI.36)

$U = V = 0,\ \frac{\partial \theta}{\partial Y} - Nr Q_r = 0$ for $0 \le X \le 1$ and $Y = 0$ (VI.37)

$U = V = 0, \frac{\partial \theta}{\partial Y} - Nr Q_r = 0$ for $0 \le X \le 1$ and $Y = 1$ (VI.38)

Where $Nr = \sigma T_0^4 H / k \Delta T$ is the dimensionless parameter of conduction-radiation.

VI.4.2 Heat transfer parameters

The following formulas provide the heat transfer rate on the active vertical walls in terms of average convective and radiative Nusselt numbers $Nu_{cavg}$and Nu_{ravg}:

$$Nu_{c_{avg}} = \int_0^1 -\frac{\partial\theta}{\partial X}\Big|_{X=0,1} dY \tag{VI.39}$$

$$Nu_{r_{avg}} = N_r \int_0^1 Q_r|_{X=0,1}\, dY \tag{VI.40}$$

The total average Nusselt number is obtained by summing the average values of the convective and radiative Nusselt numbers:

$$Nu_{avg} = \int_0^1 \left(-\frac{\partial\theta}{\partial X}\Big|_{0,1} + N_r Q_r|_{X=0,1}\right) dY \tag{VI.41}$$

VI.4.3 Numerical modelling

The 2-D governing differential equations for the velocity, pressure, and temperature fields are numerically solved using a finite volume approach. A power scheme is employed to approximate the advection-diffusion terms. To solve the pressure-velocity coupling, the SIMPLER (Semi-Implicit Method for Pressure Linked Equations Revised)method with a staggered grid is used, as described in Patankar[20]. The governing equations are formulated in transient form, and a fully implicit transient differencing scheme is used as an iterative procedure to reach steady state. The algebraic equations are solved using a combination of the line-by-line technique, which employs both the direct method (Thomas algorithm) and the iterative method (Gauss-Seidel). The discretized equations are solved using this technique with two directional sweeps. For each elemental wall surface, the radiosity is calculated as a function of temperature, emissivity, and view factor, through the following matrix equation:

$$[A_{i,j}][R_i] = [\sigma\theta_i^4] \tag{VI.42}$$

The analytical formulas for the view factors in 2D are provided as follows [21] (Figure VI.1):

$$F_{i-j} = \frac{-1}{2(x_2-x_1)}\left[\sqrt{x_2^2+y^2}\Big|_{y_1}^{y_2} - \sqrt{x_2^2+y^2}\Big|_{y_1}^{y_2}\right] \tag{VI.43}$$

$$F_{i-k} = -\frac{1}{2(x_2-x_1)}\left[\sqrt{(x_2-x)^2+H^2}\Big|_{x=x_1}^{x=x_2} - \sqrt{(x_1-x)^2+H^2}\Big|_{x=x_1}^{x=x_2}\right] \tag{VI.44}$$

VI.5 GRID SENSITIVITY

In order to achieve an optimal balance between the required precision and computation time, a mesh sensitivity test is conducted at various locations within a domain. A grid size variation ranging from (50×50) to (160×160) is used, with particular attention given to comparing the average Nusselt numbers on the vertical active walls.

The analysis is characterized by the following specific calculation parameters: $Ra=10^6$, $Yp=0.2$, $\varepsilon_r=0.5$, $Da=10^{-3}$, and $\Delta T=360$ K. The initial state corresponds to a quiescent medium, with a uniform temperature $T_0=300$K, for which the Prandtl number is $Pr=0.71$.

The results obtained for different mesh configurations are presented in Table VI.1. It should be noted that with a finer mesh, there is a reduction in the average Nusselt values. The observed reductions indicate that the solution becomes independent of the mesh beyond (100×100). This particular mesh size is identified as the optimal balance between accuracy and computation time, serving as the basis for code validation

Table VI.1: Mesh sensitivity test for convective, radiative and total Nusselt numbers.

Grid / Nu_{avg}		50*50	60*60	80*80	100*100	120*120	160*160
Convective	**Hot wall**	8.201255	8.191255	8.180472	8.157594	8.15723	8.14867
Radiative		6.299823	6.28924	6.281225	6.27943	6.275761	6.273356
Total		14.49003	14.48055	14.4617	14.43703	14.43299	14.42803
Convective	**Cold wall**	8.11632	8.07136	8.055877	8.032181	8.026004	8.02463
Radiative		6.41034	6.402246	6.4055	6.404661	6.406952	6.407051
Total		14.49352	14.47361	14.46138	14.4368	14.43295	14.42935

VI.6 VERIFICATION

Before presenting and discussing the results, the developed numerical code is validated to ensure that it produces accurate results. The results of the natural convection problem in the presence of surface radiation are compared to two sets of published data.

The average radiative Nusselt number and isotherms for (42 ×42) grid size are compared with those given in Wang et al. [22] and Akiyama et al. [23] as shown in Figures VI.2 and VI.3. Results of the present work compare exceedingly well with those given in the literature.

It should be mentioned here that in the works of Wang et al. [22] and Akiyama et al. [23], the Boussinesq approximation was taken into account for the temperature difference $\Delta T= 10$ K ($\varepsilon_b=0.017$), while this approximation is no longer valid for such a temperature difference. To simulate both pure natural convection ($\varepsilon_r = 0$) and combined natural convection with surface radiation ($\varepsilon_r > 0$), the use of the incompressible model based on the Boussinesq approximation can be considered valid under the condition $\varepsilon_b \leq 0.05$ when the temperature difference in the cavity is approximately less than 30K [16,24]

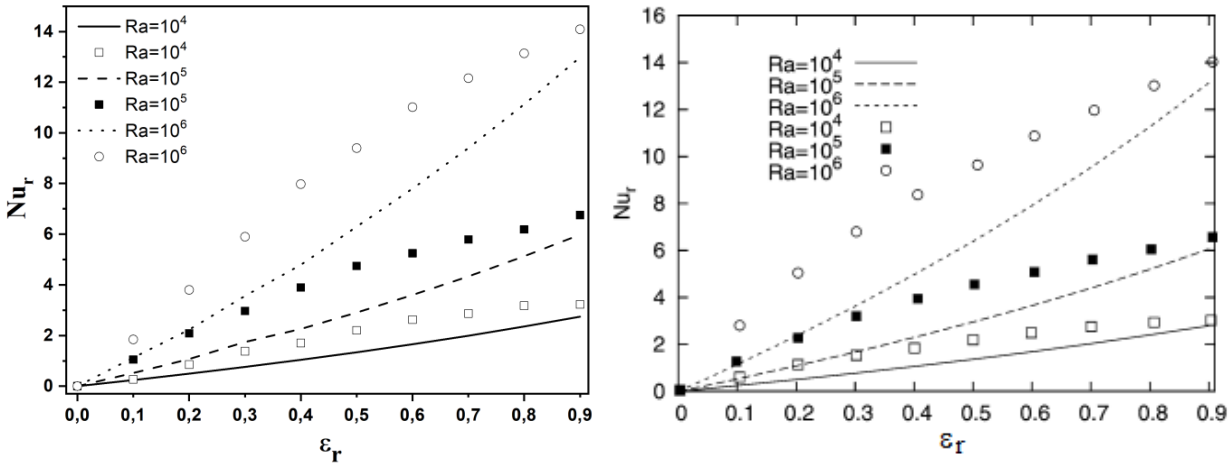

Present work Wang et al. [23]

Figure VI.2: Comparison of the average radiative Nusselt numbers of the present work with those of Wang et al. [23]

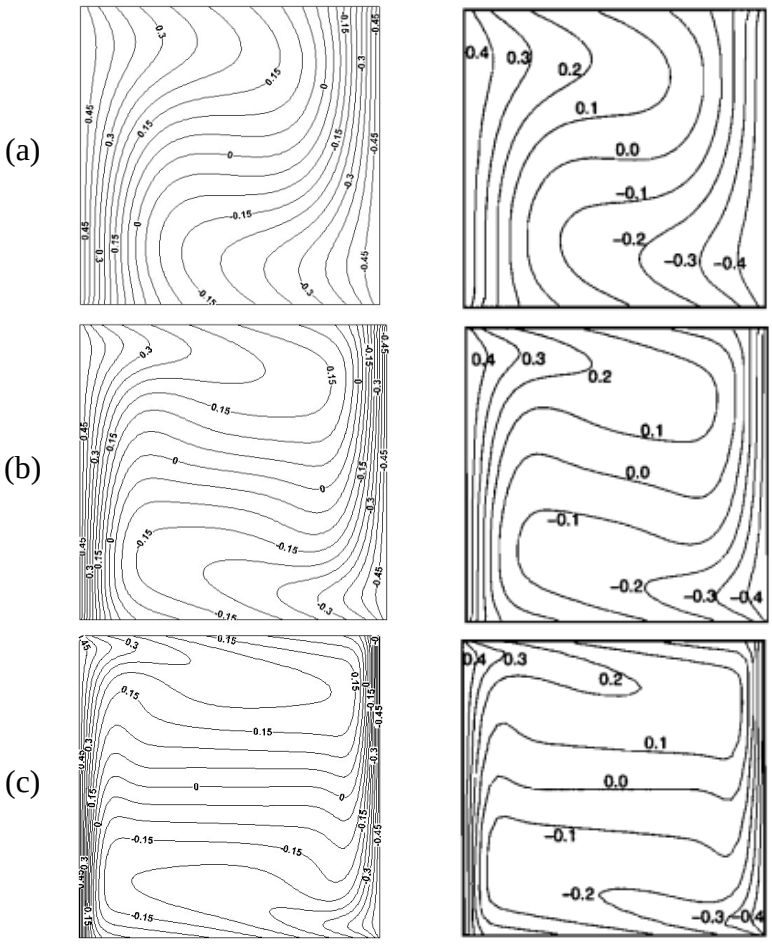

Present work Akiyama et al.[24]

Figure VI.3 : Comparison of the isotherms of the present work with those of Akiyama et al. **[24]**

VI.7 RESULTS AND DISCUSSION

In this section, we present and discuss the numerical results illustrating the impact of the examined parameters on flow characteristics and heat transfer. The study uses a compressible numerical model (LMN) to explore the influences of porous layer permeability and surface radiation on steady-state heat transfer and fluid flow in the presence of substantial temperature variations.

The system under investigation is an air enclosure incorporating porous media. It comprises a differentially heated cavity with isothermal vertical walls and adiabatic top and bottom walls

In the simulation, certain parameters are kept constant. These parameters include the Prandtl number (Pr = 0.71), the Rayleigh number (Ra = 10^6), the Boussinesq parameter (ε_b = 0.6), the porous layer thickness (Yp = 0.2) and the porosity (ε=0.4). However, we experiment with varying the Darcy number Da (10^{-5}, 10^{-3}) and emissivity ε_r (ranging from 0 to 1) in order to investigate the effects of permeability and surface radiation.

Figures VI.4 and VI.5 show temperature profiles for different emissivity (ε_r) values and two Darcy numbers: a low value (Da = 10^{-5}) and a high value (Da = 10^{-3}).

In Figure VI.4, the horizontal temperature profiles of the air in the middle of the cavity are presented for the specific case of ε_b = 0.6. The results demonstrate that the thickness of the thermal boundary layer varies with emissivity. Specifically, an increase in emissivity leads to thickening of the thermal boundary layer near the hot wall, while it thins near the cold wall. This variation in the thickness of the thermal boundary layer causes a shift in the temperature peaks towards the cold wall.

This effect is solely due to non-Boussinesq effects. In the central region, an increase in ε slightly raises the fluid's temperature, and higher permeability reduces the temperature stratification, with no significant influence from the porous layer. Figure VI.5 displays vertical temperature profiles in the middle of the cavity. Increasing ε results in heating at the bottom wall and cooling at the top wall. The presence of the porous layer and the Darcy number have noticeable effects. As emissivity increases, the temperature at the bottom wall rises in the presence of different permeabilities in the porous layer, while a decrease is observed near the top wall.

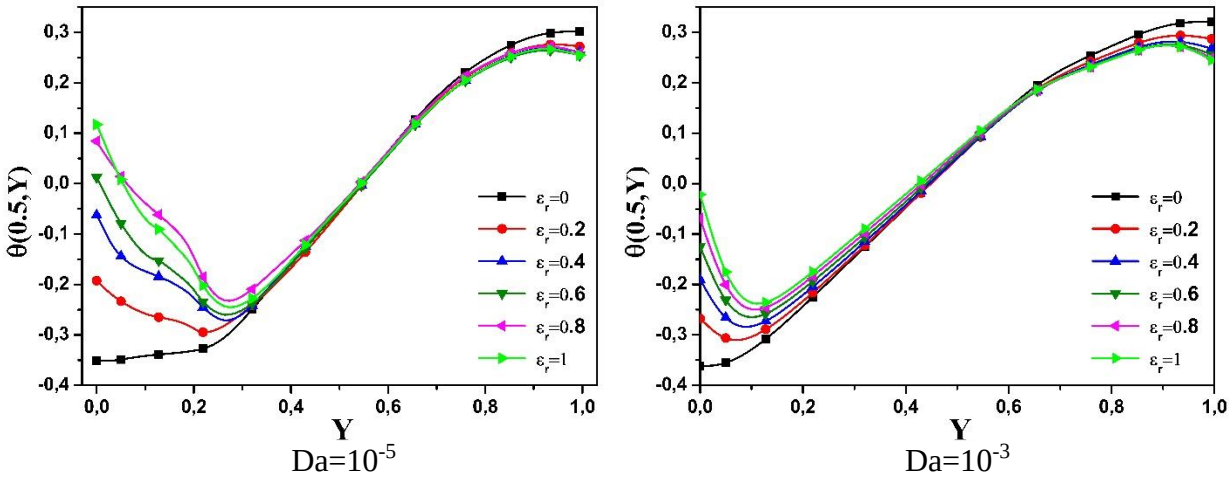

Figure VI.4: Horizontal temperature profiles as a function of emissivity (ε_r) for low ($Da = 10^{-5}$) and high ($Da = 10^{-3}$) Darcy numbers with $Ra = 10^6$, $\varepsilon_b = 0.6$

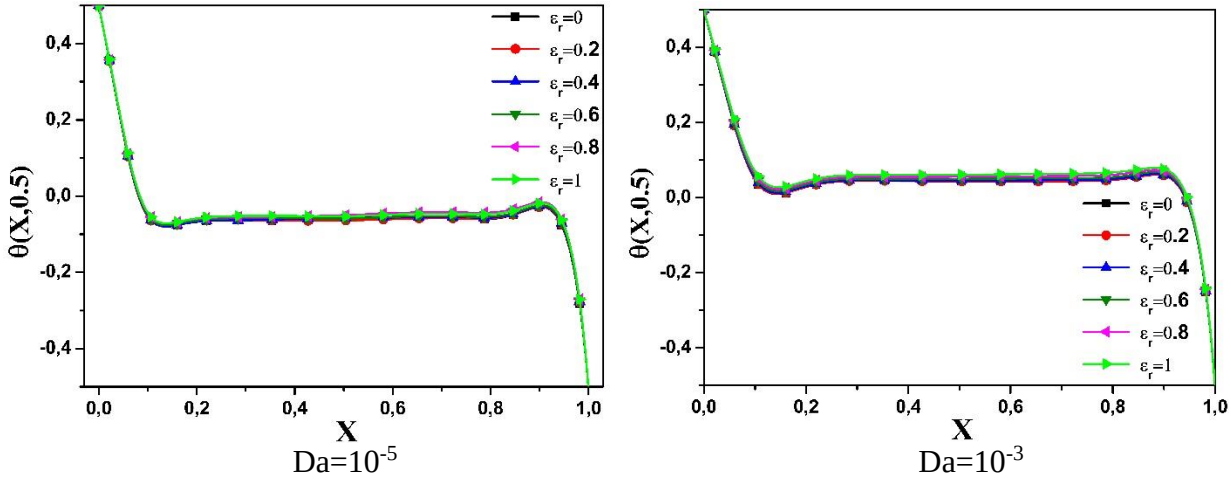

Figure VI.5: Vertical temperature profiles as a function of emissivity (ε_r) for low ($Da = 10^{-5}$) and high ($Da = 10^{-3}$) Darcy numbers with $Ra = 10^6$, $\varepsilon_b = 0.6$

The impact of emissivity (ε_r) and permeability (Da) on the flow is shown in Figures VI.6 and VI.7. Horizontal and vertical velocity components are plotted at X=0.5 and Y=0.5, respectively. The results reveal that within the porous layer, the flow is slightly faster with pure conduction heat transfer when ε is increased, especially at low Darcy numbers. Examining the U component profiles, we observe that the boundary layer contracts near the bottom wall and expands near the opposite wall. It is interesting to note that in the stratified region, the flow remains unchanged for the V component. Moreover, the peak value near the cold vertical wall is slightly lower for $Da=10^{-3}$ compared to $Da=10^{-5}$, indicating an increase in the permeability of the porous medium, resulting in reduced hydrodynamic resistance. Convection heat transfer within the porous layer becomes significant at high Darcy values, although the dominant mode is conduction.

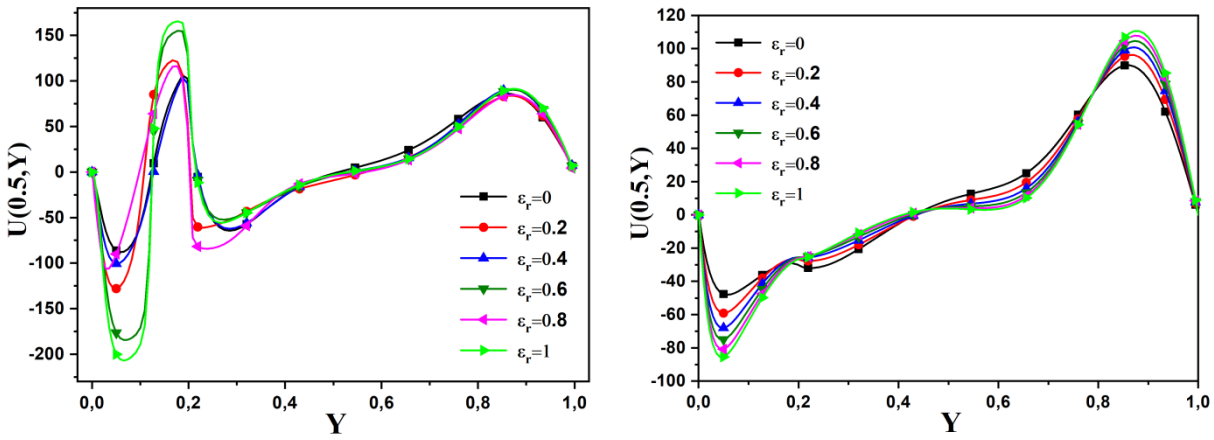

Da=10^{-5} Da=10^{-3}

Figure VI.6: Horizontal velocity profiles as a function of emissivity (ε_r) for low (Da =10^{-5}) and high (Da = 10^{-3}) Darcy numbers with Ra = 10^6, ε_b=0.6

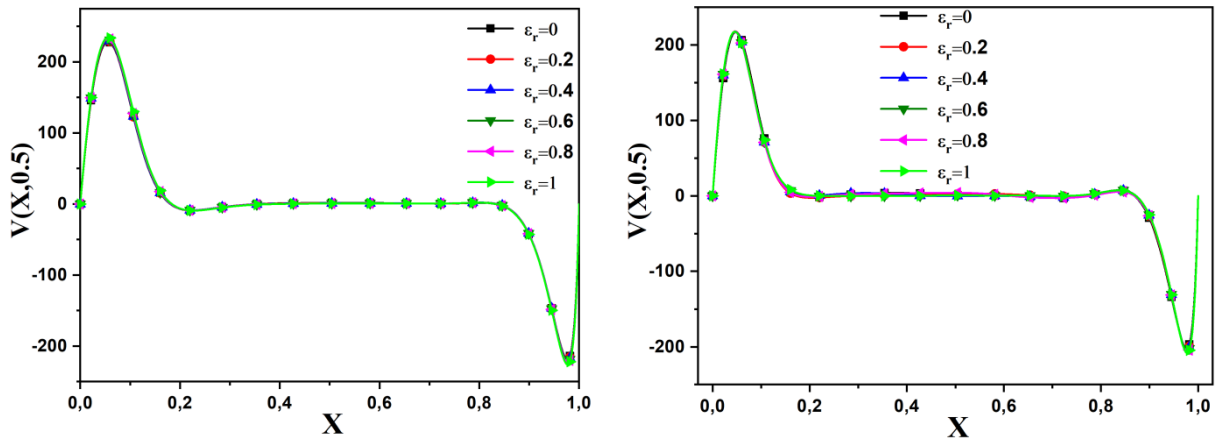

Da=10^{-5} Da=10^{-3}

Figure VI.7: Vertical velocity profiles as a function of emissivity (ε_r) for low (Da =10^{-5}) and high (Da = 10^{-3}) Darcy numbers with Ra = 10^6, ε_b=0.6.

Figures VI.8 and VI.9 demonstrate the impact of surface emissivity on the Nusselt number for high values of the Boussinesq parameter ε_b. The results reveal that the effect of surface emissivity on the Nusselt number differs between the free flow region (Yp> 0.2) and the porous medium region (Yp ≤ 0.2). In the porous medium region, the cold side wall experiences significantly lower values of the Nusselt number compared to the free flow region for Da=10^{-5}. On the hot side wall, an opposite effect is observed, where the impact is more pronounced compared to the free flow region. These changes are relatively smaller due to weaker natural convection and the absence of thermal radiation in the porous medium. Figures VI.8 and VI.9, also illustrates the effect of emissivity variation on the radiative Nusselt number. As expected, Nusselt values rapidly increases with emissivity on the cold side wall and decreases on the hot side wall. This indicates the significant role of surface radiation in heat transfer in the cavity, particularly at higher emissivity levels.The presence of thermal radiation on the surfaces results in a slight increase in the temperature gradient near the hot side wall in the free flow region, causing a slight elevation in the Nusselt number on

the hot side as emissivity increases. As a result, the Nusselt number at the hot wall is lower than that at the cold wall. Moreover, as emissivity further increases, the temperature gradient near the cold side also slightly rises in the free flow region.

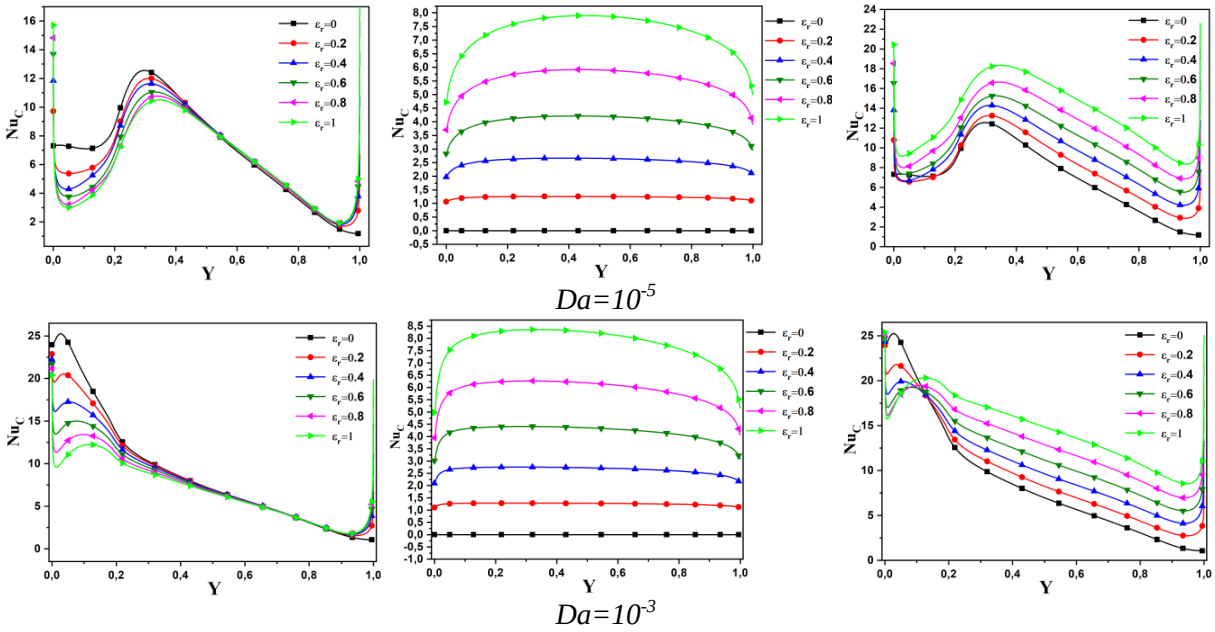

Figure VI.8: Evolution of the Nusselt numbersat the cold wall as a function of emissivity (ε_r) for low (Da = 10^{-5}) and high (Da = 10^{-3}) Darcy numbers with Ra = 10^6, ε_b=0.6

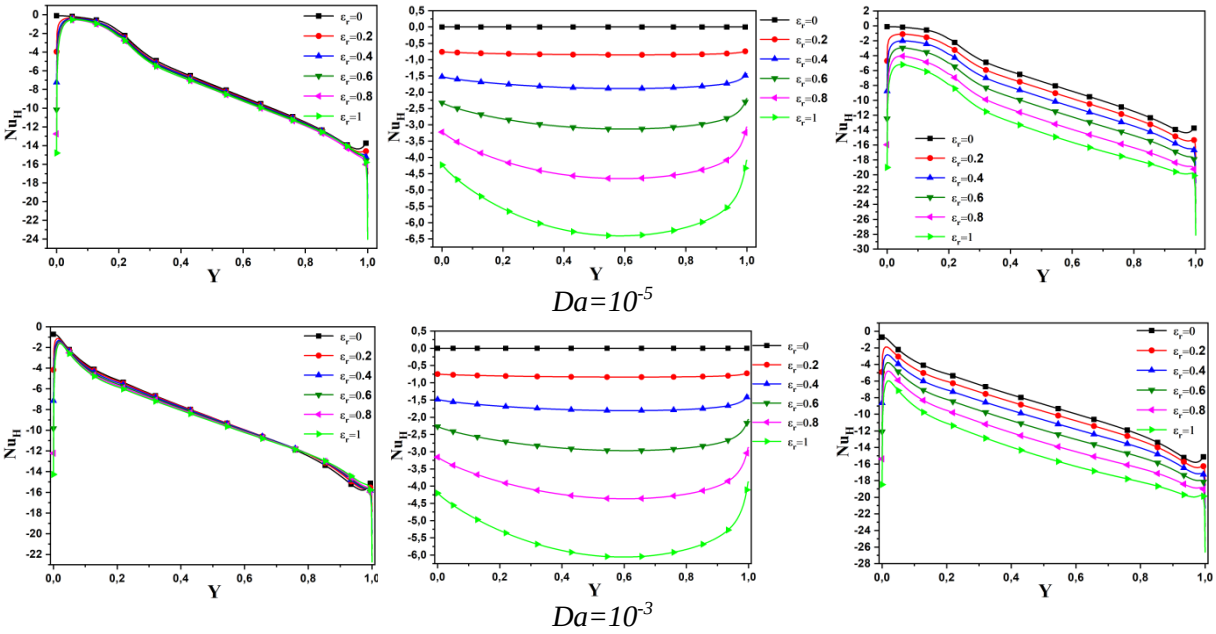

Figure VI.9: Evolution of the Nusselt numbersat the hot wall as a function of emissivity (ε_r) for low (Da = 10^{-5}) and high (Da = 10^{-3}) Darcy numbers with Ra = 10^6, ε_b=0.6

Figures VI.10 and VI.11 display streamlines and isotherm plots, which are used to compare simulations with and without surface radiation at different emissivities. The results consistently indicate that, since the temperature difference is high (ε_b = 0.6), the flow loses its symmetric nature.

As we can see in Figure VI.10, the secondary rolls within the primary flow become asymmetric. The permeability of the porous layer (Da) significantly influences the flow structure. An increase in Da reduces the strength of the cell due to the hydrodynamic resistance from the porous layer. At lower Da values, a contracted central cell can be observed, while higher Da values result in a horizontally elongated cell

A closer examination of Figure VI.11 reveals that the slopes of the isotherms near the lower wall differ from those near the upper wall. The predominantly vertical isotherm patterns within the porous layer indicate the dominance of conduction heat transfer, whereas the predominantly horizontal isotherm patterns imply convection dominance.

Furthermore, the introduction of radiation causes an increase in temperature at the interface and a decrease at the top wall in the free flow region. The presence of natural convection and thermal radiation at the interface between the free flow and porous medium leads to higher average temperatures in the porous medium compared to cases without radiation. Increasing the emissivity of the surfaces slightly amplifies the average temperature in the porous medium. The introduction of surface thermal radiation significantly shifts the mean temperature line to the right in the porous medium, even with low emissivity values. However, the extent of these changes is less pronounced when the emissivity increases from 0.5 to 1 compared to the range of 0 to 0.5.

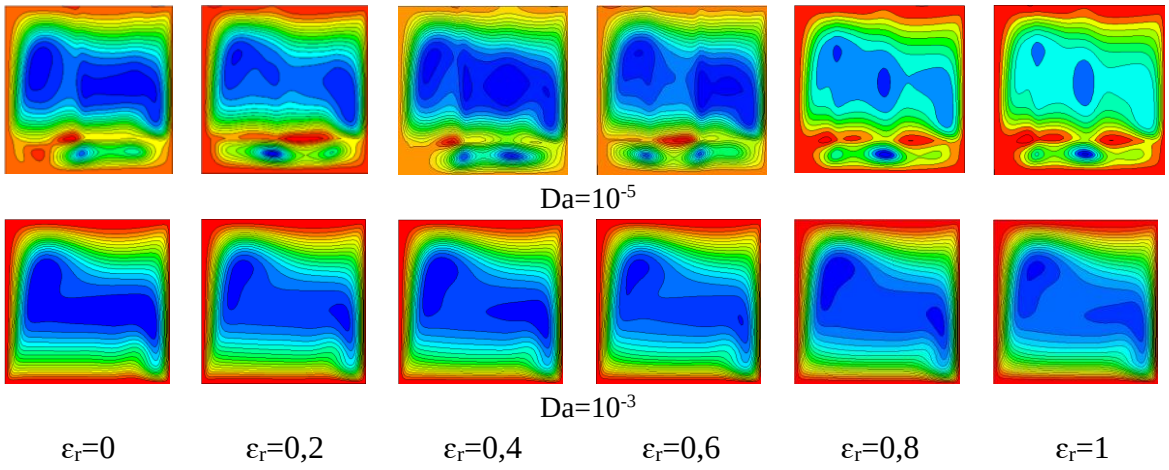

Figure VI.10: Streamlines as a function of emissivity (ε_r) for low (Da =10^{-5}) and high (Da = 10^{-3}) Darcy numbers with Ra = 10^6, ε_b=0.6.

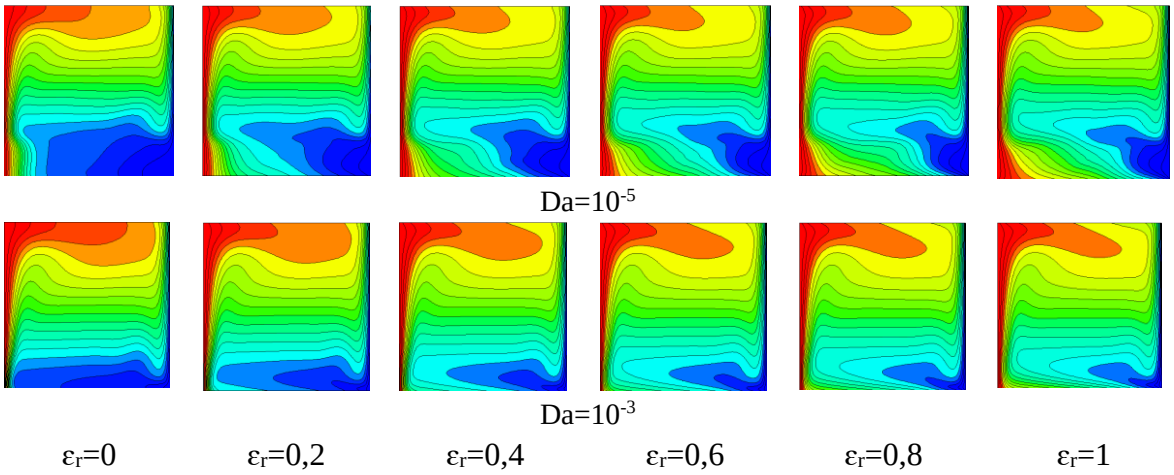

Figure VI.11: Isothermsas a function of emissivity (ε_r) for low (Da =10^{-5}) and high (Da = 10^{-3}) Darcy numbers with Ra = 10^6, ε_b=0.6.

To gain a better understanding of the effects of the studied parameters, we extensively investigate the overall heat transfer, represented by the average Nusselt numbers over the heated wall, as depicted in Figure VI.12.

The results demonstrate that overall heat transfer improves as the emissivity (ε_r) increases, regardless of the values of other parameters, even in the presence of the porous layer, which inherently resists heat transfer. This observation is clearly evident in Figure VI.12, indicating that the permeability of the porous layer does not significantly impact the enhancing effect of emissivity. However, our study reveals that in certain situations, particularly at lower Da values, increasing ε_r to 0.8 leads to an increase in the average convective Nusselt number. Subsequently, further increases in ε_r result in a steep stabilization of convective Nu_{avg} values, as shown in Figure VI.12a.

Additionally, in Figure VI.8b, the influence of effective thermal conductivity and hydrodynamic resistance is expressed at high Da numbers, due to the flow penetrating through the porous layer. In other words, the increase in Nu_{avg} with respect to ε_r can be attributed to the fact that, for different Da numbers, the flow penetrating into the porous layer is not affected by the acceleration caused by the thermal energy resulting from higher effective thermal radiation.

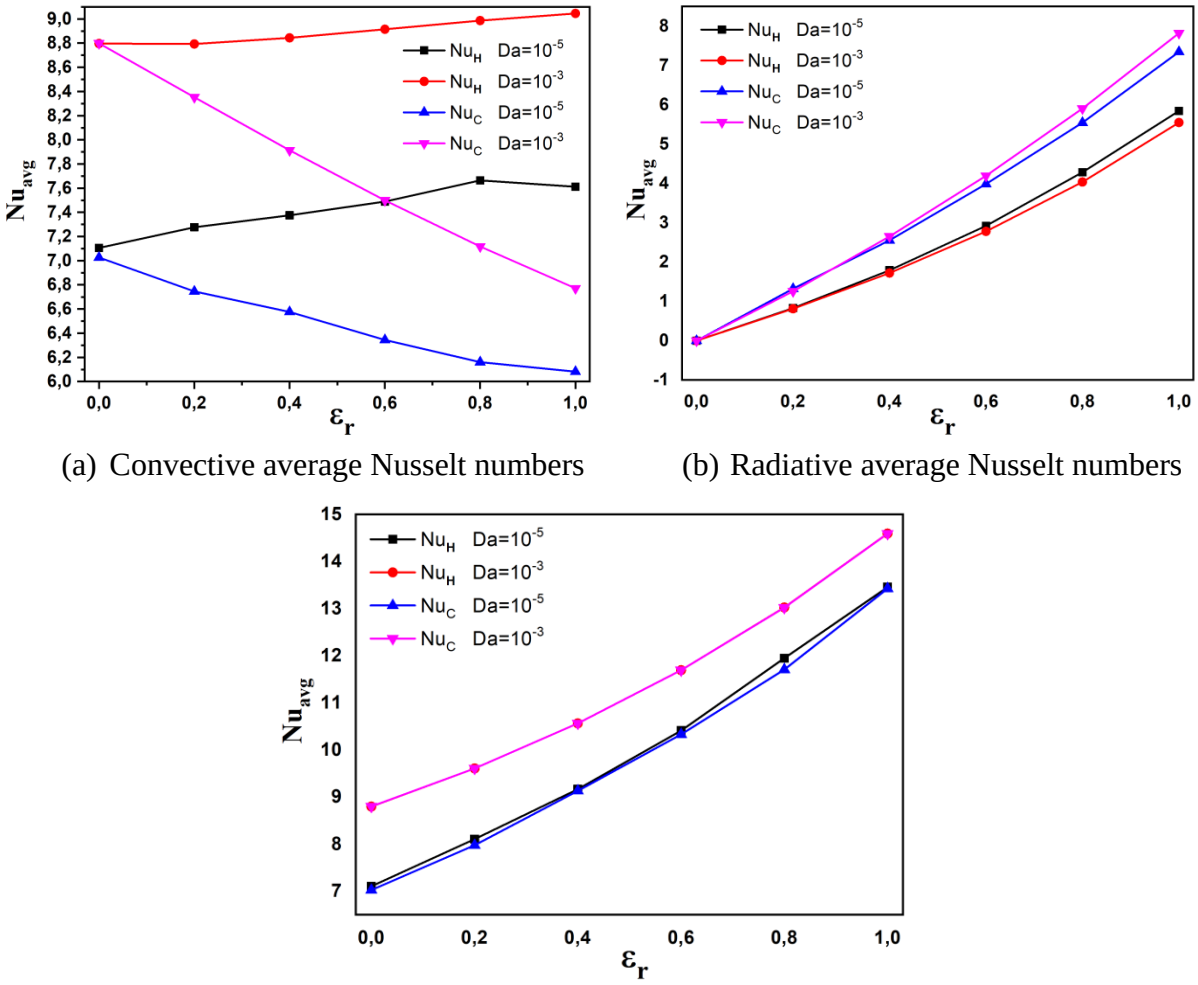

(a) Convective average Nusselt numbers (b) Radiative average Nusselt numbers

(c) Total average Nusselt numbers

Figure VI.12: Distribution of the average nusselt numbers as a function of emissivity (ε_r) for low (Da =10^{-5}) and high (Da = 10^{-3}) Darcy numbers with Ra = 10^6, ε_b=0.6.

VI.8 CONCLUSION

The investigation into heat transfer and fluid flow within a cavity, considering the influence of permeability in porous media and surface emissivity, has provided valuable insights into the complex interplay of these factors.

Permeability impact:

- Variations in permeability significantly alter flow behavior.

- Low permeability restricts fluid flow, reducing convection and heat transfer rates.

- High permeability facilitates fluid flow, enhancing heat transfer within the cavity.

Combined Radiation-Natural Convection:

- Numerical exploration of combined radiation-natural convection in a differentially heated cavity with porous medium revealed insightful patterns.

- Thermal radiation plays a crucial role in shaping natural convection and heat transfer in both free fluid and porous medium regions.

- Surface thermal radiation induces temperature distribution changes, even with a small emissivity. However, increasing emissivity from 0.5 to 1.0 does not lead to remarkable alterations.

- Compared to non-radiation scenarios, temperature rises at the interface and decreases at the top insulated wall. This leads to higher temperatures within the porous medium, with a slight increase as the emissivity of the surfaces rises.

In conclusion, this study underscores the significance of permeability and emissivity in shaping heat transfer and fluid flow dynamics. The observed variations in parameters provide a nuanced understanding of the intricate relationship between these factors, offering valuable implications for practical applications and further research in thermal systems.

References

[1] S.R. Sondur, A.M. Mescher, Natural convection of Boussinesq and non-Boussinesq airflows simulated in a tall annular cavity, Numer. Heat Transf. Part Appl. 0 (2022) 1–27. https://doi.org/10.1080/10407782.2022.2105121.

[2] E.G. Barbosa, M.E.V. Araujo, M.A. Martins, Natural Convection and Radiation in Enclosures with Semi-transparent Medium: Conjugate CFD Analysis, J. Appl. Fluid … (2022). https://www.jafmonline.net/article_2068.html.

[3] T.M. Shih, A Literature Survey on Numerical Heat Transfer, Numer. Heat Transf. 5 (1982) 369–420. https://doi.org/10.1080/10407788208913456.

[4] M.S. Astanina, M.A. Sheremet, J.C. Umavathi, Effect of thermal radiation on natural convection in a square porous cavity filled with a fluid of temperature-dependent viscosity, Therm. Sci. 22 (2018) 391–399. http://www.doiserbia.nb.rs/Article.aspx?ID=0354-98361600164A.

[5] S.G. Bejawada, M.M. Nandeppanavar, Effect of thermal radiation on magnetohydrodynamics heat transfer micropolar fluid flow over a vertical moving porous plate, Exp. Comput. (2023). https://doi.org/10.1007/s42757-021-0131-5.

[6] M.S. Astanina, M. Sheremet, J.C. Umavathi, Effect of thermal radiation on natural convection in a square porous cavity filled with a fluid of temperature-dependent viscosity, (2016). https://doi.org/10.2298/TSCI150722164A.

[7] Y. Wang, J. Yang, X. Zhang, Y. Pan, Effect of Surface Thermal Radiation on Natural Convection and Heat Transfer in a Cavity Containing a Horizontal Porous Layer, Procedia Eng. 121 (2015) 1193–1199. https://doi.org/10.1016/J.PROENG.2015.09.137.

[8] S. Paolucci, On the Filtering of Sound from the Navier–Stokes Equations, NASA STIRecon Tech. Rep. N 83 (1982) 26036.

[9] D.D. Gray, A. Giorgini, The validity of the boussinesq approximation for liquids and gases, Int. J. Heat Mass Transf. 19 (1976) 545–551. https://doi.org/10.1016/0017-9310(76)90168-X.

[10] G. De Vahl Davis, Natural convection of air in a square cavity: A bench mark numerical solution, Int. J. Numer. Methods Fluids 3 (1983) 249–264. https://doi.org/10.1002/fld.1650030305.

[11] S. Chen, W. Gong, Y. Yan, Conjugate natural convection heat transfer in an open-ended square cavity partially filled with porous media, Int. J. Heat Mass Transf. 124 (2018) 368–380. https://doi.org/10.1016/j.ijheatmasstransfer.2018.03.084.

[12] M. Aneja, A. Chandra, S. Sharma, Natural convection in a partially heated porous cavity to Casson fluid, Int. Commun. Heat (2020). https://www.sciencedirect.com/science/article/pii/S0735193320300804.

[13] S. Hamimid, M. Guellal, Numerical Study of Combined Natural Convection-surface Radiation in a Square Cavity, (n.d.).

[14] M. Bouafia, S. Hamimid, M. Guellal, Non-Boussinesq convection in a square cavity with surface thermal radiation, Int. J. Therm. Sci. 96 (2015) 236–247. https://doi.org/10.1016/j.ijthermalsci.2015.04.017.

[15] S. Hamimid, M. Guellal, Thermomagnetic convection-surface radiation interactions in microgravity environment, Fluid Dyn. Mater. Process. 12 (2016) 137–153. https://doi.org/10.3970/fdmp.2016.012.137.

[16] S. Hamimid, M. Guellal, M. Bouafia, Numerical study of natural convection in a square cavity under non-boussinesq conditions, Therm. Sci. 20 (2016).

[17] S. Hamimid, M. Guellal, Numerical analysis of combined natural convection-internal heat generation source-surface radiation, Therm. Sci. 20 (2016) 1879–1889. http://www.doiserbia.nb.rs/Article.aspx?id=0354-98361400115H (accessed September 22, 2022).

[18] F.M. White, Viscous fluid flow, 2nd ed, McGraw-Hill, New York, 1991.

[19] S. Hamimid, N. Rachedi, M. Guellal, M. Bouafia, Compressible Coupled Natural Convection and Volumetric Radiation in a Square Cavity, J. Thermophys. Heat Transf. 32 (2018) 580–589. https://doi.org/10.2514/1.T5333.

[20] S. Patankar, Numerical Heat Transfer and Fluid Flow, CRC Press, Boca Raton, 2018. https://doi.org/10.1201/9781482234213.

[21] J.R. Howell, A Catalog of Radiation Configuration Factors, McGraw-Hill, 1982.

[22] H. Wang, S. Xin, P. Le Quéré, Étude numérique du couplage de la convection naturelle avec le rayonnement de surfaces en cavité carrée remplie d'air, Comptes Rendus Mécanique 334 (2006) 48–57. https://doi.org/10.1016/j.crme.2005.10.011.

[23] M. Akiyama, Q.P. Chong, numerical analysis of natural convection with surface radiation in a square enclosure, Numer. Heat Transf. Part Appl. (1997). https://doi.org/10.1080/10407789708913899.

[24] S. Hamimid, Simulation numérique de la convection naturelle couplée au rayonnement ou à un champ magnétique dans l'approximation faible nombre de Mach, Thesis, 2018. http://dspace.univ-setif.dz:8888/jspui/handle/123456789/1159.

GENERAL CONCLUSIONS

This research has investigated the intricate dynamics of fluid flow and heat transfer within a square cavity, considering the influence of permeability in porous media, surface emissivity, and the coupling effects of natural convection with internal heat generation. The study aimed to clarify the complex interactions among these factors and their implications for engineering applications involving thermal systems and energy transfer.

The primary focus of this study was to examine how the presence of a porous medium influences fluid flow and heat transfer characteristics within the square cavity. Through a combination of mathematical analysis and numerical simulations using advanced computational methods, valuable insights were gained into the behavior of fluid flow and heat transfer under varying conditions.

Additionally, the investigation addressed the limitations of the Boussinesq approximation for predicting fluid heat transfer under significant temperature gradients. By adopting a compressible model based on the low Mach number approximation, more accurate results were obtained, emphasizing the importance of selecting appropriate modeling approaches in complex fluid dynamics scenarios.

Furthermore, the study explored the competition between internal and external Rayleigh numbers (Ra_I and Ra_E), revealing their critical role in shaping overall system behavior. The analysis provided insights into the balance between buoyancy forces induced by internal heat generation and external temperature gradients imposed on the cavity, elucidating the interplay between porous medium characteristics, natural convection, and internal heat generation.

This research underscores the importance of understanding variations in thermophysical property on fluid flow and heat transfer within cavities, which is crucial for optimizing thermal systems and designing efficient heat exchangers.

One of the key findings is the significant role of permeability in porous media on altering flow behavior. It was observed that low permeability restricts fluid flow, resulting in reduced convection and heat transfer rates within the cavity. Conversely, higher permeability facilitates fluid flow, thereby enhancing heat transfer effectiveness. This understanding is crucial for optimizing thermal management strategies and designing efficient heat exchangers in engineering applications.

Moreover, the study highlighted the crucial influence of thermal radiation on shaping flow patterns and heat transfer dynamics. Surface emissivity plays a critical role in determining temperature distributions within the cavity, with increasing emissivity leading to moderate alterations in temperature profiles. The incorporation of radiation reduces stratification within the cavity and promotes flow along the horizontal walls and within the porous medium, ultimately affecting heat transfer rates.

These findings have profound implications for optimizing thermal systems and designing energy-efficient solutions across various engineering disciplines. Understanding the nuanced interactions between permeability, radiation, and fluid dynamics enables the development of tailored solutions to enhance heat transfer performance and energy utilization.

Moving forward, several future research directions are highly recommended to expand on the current findings. For instance, exploring the influence of a magnetic field in the presence of porous media could offer novel perspectives on how magnetic effects impact fluid dynamics and heat transfer in such systems. Additionally, investigating volumetric radiation effects within a porous medium could provide deeper insights into the role of radiation in modifying heat transfer characteristics within porous enclosures. These avenues of research have the potential to uncover new phenomena and enhance our understanding of complex thermal systems involving porous media and radiative heat transfer.

ABSTRACT

This thesis explores natural convection heat transfer in fluid-saturated porous media within enclosed cavities, a key area with applications in thermal management and industrial processes. The research examines the effects of internal heat generation, thermal radiation, temperature differences and porous medium characteristics on fluid flow and heat transfer rates. All simulations are conducted under the low Mach number approximation, where high temperature gradients ensure accurate fluid dynamics modeling. Numerical simulations, based on the Darcy-Brinkman model and Navier-Stokes equations, analyze laminar flow patterns and temperature fields. Key parameters such as internal Rayleigh number, external Rayleigh number, Darcy number, porosity, emissivity, and Boussinesq parameter are investigated. Results show that higher Darcy numbers improve fluid flow and heat transfer, while increased porosity enhances heat exchange surface area. Thermal radiation plays a significant role in shaping convection patterns and overall heat transfer rates. This study provides valuable insights for optimizing heat exchange in energy-efficient systems and industrial applications.

Keywords: *Natural convection, Porous layer, Internal heat source, Finite volume method, SIMPLER algorithm, Permeability, Porosity, Layer thickness, Low Mach Number approximation, Boussinesq approximation, surface radiation.*

RÉSUMÉ

Cette thèse explore le transfert de chaleur par convection naturelle dans des milieux poreux saturés de fluide au sein de cavités fermées, un domaine clé avec des applications dans la gestion thermique et les processus industriels. La recherche examine les effets de la génération de chaleur interne, du rayonnement thermique, des différences de température et des caractéristiques du milieu poreux sur l'écoulement des fluides et les taux de transfert de chaleur. Toutes les simulations sont réalisées sous l'approximation des faibles nombres de Mach, où des gradients de température élevés assurent une modélisation précise de la dynamique des fluides. Des simulations numériques, basées sur le modèle de Darcy-Brinkman et les équations de Navier-Stokes, analysent les schémas d'écoulement laminaire et les champs de température. Des paramètres clés tels que le nombre de Rayleigh interne, le nombre de Rayleigh externe, le nombre de Darcy, la porosité, l'émissivité et le paramètre de Boussinesq sont étudiés. Les résultats montrent que des nombres de Darcy plus élevés améliorent l'écoulement des fluides et le transfert de chaleur, tandis qu'une porosité accrue augmente la surface d'échange de chaleur. Le rayonnement thermique joue un rôle significatif dans la formation des schémas de convection et les taux globaux de transfert de chaleur. Cette étude fournit des informations précieuses pour optimiser les échanges de chaleur dans des systèmes économes en énergie et des applications industrielles.

Mots-clés : Convection naturelle, Couche poreuse, Source de chaleur interne, Méthode du volume fini, Algorithme SIMPLER, Perméabilité, Porosité, Épaisseur de couche poreuse, Approximation de nombre de Mach faible, Approximation de Boussinesq, Rayonnement de surface.

الملخص

تتناول هذه الأطروحة انتقال الحرارة بالتدفق الحراري الطبيعي في الوسائط المسامية المشبعة بالسوائل داخل تجاويف مغلقة، وهو مجال أساسي له تطبيقات في إدارة الحرارة والعمليات الصناعية. تبحث الدراسة في تأثيرات توليد الحرارة الداخلي والإشعاع الحراري وفروقات درجات الحرارة وخصائص الوسط المسامي على سلوك تدفق السوائل ومعدلات انتقال الحرارة. تم إجراء جميع المحاكاة تحت تقريب الأعداد المنخفضة لماخ، حيث تضمن التدرجات العالية في درجات الحرارة نمذجة دقيقة لديناميكا الموائع. تستند المحاكاة العددية إلى نموذج دارسي-برينكمان ومعادلات نافييه-ستوكس لتحليل أنماط التدفق الطبقي وحقول درجات الحرارة. تم دراسة معايير رئيسية مثل عدد رايلي الداخلي، عدد رايلي الخارجي، عدد دارسي، المسامية، الانبعاثية، ومعامل بوسينسك. أظهرت النتائج أن الأعداد الأعلى لدارسي تحسن تدفق السوائل وانتقال الحرارة، بينما تعزز المسامية العالية مساحة التبادل الحراري. يلعب الإشعاع الحراري دورًا مهمًا في تشكيل أنماط التدفق الحراري ومعدلات انتقال الحرارة الإجمالية. توفر هذه الدراسة رؤى قيمة لتحسين آليات تبادل الحرارة في الأنظمة الموفرة للطاقة والتطبيقات الصناعية.

الكلمات المفتاحية: الحمل الطبيعي، الطبقة المسامية، مصدر حراري داخلي، طريقة volume fini ، خوارزمية SIMPLER ، النفاذية، المسامية، سمك الطبقة، تقريب *Low Mach Number*، تقريب Boussinesq ، الإشعاع السطحي.